Diese Arbeit wurde vorgelegt am
Lehrstuhl für Mathematik (MathCCES)

Optische und elektrische Simulation von Solarzellen
Optical and Electrical Simulation of Solar Cells

Masterarbeit Physik

25. Oktober 2017

Vorgelegt von Presented by	Paul Luckner paul.luckner@rwth-aachen.de
Erstprüfer First examiner	Prof. Dr. Martin Frank Lehrstuhl für Mathematik (MathCCES) RWTH Aachen University
Zweitprüfer Second examiner	Privatdozent Dr. habil. Dimitry Chigrin Lehrstuhl für Experimentalphysik I A RWTH Aachen University
Koreferent Co-supervisor	Dr. rer. nat. Pascal Richter Lehrstuhl für Mathematik (MathCCES) RWTH Aachen University

Eidesstattliche Versicherung

Statutory Declaration in Lieu of an Oath

Luckner, Paul

Name, Vorname/Last Name, First Name

313243

Matrikelnummer (freiwillige Angabe)
Matriculation No. (optional)

Ich versichere hiermit an Eides Statt, dass ich die vorliegende Arbeit/Bachelorarbeit/Masterarbeit* mit dem Titel

I hereby declare in lieu of an oath that I have completed the present paper/Bachelor thesis/Master thesis* entitled

Optical and Electrical Simulation of Solar Cells

selbstständig und ohne unzulässige fremde Hilfe erbracht habe. Ich habe keine anderen als die angegebenen Quellen und Hilfsmittel benutzt. Für den Fall, dass die Arbeit zusätzlich auf einem Datenträger eingereicht wird, erkläre ich, dass die schriftliche und die elektronische Form vollständig übereinstimmen. Die Arbeit hat in gleicher oder ähnlicher Form noch keiner Prüfungsbehörde vorgelegen.

independently and without illegitimate assistance from third parties. I have used no other than the specified sources and aids. In case that the thesis is additionally submitted in an electronic format, I declare that the written and electronic versions are fully identical. The thesis has not been submitted to any examination body in this, or similar, form.

Aachen,

Ort, Datum/City, Date

Unterschrift/Signature

*Nichtzutreffendes bitte streichen

*Please delete as appropriate

Belehrung:
Official Notification:

§ 156 StGB: Falsche Versicherung an Eides Statt

Wer vor einer zur Abnahme einer Versicherung an Eides Statt zuständigen Behörde eine solche Versicherung falsch abgibt oder unter Berufung auf eine solche Versicherung falsch aussagt, wird mit Freiheitsstrafe bis zu drei Jahren oder mit Geldstrafe bestraft.

Para. 156 StGB (German Criminal Code): False Statutory Declarations

Whoever before a public authority competent to administer statutory declarations falsely makes such a declaration or falsely testifies while referring to such a declaration shall be liable to imprisonment not exceeding three years or a fine.

§ 161 StGB: Fahrlässiger Falscheid; fahrlässige falsche Versicherung an Eides Statt

(1) Wenn eine der in den §§ 154 bis 156 bezeichneten Handlungen aus Fahrlässigkeit begangen worden ist, so tritt Freiheitsstrafe bis zu einem Jahr oder Geldstrafe ein.

(2) Straflosigkeit tritt ein, wenn der Täter die falsche Angabe rechtzeitig berichtigt. Die Vorschriften des § 158 Abs. 2 und 3 gelten entsprechend.

Para. 161 StGB (German Criminal Code): False Statutory Declarations Due to Negligence

(1) If a person commits one of the offences listed in sections 154 through 156 negligently the penalty shall be imprisonment not exceeding one year or a fine.

(2) The offender shall be exempt from liability if he or she corrects their false testimony in time. The provisions of section 158 (2) and (3) shall apply accordingly.

Die vorstehende Belehrung habe ich zur Kenntnis genommen:

I have read and understood the above official notification:

Aachen,

Ort, Datum/City, Date

Unterschrift/Signature

Abstract

The direct conversion of solar irradiation into electric power is only possible with solar cells. Their basic principle follows a common idea: Sun light is absorbed within an optically active material. Absorption leads to generations of free charge carriers which are separated by polarity, and transported towards different contacts. The potential difference on contacts can be used for electrical work and thus, electricity is generated. Current cells need further optimization to reach their theoretical limits which is financially feasible for most parts only using simulations.

The treatment of light absorption is done using different models. At first, we use an incoherent model based on the Lambert-Beer law. It is derived from first principle using the Boltzmann transport equation for photon distributions. An implementation is discussed which uses a multi-layer setup in one dimension on uniformly distributed grids for wavelength and position spaces. The optical simulation's goal is the calculation of a charge generation rate's profile along the cell's depth. The influence of the input parameters' discretization as well as the positional discretization upon the generation rate is investigated. An anti-reflection coating is used to reduce the reflection at the front interface. The incoherent Lambert-Beer implementation is tested against a coherent light model solving the full Maxwell's equations using a finite difference scheme – the so-called Yee algorithm. It is implemented for a two-dimensional multi-layered structure and the comparison is done by averaging out one dimension.

Charge transportation within semiconducting layers is treated by the semiconductor's drift-diffusion equations. They are being derived from first principle using the Boltzmann transport equation and assuming multiple approximations for the underlying electron distribution. Within this thesis an implementation is proposed which solves the one-dimensional drift-diffusion equations using the finite difference method. The optical absorption, and electrical charge transportation models couple as the absorption's generation rate is a source term within the charge transportation's drift-diffusion equations.

Contents

List of Figures

List of Tables

1. Introduction

Human population is in constant need for energy. Electrical energy is one of the most useful forms as we can use it for almost anything. Up to now the main energy sources are *fossil fuels*: coal, oil, natural gas, and nuclear. These sources are available only in limited amounts and their energy production relies heavily on combustion which produces Greenhouse gases that accelerate climate change. Nuclear power plants inhibit the threat of a nuclear radiation incident, or problems that come along with nuclear waste. This lead to the research and development of a new class of energy sources – the so-called *renewables*: wind, biomass, hydroelectric, and solar. As solar irradiation is the most abundant energy source on Earth it should yield a reliable source for our energy needs. The only direct conversion of solar radiation towards electrical energy is given by **photovoltaic cells**.

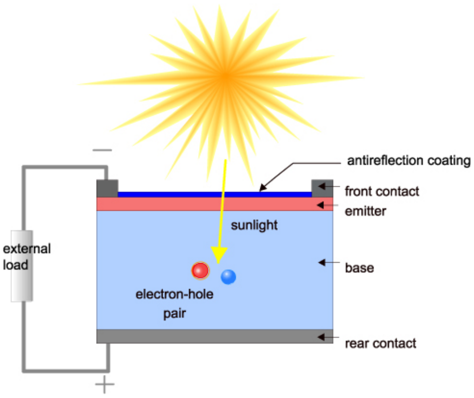

Figure 1.: A sketch of a solar cell showing its operating principle [43]. Sunlight is transmitted through the anti-reflection coating, and absorbed in the base which generates electron-hole pairs. Charge transportation towards the contacts results in usable voltage differences.

A photovoltaic cell generates electrical energy by harvesting solar radiation during a multi-step process. The sun emits light via a wavelength-dependent spectrum. It propagates through space without interaction but once it hits Earth's atmosphere parts of it are strongly absorbed or reflected whereas others are almost ideally transmitted onto sea level. The sunlight enters photovoltaic devices with additional losses which can be minimized by using anti-reflection coatings (ARC). As the sunlight's photons propagate through the cell's structure they have a non-vanishing probability for **absorption** by bounded electrons. In the absorption process the photon will interact with the bounded electron to form an (excited) electron-hole pair.

To produce electrical currents the different charges (electrons and holes) need to be separated and extracted along different paths. In fact, the extraction should happen because of an internal process such that the charges can still perform physical work. As gravitational force, and temperature gradients are usually neglected for solar cells the driving forces are purely by **electrical**, and chemical gradients. In conventional solar cells one uses semiconducting materials – such as silicon (Si), or gallium arsenide (GaAs) – to cause charge separation. By the process of doping one can force large differences of Fermi energies at the terminals which result into voltage differences that can be used to perform work.

For the research and development of photovoltaic devices one relies heavily upon numerical simulations. The cost for producing high tech prototypes for solar cells is often economically not feasible as well as time consuming. By using numerical simulations one can work on each part of the product by its own. The simulations will yield satisfying results as long as the numerical models are accurate enough. Especially for the optimization of material parameters one often falls back to simulations as one can do a whole batch run for a range of parameters.

Simulations for solar cells are usually split up into two processes. At first the optical absorption will be simulated and the resulting generation rate for electron-hole pairs can be computed. Then the electrical charges will be propagated by the transport simulation. Each step is quite involved and can be performed up to arbitrary precision from one to three dimensions. Often simulation in one or two spatial dimension is sufficient but some device geometries require simulation in three dimensions.

The optical simulation can be performed using many different models. On the one-hand side one can treat light incoherently and apply the Lambert-Beer law which yields the absorption profile in one dimension. Another possibility is to solve Maxwell's equations rigorously for propagation of light in space-time by using algorithms such as introduced by Kane Yee in 1966 [55]. The different algorithm and especially the increase in dimensions introduces numerical challenges as the systems of equations one has to solve tend to become large very quickly. Another problem arises when working with heterostructures which incorporate different materials in each layer. This introduces discontinuities in material parameters across the structure which result into regions where variables tend to change by different orders of magnitude.

The electrical simulation can be solved for different approximations, such as the drift-diffusion, or the hydrodynamical model. The models are compromised of a system of coupled partial differential equations where higher order approximations add additional variables, and equations to the system.

The inner working principles for solar cells have been studied. The process of transforming sun light into electrical energy is a two-step process which is not analytically solvable except for the simplest test cases where most parameters have been set constant. The goal of this work is to solve a solar cell in total and for this purpose we needed to rely on simulation software. We tested several tools but none could fulfill the requirements of open-source code, exhaustive documentation, and being feature-rich. Thus, we have implemented our own model from scratch using the MATLAB® programming environment.

The application is modular implemented such that it could easily be extended by other models and represent a large array of possible cells. The application is able to calculate conventional silicon solar cells but other materials such as gallium arsenide are also available.

In Chapter 2 we will start to tackle the absorption problem of solar cells. We will point out the current state of optical simulations as well as the general physical background which is needed for further discussions. Thereafter we introduce our implementation of the one-dimensional Lambert-Beer model. This will include the total numerical schemes we used. In the next section we run several case studies where we compare our model to existing software.

Chapter 3 will discuss the topic of charge transport in semiconductors. We start by noting the current state of the art. Then we will introduce the drift-diffusion model which governs charge transport. The model will be derived from the underlying Boltzmann transport equation in detail. After explaining the physical background we dive into our implementation of the drift-diffusion model. The model will be discussed in detail and the numerical schemes will be highlighted. Thereafter we present case studies made from our implementation.

With Chapter 4 we will finish by giving a summary of the presented work and an outlook for possible future work.

2. Absorption of Sun Light

2.1. State of the art

Optical simulation of solar cells can be achieved by the Lambert-Beer model. It is implemented within general purpose device modeling applications such as Synopsys' Sentaurus™ [44], Silvaco's Atlas™ [41], and COMSOL Multiphysics® [3]. Apart from these full-blown industry-standard tools there are programs especially written for solar cells. The Helmholtz-Zentrum Berlin has published a feature-rich Windows gui-tool AFORS-HET [47]. It can run numerical simulations for various input spectra and do advanced electrical transport simulations within heterostructures. The problem is that some numerical schemes are not fully documented such that the user does not know which numerical method is being used.

2.2. Physical models

The goals of optics are to determine the propagation of light in space-time and its interaction with media. For different length scales one can treat light in different ways.

Whenever the characteristic length scale of a structure is large compared to the light's wavelength one can use the approximations by *geometrical optics* [5]. In geometrical optics one treats light as single rays. For smaller length scales one needs to include the wave-like nature of light thus the *wave model of light*. The wave-like behavior is based upon the electromagnetic description of light via Maxwell's equations.

To acquire a detailed understanding of light one needs to extend the optical models by means of quantum mechanics wherein one treats electromagnetic waves as being comprised of small particles – photons. Thus, the underlying model is called *photon model*.

2.2.1. Geometrical optics and photon model

For structures with length scales considerably larger than the light's wavelength one can treat light as propagating rays. This simplifies the treatment highly and the two resulting phenomenons to consider are *reflection* and *refraction*.

For the mathematical treatment one defines material specific parameters which define the interaction of light with one specific material. Let $n \geq 1$ be the refractive index which indicates the material's phase velocity, and let $\kappa \geq 0$ be the extinction

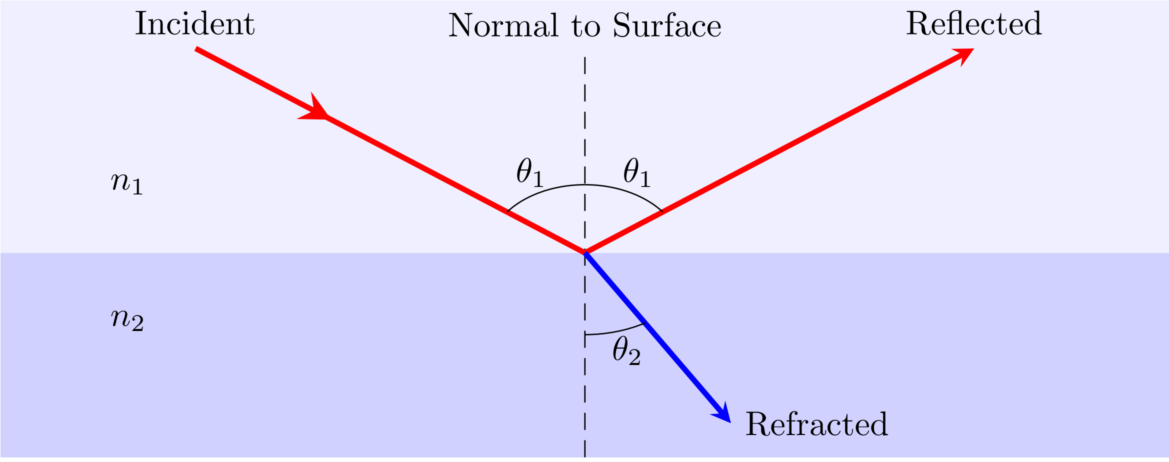

Figure 2.: Typical interaction process of a light ray at an interface governed by the geometrical optic model. The incident ray coming from a medium with refractive index n_1 is partly reflected by the law of reflection. The remainder of the ray is refracted into the medium with refractive index n_2. This sketch represents the case $n_2 > n_1$ which leads by Snell's law to $\theta_2 < \theta_1$.

coefficient which indicates the rate of intensity loss as the wave propagates through that material. Now, the *complex refractive index* $\underline{n} \in \mathbb{C}$ is defined as

$$\underline{n} \coloneqq n - \mathrm{i}\kappa\,. \tag{2.1}$$

For most materials the values for n and κ can be found in the literature, e.g. the “Refractive index database” [30].

In simple scenarios in geometrical optics one looks at a planar interface in between two homogeneous materials. Light rays will travel straight through homogeneous materials and at the interface reflection, and refraction will occur. This process is sketched in Figure 2.

Some parts of the light's intensity will be reflected at the interface (“reflection”) and the exact fraction is given by the *reflectance* R. The remaining part will be transmitted into the attached material which is given by the *transmittance* T. For the special case of a normal incident ray coming from a material with complex reflective index $\underline{n}_1$ and going into a material $\underline{n}_2$ the fractions are given by [5, p. 244]

$$R = \left|\frac{\underline{n}_1 - \underline{n}_2}{\underline{n}_1 + \underline{n}_2}\right|^2\,, \tag{2.2}$$

$$T = 1 - R\,, \tag{2.3}$$

which are derived from the more general Fresnel equations [5, pp. 238, 244]. One should note that refractive indices $\underline{n}_i$ of actual materials are wavelength-dependent. This results into reflectance, and transmittance being wavelength-dependent as well.

Refraction happens when a light ray is transmitted from one medium to another. Let n_i be the refractive indices, and θ_i the angle counted from the surface normal, see

Figure 2. The transmitted ray will bend at the interface according to Snell's law [5, p. 237]

$$\frac{\sin\theta_1}{\sin\theta_2} = \frac{n_2}{n_1} \,.$$

As the light ray propagates through the material its intensity I is partly absorbed for non-vanishing extinction coefficient κ. This leads to a drop in intensity which is given by the *Lambert-Beer law* [5, p. 227]

$$\begin{aligned} I(x,\lambda) =& I_0 \exp(-\alpha x) && (2.4) \\ \alpha :=& \frac{4\pi\kappa}{\lambda} \,, && (2.5) \end{aligned}$$

where $\alpha = \alpha(\lambda)$ is the attenuation coefficient, $I_0 = I_0(\lambda)$ the initial intensity distribution, and $x \geq 0$ the penetration depth. An in-depth derivation is given in Section 2.2.2.

The absorption of light is theoretically explained by quantum mechanics wherein light is treated as a stream of *photons*. Each photon has a specific energy E_γ which is determined by its wavelength λ

$$E_\gamma = \frac{hc}{\lambda} \,, \tag{2.6}$$

where the Planck constant h, and speed of light c are defined in the appendix.
Absorption is interpreted as the annihilation of a photon by the medium which generates so-called *electron-hole pairs*[1]. In first approximation one can assume that all the absorbed energy is used for the creation of electron-hole pairs which leads to the (spectral) generation rate g [21, p. 108]

$$\begin{aligned} g(x,\lambda) :=& \left| \frac{1}{E_\gamma(\lambda)} \frac{\partial I}{\partial x}(x,\lambda) \right| \\ =& \frac{\lambda}{hc} \alpha(\lambda) I_0(\lambda) \exp\bigl(-\alpha(\lambda) x\bigr) \,, \end{aligned}$$

where the change in intensity $\frac{\partial I}{\partial x}$ was scaled by the photon's energy E_γ to get a particle count.
For the (total) generation rate $G = G(x)$ one needs to integrate the spectral generation rate g over the whole spectrum. As will be explained in Section 3.2 the excitation of electrons in semiconductors needs a minimal amount of energy E_{gap} which leads to a vanishing generation rate above a critical wavelength $\lambda_{\max}$ by using equation (2.6)

$$\lambda_{\max} := \frac{hc}{E_{\mathrm{gap}}} \,.$$

---

[1] For a more detailed discussion of electron-hole pairs confer to Section 3.2.1.

Thus, the (total) *generation rate* G is given by

$$\begin{aligned} G(x) &= \int_0^{\lambda_{\max}} g(x,\lambda)\,\mathrm{d}\lambda \\ &= \int_0^{\lambda_{\max}} \frac{\lambda}{hc}\alpha(\lambda)I_0(\lambda)\exp\big(-\alpha(\lambda)x\big)\,\mathrm{d}\lambda\,. \end{aligned} \tag{2.7}$$

2.2.2. From Boltzmann transport equation towards the Lambert-Beer law

A model for light absorption can be gained by postulating a particle transport mechanism using the Boltzmann transport equation for photons. The photon distribution $f = f(\mathbf{x}, \mathbf{p}, t)$ for photons at position $\mathbf{x}$, with momentum $\mathbf{p}$, and time t follows a Boltzmann transport equation

$$\partial_t f + (\mathbf{v}\cdot\boldsymbol{\nabla}_{\mathbf{x}})f + \big(\mathbf{F}\cdot\boldsymbol{\nabla}_{\mathbf{p}}\big)f = \left(\frac{\mathrm{d}f}{\mathrm{d}t}\right)_{\mathrm{coll}}\,. \tag{2.8}$$

Here the velocity $\mathbf{v}$, force $\mathbf{F}$, and the change in net number density induced by collisions $\left(\frac{\mathrm{d}f}{\mathrm{d}t}\right)_{\mathrm{coll}}$ were used. By considering massless photons, and no general relativistic effects one can neglect the momentum derivative

$$\partial_t f + (\mathbf{v}\cdot\boldsymbol{\nabla}_{\mathbf{x}})f = \left(\frac{\mathrm{d}f}{\mathrm{d}t}\right)_{\mathrm{coll}}\,. \tag{2.9}$$

The number of photons at position $\mathbf{x}$, time t, of frequency $(\nu, \nu+\mathrm{d}\nu)$, and unit direction $\hat{\mathbf{n}}$ with solid angle spread $\mathrm{d}\omega$ is given by [29, p. 36]

$$f(\mathbf{x}, \hat{\mathbf{n}}, \nu, t)\,\mathrm{d}\omega\,\mathrm{d}\nu\,.$$

The photon number crossing an area element $\mathbf{d}\boldsymbol{A}$ within time $(t, t+\mathrm{d}t)$, and of velocity $\mathbf{v} = c\hat{\mathbf{n}}$ is

$$f(c\,\mathrm{d}t)(\hat{\mathbf{n}}\cdot\mathbf{d}\boldsymbol{A})\,\mathrm{d}\omega\,\mathrm{d}\nu\,.$$

Finally, the energy transport by photons of energy $E_\gamma = h\nu$ is [29, p. 36]

$$\mathrm{d}E = (h\nu)(cf\cos\theta\,\mathrm{d}A\,\mathrm{d}\omega\,\mathrm{d}\nu\,\mathrm{d}t)\,,$$

where we introduced the angle θ in-between the area $\mathbf{d}\boldsymbol{A}$, and velocity direction $\hat{\mathbf{n}}$ by $\cos\theta\,\mathrm{d}A := \hat{\mathbf{n}}\cdot\mathbf{d}\boldsymbol{A}$. Using the definition of intensity [29, p. 1]

$$dE = I\cos\theta\,\mathrm{d}A\,\mathrm{d}\omega\,\mathrm{d}\nu\,\mathrm{d}t\,,$$

one can readily gather the relation of photon distribution and intensity

$$I = ch\nu f\,. \tag{2.10}$$

The change in photon number is given by the energy of emitted photons E_{emit} minus the absorbed ones E_{abs}, and scaled by the photon's energy [29, p. 36]

$$\left(\frac{\mathrm{d}f}{\mathrm{d}t}\right)_{\text{coll}} = \frac{E_{\text{emit}} - E_{\text{abs}}}{E_\gamma} = \frac{j - \kappa I}{h\nu}\,, \tag{2.11}$$

where the emission coefficient j, and absorption coefficient κ are used.
Substituting the relations (2.11), and (2.10) into the Boltzmann transport equation (2.9) yields the (time-dependent) radiative transfer equation [29, p. 36]

$$\frac{1}{ch\nu}\big(\partial_t I + c(\hat{\mathbf{n}} \cdot \boldsymbol{\nabla}_{\mathbf{x}})I\big) = \frac{j - \kappa I}{h\nu}\,.$$

Generally, one studies the time-independent *radiative transfer equation* [29, p. 36]

$$(\hat{\mathbf{n}} \cdot \boldsymbol{\nabla}_{\mathbf{x}})I = j - \kappa I\,.$$

The reduction towards a one-dimensional model uses a dimension scaling parameter μ [29, p. 36]

$$\mu \frac{\mathrm{d}I}{\mathrm{d}x} = j - \kappa I\,.$$

By neglecting emission within our media we end up with the *Lambert-Beer law*

$$\frac{\mathrm{d}I}{\mathrm{d}x} = -\alpha I\,, \quad \alpha = \alpha(\nu) := \frac{\kappa}{\mu}\,.$$

2.2.3. Spectrum and coherency

A light source emits electromagnetic radiation at different wavelengths. The wavelength-intensity distribution is a key parameter to distinguish between different light sources. This distribution is usually referred to as the light source's *spectrum*.
Our sun emits light with a spectral distribution which is close to an ideal black body light source of around 5800 K. Parts of its emitted spectrum are absorbed as it enters Earth's atmosphere. Thus the light at sea level differs strongly from the ideal black body spectrum. For comparison purposes standardized spectra "AM1.5" were defined by the solar industry which resemble the average spectrum at sea level [37]. The AM1.5 spectrum comes in two flavors: one with just the direct illumination coming from a small solid angle around the sun (AM1.5d), and the other with the total integrated intensity from the half sphere's surface (AM1.5g). Figure 3 compares the ideal black body spectrum to the AM1.5 spectra.

On the other hand, a light source emits waves which interfere with each other. For interference one needs to calculate the superposition of electric, and magnetic field strengths but in real world applications light sources are not ideal. This implies that one introduces the *coherency* effect wherein each wave from the same light source has a maximal interference length – the so-called *coherence length*. For waves which have traveled farther from the source than the coherence length one treats them as being *incoherent*, that is to say that interference does not play a role any more. Thus, one does not superimpose electric, and magnetic field strengths but rather adds their intensities.

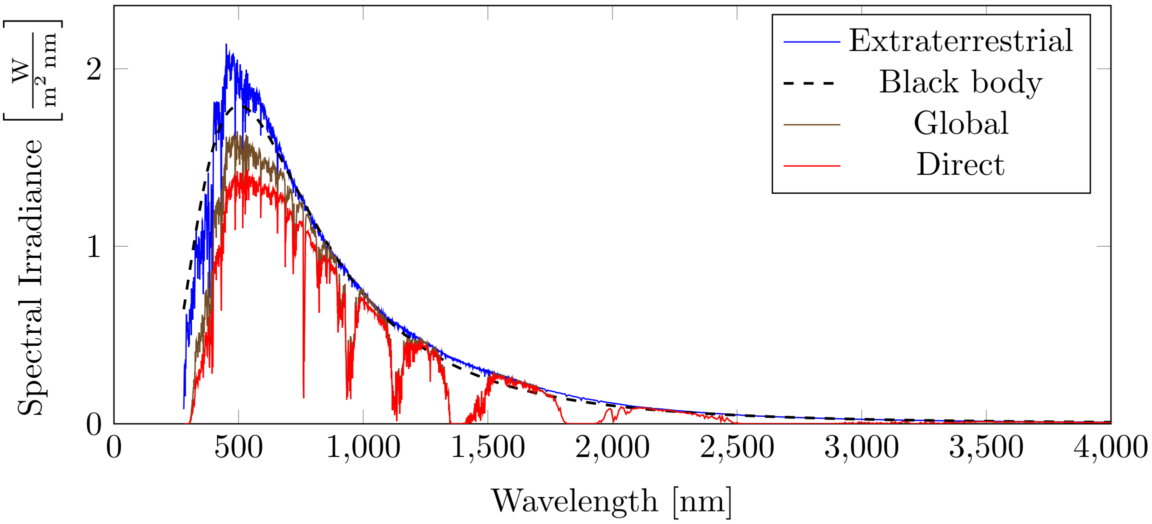

Figure 3.: Different spectra resulting from the sun's radiation are displayed. An ideal black body spectrum for a sun-like source of temperature $T = 5772\,\mathrm{K}$ shining into a solid angle of angular diameter $\alpha = 1919''$ is shown [27]. The extraterrestrial, global, and direct spectra are defined by the standards AM0, AM1.5g, and AM1.5d [37].

2.2.4. Anti-reflection coating

As the sun light reaches the solar cell it is partially reflected at the top interface. One can optimize the top interface's refractive index to decrease the frontal reflection. This is called creating an *anti-reflection coating* (ARC) which is usually compromised of a mixture of different glass plates.

A bare air-silicon interface has more than 30% reflection for most of the sun's spectrum. Even in the simple case of using just one glass plate one can heavily reduce the reflection for important parts of the sun's spectrum. Figure 4 shows the different reflections of a bare air-silicon, air-standard glass-silicon, and air-ARC-silicon interfaces. For simplicity, we assumed that the incident light is perpendicular to the interface.

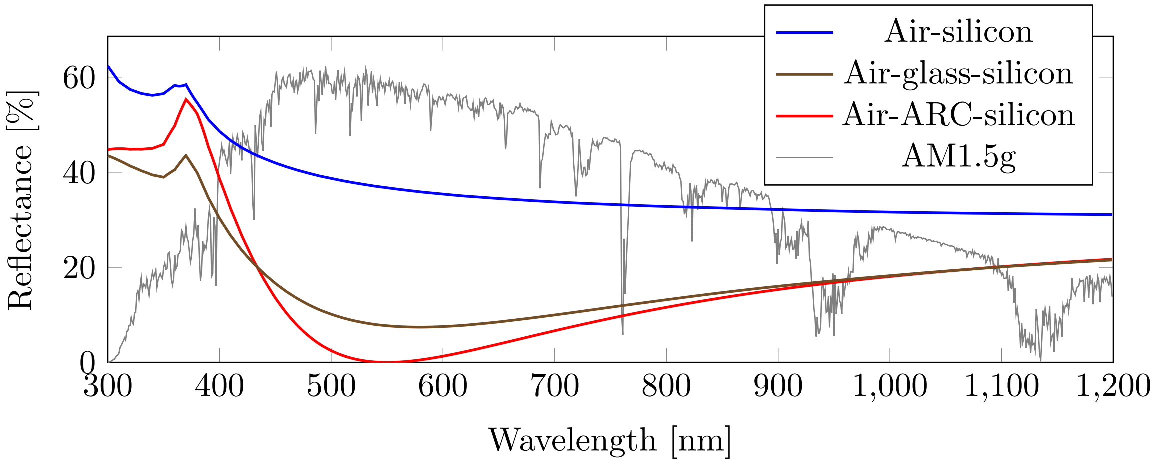

Figure 4.: The result of an anti-reflection coating is illustrated. The bare air-silicon interface reflects very highly compared to air-glass-silicon. The reflectance can be minimized by choosing a specific refractive index. For a refractive index of around $n_{\mathrm{ARC}} = 2.3$ the reflectance at the sun spectrum's peak can be minimized. Hence the name anti-reflection coating (ARC). The typical AM1.5g spectrum is overlayed in the background by transformed units.

2.3. Optical model – 1D Lambert-Beer

A one-dimensional model for the simulation of incoherent light similar to the "Classical optical model" by Krč and Topič [21, p. 22] has been implemented. The treatment of incoherent light is done by propagating intensity distributions through the structure. The solar cell structure is modeled as a multi-layer system consisting of an anti-reflection coating (ARC) at the top, then multiple semiconducting layers of different materials, and a rear contact layer.

2.3.1. Sun light

One of the main ingredients for any optical model is the incident light spectrum. We choose the sun as our light source and the industry standard spectrum AM1.5g, or AM1.5d. The AM1.5 spectra were shown before in Figure 3. The incoming spectrum will be denoted as $I^+_{\mathrm{inc}} = I^+_{\mathrm{inc}}(\lambda)$.

2.3.2. Cell's structure and light path

The cell is modeled as a multi-layer system. It is compromised of an anti-reflection coating at the front, multiple layers used for absorption, and a metallic rear layer. A sketch is given in Figure 5.

Already as light enters the solar cell some parts are reflected and only the remainder is transmitted into the structure. The transmitted part $I^+_{\mathrm{in},1} = I^+_{\mathrm{in},1}(\lambda)$ depends on the

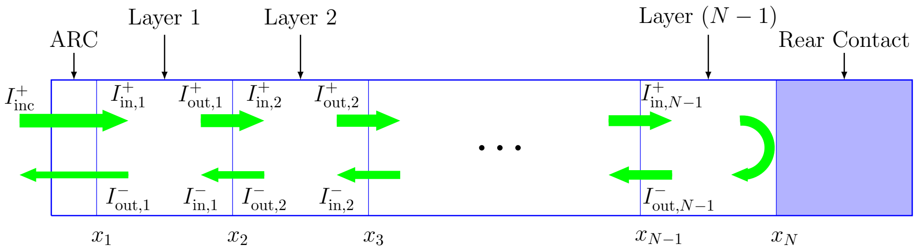

Figure 5.: The model for the solar cell's structure is sketched. Compromising of a frontal anti-reflection layer (ARC), $(N-1)$ bulk layers, and a metallic rear layer. The intensity distribution I is propagated through each layer up to the rear layer and then propagated backwards in a second pass. Interface positions are given by $(x_i)_i$.

transmittance $T_{\text{front}} = T_{\text{front}}(\lambda)$, see equation (2.2), of the anti-reflection coating,

$$I^+_{\text{in},1} \coloneqq T_{\text{front}} I^+_{\text{inc}} \,.$$

The transmitted part travels through the bulk material. The bulk's layers are numbered from 1 at the top to $N-1$ at the bottom and the domain is split up into interface positions $x_1 < x_2 < \cdots < x_N$ where layer i extends from x_i up to x_{i+1}.

Within each layer parts of the spectrum are absorbed. The intensity $I = I(x,\lambda)$ decreases because of absorption according to the Lambert-Beer law, see equation (2.4). Within each layer i it is given by

$$I(x,\lambda) = I^+_{\text{in},i} \exp\bigl(-\alpha_i(x - x_i)\bigr) \,, \quad x \in (x_i, x_{i+1}) \,,$$

where the initial intensity of layer i is given by $I^+_{\text{in},i} = I^+_{\text{in},i}(\lambda)$, and $\alpha_i = \alpha_i(\lambda)$ is its attenuation coefficient.

Once the spectrum passes an interface position x_i its intensity is reduced by reflection. This is included by definitions of the outgoing spectrum $I^+_{\text{out},i-1}$ of layer $i-1$, and the incoming spectrum $I^+_{\text{in},i}$ of the next layer

$$\begin{aligned} I^+_{\text{out},i} &\coloneqq I^+_{\text{in},i} \exp\bigl(-\alpha_i(x_{i+1} - x_i)\bigr) && \text{for} \quad i = 1, \ldots, N-1 \,, \\ I^+_{\text{in},i} &\coloneqq T_{i-1,i}\, I^+_{\text{out},i-1} && \text{for} \quad i = 2, \ldots, N-1 \,. \end{aligned}$$

Here $T_{i-1,i}$ is the transmittance between layer $i-1$ and i, see equation (2.3).

The above formulated equations are used for a model wherein we propagate only the transmitted part and neglect the reflected parts. This is done for all layers 1 through $N-1$ and at the last layer we will calculate the reflected part instead

$$I^-_{\text{in},N-1} \coloneqq R_{\text{rear}}\, I^+_{\text{out},N-1} \,,$$

where the reflectance at the interface of layer $(N-1)$, and the rear is R_{rear}.

Now, we will use the reflected spectrum as initial data for a backwards propagating spectrum (denoted by a minus sign as superscript). The propagation through the bulk layers is handled in a similar manner as for the forward propagating spectrum but the wave will not be reflected at the front again

$$\left.\begin{aligned} I^-_{\text{out},i} &:= I^-_{\text{in},i}\exp\bigl(-\alpha_i(x_{i+1}-x_i)\bigr) \\ I^-_{\text{in},i-1} &:= T_{i-1,i}\, I^-_{\text{out},i} \end{aligned}\right\} \quad \text{for} \quad i = 2, \dots, N-1\,.$$

To underline the physical reasoning as to why we neglect the reflected parts in the cell's bulk we will do some example calculations. As a standard test case one looks at a silicon-gallium arsenide interface (data taken from [35, 33])

$$\begin{aligned} \underline{n}_{\text{Si}}(\lambda = 500\,\text{nm}) &= 4.299 - 0.070\text{i} \\ \underline{n}_{\text{GaAs}}(\lambda = 500\,\text{nm}) &= 4.307 - 0.427\text{i} \\ \Longrightarrow \qquad R &\approx 0.17\%\,. \end{aligned}$$

Thus, for wavelengths around the sun spectrum's peak that interface shows negligible reflectance R. Whereas the reflection of a silver back contact with either material is significantly higher (data taken from [31])

$$\begin{aligned} &\underline{n}_{\text{Ag}}(\lambda = 500\,\text{nm}) = 0.041 - 3.159\text{i} \\ \Longrightarrow \qquad &R_{\text{Si-Ag}} \approx 94\%\,, \quad R_{\text{GaAs-Ag}} \approx 81\%\,. \end{aligned}$$

2.3.3. Anti-reflection coating

The anti-reflection coating's (ARC) purpose is to minimize the reflection at the front surface. For a single ARC layer one needs to choose its refractive index n_{ARC} as the geometric mean of the surrounding air's n_{air} and the bulk's first layer $n_{\text{bulk}} = n_{\text{bulk}}(\lambda)$ [5, p. 326]. As the bulk material's refractive index is wavelength-dependent we choose a value at the wavelength $\lambda_0 = 550\,\text{nm}$ which corresponds roughly to the sun spectrum's peak

$$n_{\text{ARC}} := \sqrt{n_{\text{air}} \cdot n_{\text{bulk}}(\lambda_0)}\,.$$

The ARC's total reflectance R which resembles multiple reflections inside the ARC layer is given by [26, p. 205]

$$\begin{aligned} R &= \frac{n^2_{\text{ARC}}\bigl(n^2_{\text{air}} - n^2_{\text{bulk}}\bigr) - \bigl(n^2_{\text{air}} - n^2_{\text{ARC}}\bigr)\bigl(n^2_{\text{ARC}} - n^2_{\text{bulk}}\bigr)\sin^2\theta}{n^2_{\text{ARC}}\bigl(n^2_{\text{air}} + n^2_{\text{bulk}}\bigr) - \bigl(n^2_{\text{air}} - n^2_{\text{ARC}}\bigr)\bigl(n^2_{\text{ARC}} - n^2_{\text{bulk}}\bigr)\sin^2\theta} \\ &= \frac{r_1^2 + r_2^2 + 2r_1r_2\cos(2\theta)}{1 + r_1^2r_2^2 + 2r_1r_2\cos(2\theta)}\,, \end{aligned}$$

$$\text{with} \quad \begin{cases} r_1 := \dfrac{n_{\text{air}} - n_{\text{ARC}}}{n_{\text{air}} + n_{\text{ARC}}}\,, & r_2 := \dfrac{n_{\text{ARC}} - n_{\text{bulk}}}{n_{\text{ARC}} + n_{\text{bulk}}} \\ \theta := \dfrac{2\pi n_{\text{ARC}} d_{\text{ARC}}}{\lambda}\,, & d_{\text{ARC}} := \dfrac{\lambda_0}{4n_{\text{ARC}}}\,. \end{cases}$$

Figure 4 displays the minimizing result of this ARC layer compared to the bare air-silicon or air-glass-silicon interface.

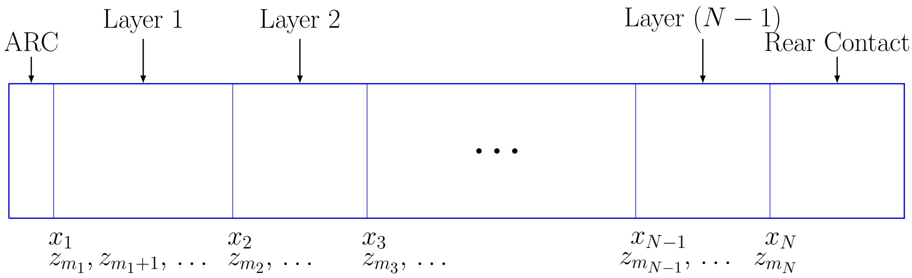

Figure 6.: The solar cell's bulk layers have interfaces at positions $(x_i)_{i=1,\dots,N}$. The total length is discretized uniformly by positions $(z_i)_{i=1,\dots,M}$, and the interfaces are approximated by $x_i \approx z_{m_i}$.

2.3.4. Discretizations

Different input parameters such as the Sun's spectrum or silicon's refractive index are only given at discrete wavelengths. We will discuss their discretizations in this section.

2.3.4.1. Spectrum

The AM1.5 spectra are given in the wavelength range of $\lambda_{\text{min}} = 280\,\text{nm}$ up to $\lambda_{\text{max}} = 4000\,\text{nm}$. It uses a uniform discretization step width of $\Delta\lambda = 0.5\,\text{nm}$ below $\lambda = 400\,\text{nm}$, and $\Delta\lambda = 1\,\text{nm}$ for larger wavelengths. Data sets for other material parameters were not as densely discretized, and because the spectra are peaked within the visible range, $\lambda = (390\text{–}700)\,\text{nm}$, we choose to use only a subset of the spectra given by

$$\lambda_{\text{min}} = 300\,\text{nm}\,, \quad \lambda_{\text{max}} = 1199\,\text{nm}\,.$$

This defines the wavelength's discretization $\lambda = (\lambda_k)_k$, and the incident intensity's $I_0 = \big(I_0(\lambda_k)\big)_k$.

2.3.4.2. Position

The cell's bulk is composed of an $N-1$ layer system with interface positions $x_1 < x_2 < \dots < x_N$ as depicted in Figure 6. We discretize the total length by M equidistant points $z_1 < z_2 < \dots < z_M$ which is far denser than the number of interface positions, i.e. $M \gg N$. The interface positions within the bulk $(x_i)_{i=2,\dots,N-1}$ are replaced by approximations $\big(z_{m_i}\big)_{i=2,\dots,N-1}$ with

$$m_i := \min\left\{ j \in \{1,\dots,M\} \;\middle|\; \big|x_i - z_j\big| = \min_{k=1,\dots,M} |x_i - z_k| \right\},$$

which are also illustrated in Figure 6. Thus, the layer i is given by the following position discretization $z_{m_i} < z_{m_i+1} < \dots < z_{m_{i+1}}$.

Material	Data obtained			Source
	n	κ	$\Delta\lambda$ [nm]	
Silver (Ag)	✓	✓	10	[31]
Aluminum (Al)	✓	✓	5	[32]
Amorphous silicon (a-Si)	✓	✓	5	[47]
Crystalline silicon (c-Si)	✓	✓	2-75	[34, 9]
Silicon nitride (Si_3N_4)	✓		≈ 10	[36]
Hydrogenated amorphous silicon (a-Si:H)	✓	✓	≈ 50	[21, pp. 117-120]
P-type hydrogenated amorphous silicon (p a-Si:H)	✓	✓	≈ 50	[21, pp. 117-120]
N-type hydrogenated amorphous silicon (n a-Si:H)	✓	✓	≈ 50	[21, pp. 117-120]

Table 1.: Different materials are included in our program. This list shows each material, and their obtained optical parameters from its source. The parameters include the refractive index n, and the extinction coefficient κ. Each parameter is wavelength-dependent and the discretization is not the same across different sources. Some are given by a uniform step width $\Delta\lambda$ whereas others have varying accuracies which are denoted by an approximation sign "$\approx$". Crystalline silicon was merged from two different data sets.

2.3.4.3. Complex refractive index

The bulk's materials are partly characterized by each layer's complex refractive index $\underline{n}_i$. The complex refractive index consists of the refractive index n, and the extinction coefficient κ, see equation (2.1). The attenuation coefficient α depends upon the extinction coefficient via equation (2.5) and each of these material parameters is strongly wavelength-dependent.

Our implementation includes varies different materials such as silicon, and gallium arsenide. Table 1 gives a full list of available materials, and the sources where we have gathered the data from.

In all cases the data were given on far too coarsely discretized wavelength grids. To fit the fine grid defined by our incident spectrum, see Section 2.3.4.1, we needed to interpolate the data sets. For this purpose we used cubic spline interpolation.

2.3.5. Generation rate

Absorption and transmission lead to a decrease in intensity. The intensity drop caused by absorption is assumed to generate electron-hole pairs by a generation rate $G = G(x)$ according to equation (2.7). The generation rate is comprised of the forward $G^+ = G^+(x)$ as well as the backward moving part $G^- = G^-(x)$

$$G = G^+ + G^- \,.$$

Each generation rate G^+, G^- consists of an integral which needs to be discretized. For a position z_j within layer i, i.e. $z_j \in [z_{m_i}, z_{m_{i+1}})$, this is done as follows

$$G^+(z_j) = \sum_{k\colon \lambda_k \leq \lambda_i^{\max}} \frac{\lambda_k}{hc} \, \alpha_i(\lambda_k) \, I^+_{\mathrm{in},i}(\lambda_k) \, \exp\Big(-\alpha_i(\lambda_k) \, \big(z_j - z_{m_i}\big)\Big) \, \Delta\lambda \,,$$

$$\text{with} \quad \lambda_i^{\max} := \frac{hc}{E_i^{\mathrm{gap}}} \,,$$

where $\Delta\lambda$ denotes the spectral resolution, and the layer i's band gap is given by E_i^{gap}. The generation rate G^- is discretized in a similar manner with the obvious change in interface position.

2.4. Case studies

We have implemented an optical model to simulate the absorption process governed by the Lambert-Beer law in one dimension. Amongst others, a validation of our implementation will be done in this section as a multi-step process. At first we will check that the anti-reflection coating (ARC) is implemented well and produces fitting reflectance values. Thereafter we will validate the absorption process and its resulting generation rate.

2.4.1. ARC's reflectance

The frontal reflection routine will be tested by two different set-ups. An air-silicon interface as well as an air-ARC-silicon interface are used for the calculation of spectral reflectances given the incident AM1.5d spectrum.

Krč et al. [21, p. 203] have implemented a model for optical simulations which is commercially available. They published data which they have gathered from sample runs.

As the data is accessible only from plots we needed to digitalize them. For this purpose we have used the software engauge [24]. The extraction process is not done in an ideal fashion which leads to the introduction of a further error source. This digitalization error is rather large and we approximated it by a constant systematic error of 0.5% of each axis' length. Thus, the reference data has an estimated wavelength error ϵ_λ, and reflectance error ϵ_R of

$$\epsilon_\lambda = 0.5\% \cdot 800\,\mathrm{nm} = 4\,\mathrm{nm}\,, \quad \epsilon_R = 0.5\% \cdot 0.6 = 0.003\,.$$

Both simulations were done with similar parameter set-ups. An overview is given in Table 2. The exact refractive indices that Krč et al. used were not specified such that we used publicly available data as indicated in the table. Figure 7 shows the reference data compared to the data obtained by our implementation. The upper plot gives the raw data and in the lower shows pointwise errors.

The two implementations result into slightly different reflectance values for the simple

Parameter		Air-silicon	Air-ARC-silicon
Incident spectrum		AM1.5d	AM1.5d
Air's refractive index	n_{air}	1	1
Air's extinction coefficient	κ_{air}	0	0
ARC's material		–	Si_3N_4
ARC's depth	d_{ARC}	–	70 nm
ARC's refractive index	n_{ARC}	–	(see Table 1)
ARC's extinction coefficient	κ_{ARC}	–	(see Table 1)
Bulk's material		Si	Si
Bulk's refractive index	n_{bulk}	(see Table 1)	(see Table 1)
Bulk's extinction coefficient	κ_{bulk}	(see Table 1)	(see Table 1)
Minimal wavelength	$\lambda_{\min}$	400 nm	400 nm
Maximal wavelength	$\lambda_{\max}$	1199 nm	1199 nm
Wavelength step width	$\Delta\lambda$	1 nm	1 nm

Table 2.: Parameters used to simulate an air-silicon, and an air-ARC-silicon front interface. The air, and bulk are characterized by their refractive indices $n_{\text{air}}, n_{\text{bulk}}$, and extinction coefficients $\kappa_{\text{air}}, \kappa_{\text{bulk}}$. An ARC layer is specified by its material, depth d_{ARC}, and refractive index n_{ARC}. The uniform wavelength discretization is given by $\lambda_{\min}, \lambda_{\max}, \Delta\lambda$.

"bare" air-silicon interface as can be seen from the middle error plot. The difference of both results was measured using scaled L^p-norms and their values are displayed in Table 3. The errors are below 1% for all norms which show good agreement of the data in all aspects. By observing the middle error plot one can argue that the seen difference might solely result from the errors introduced by the digitalization process. The lower plot depicts the pointwise difference of Krč's data to our own implementation's. Here a relative error would diverge as the data should tend to zero and even small differences result into a large relative error. The error marks tend around the zero mark line for most of the time except for smaller wavelengths. The L^p-norms from Table 3 are around 2%-5% which is larger than from the bare interface. This could again result from the fact that we might use different material parameters compared to the implementation by Krč.

2.4.2. Generation rate – constant model

At first the generation rate will be validated for a test case of constant parameters, i.e. wavelength-independent values. Thus the generation rate has an exact solution which can be expressed analytically. As a reference we have chosen the GUI program AFORS-HET by the Helmholtz Zentrum Berlin [47].

We will consider a layer-structure in the form of air-silicon-air. The silicon layer's depth L is uniformly discretized by M nodes. The optical parameters of refractive index and extinction coefficient are given by the wavelength-independent constants

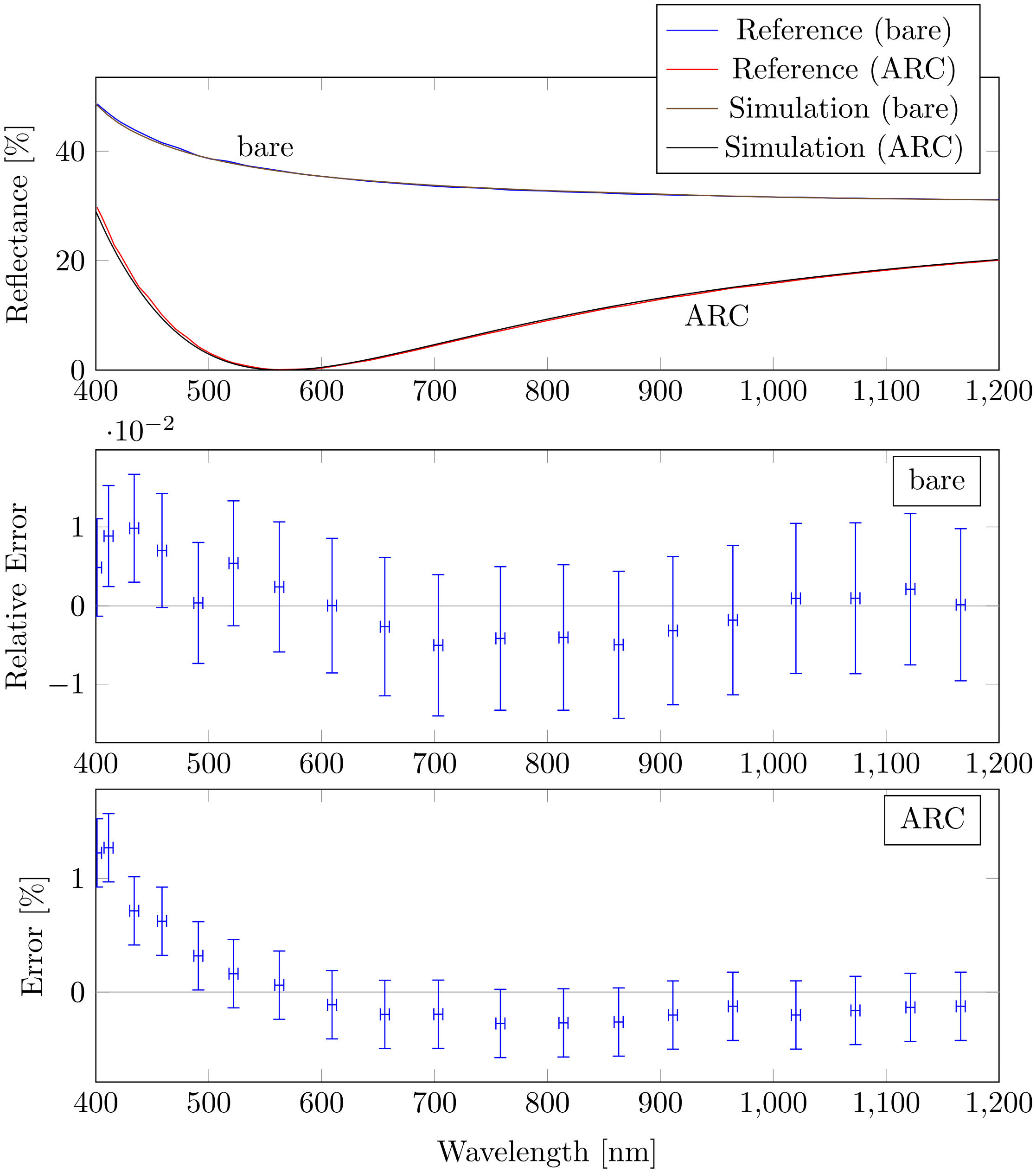

Figure 7.: Reflectance values for a bare air-silicon, and an air-ARC-silicon interface were computed. The upper figure shows the reference data obtained from the book by Krč [21, p. 203] as well as from our own simulation. The reference data has been taken from published plots which introduced a “digitization” error and is estimated by error bars in the lower two plots. Data for the bare interface is analyzed by its relative error in the middle plot and the relativized digitizing error has been overlayed. The lower plot shows the pointwise error for the ARC interface together with the digitizing error. Only some data points are shown in the error plots for visibility.

p-Norm	$\dfrac{\left\Vert R^{(\text{bare})}_{\text{Sim}} - R^{(\text{bare})}_{\text{Ref}} \right\Vert_p}{\left\Vert R^{(\text{bare})}_{\text{Ref}} \right\Vert_p}$	$\dfrac{\left\Vert R^{(\text{ARC})}_{\text{Sim}} - R^{(\text{ARC})}_{\text{Ref}} \right\Vert_p}{\left\Vert R^{(\text{ARC})}_{\text{Ref}} \right\Vert_p}$
1	0.003	0.025
2	0.004	0.027
∞	0.009	0.046

Table 3.: Reflectances at an air-silicon interface $R^{(\text{bare})}_{\text{Sim}}$, and at an air-ARC-silicon interface $R^{(\text{ARC})}_{\text{Sim}}$ were calculated. Reference data $R^{(\text{bare})}_{\text{Ref}}, R^{(\text{ARC})}_{\text{Ref}}$ were obtained from Krč [21, p. 203]. The errors for each interface type were calculated using L^p-norms and scaled by the reference reflectance's norm.

$n_{\text{air}}, \kappa_{\text{air}}$ for the air layers, and respectively $n_{\text{Si}}, \kappa_{\text{Si}}$ for the silicon layer. The spectrum's irradiance I is taken to be the constant $I(\lambda) \equiv I_0$. The wavelength interval is discretized with a constant step width $\Delta\lambda$ in between $\lambda_{\min}, \lambda_{\max}$. Furthermore, we specify silicon's band gap by E_{gap} and all parameters' values are explicitly stated in Table 4.
The reference program needed some further tweaking to represent the desired model. The air and silicon layer were set as incoherent. As the program needs contacts, and interfaces at the front, and back they were set as plane, non-absorbing, and non-reflecting interfaces. The absorbing silicon layer was also set as incoherent and all the recombinations processes were disabled.

The generation rate is given by the general equation (2.7). For the case of constant parameters it simplifies to

$$G(x) = C \int_{\lambda_{\min}}^{\widetilde{\lambda}_{\max}} \exp\left(-\frac{\Lambda}{\lambda}\right) \mathrm{d}\lambda \,,$$

$$\text{with} \quad \begin{cases} C := \dfrac{\alpha_{\text{Si}} I_0}{E_\gamma} = \dfrac{4\pi k_{\text{Si}} I_0}{hc} \\ \widetilde{\lambda}_{\max} := \dfrac{hc}{E_{\text{gap}}} < \lambda_{\max} \\ \Lambda := 4\pi k_{\text{Si}} x \,, \end{cases}$$

where we have used definitions (2.5), (2.6).
The integral can be expressed via its antiderivative F by

$$\int_{\lambda_{\min}}^{\widetilde{\lambda}_{\max}} \exp\left(-\frac{\Lambda}{\lambda}\right) \mathrm{d}\lambda = F\left(\widetilde{\lambda}_{\max}\right) - F(\lambda_{\min}) \,,$$

$$\text{with} \qquad F(\lambda) := \lambda \exp\left(-\frac{\Lambda}{\lambda}\right) + \Lambda \, \mathrm{Ei}\left(-\frac{\Lambda}{\lambda}\right) ,$$

where the special **exponential integral** function Ei has been introduced

$$\mathrm{Ei}(x) := -\int_{-x}^{\infty} \frac{e^{-t}}{t} \, \mathrm{d}t \,, \quad x \neq 0 \,.$$

Parameter		Value
Length	L	$1\,\mu\mathrm{m}$
Discretization points	M	1000
Air's refractive index	n_{air}	1
Air's extinction coefficient	κ_{air}	0
Bulk's refractive index	n_{Si}	4
Bulk's extinction coefficient	κ_{Si}	1
Bulk's band gap	E_{gap}	$1.124\,\mathrm{eV}$
Spectral irradiance	I_0	$1.5\,\frac{\mathrm{W}}{\mathrm{m}^2\,\mathrm{nm}}$
Wavelength's step width	$\Delta\lambda$	$1\,\mathrm{nm}$
Wavelength's lower limit	λ_{min}	$300\,\mathrm{nm}$
Wavelength's upper limit	λ_{max}	$1199\,\mathrm{nm}$

Table 4.: The constant model's parameters are defined in this table. An air-silicon-air system is looked at with refractive indices $n_{\mathrm{air}}, n_{\mathrm{Si}}$, and extinction coefficients $\kappa_{\mathrm{air}}, \kappa_{\mathrm{Si}}$. The silicon's length L is discretized by M equidistant points, and its band gap is given by E_{gap}. The spectrum is given by a flat profile of I_0 with the wavelength discretization of $\lambda_{\mathrm{min}}, \lambda_{\mathrm{max}}, \Delta\lambda$.

Thus the exact solution for this scenario is given by

$$G(x) = \begin{cases} C\Big(F\big(\widetilde{\lambda}_{\mathrm{max}}\big) - F(\lambda_{\mathrm{min}})\Big)\,, & x > 0 \\ C\big(\widetilde{\lambda}_{\mathrm{max}} - \lambda_{\mathrm{min}}\big)\,, & x = 0\,. \end{cases} \tag{2.12}$$

Now we can do a three-way validation of our model compared to the reference data obtained from AFORS-HET as well as to the exact solution. In the upper plot of Figure 8 one can see the raw data of the exact solution, AFORS-HET, and from our own simulation. As the documentation of the reference program did not mention which quadrature rule they used for the general generation rate integral (2.7) we implemented a midpoint and a trapezoidal rule. The lower plot of Figure 8 shows the relative error w.r.t. the exact solution. We deduced from it that AFORS-HET also implemented the midpoint rule.

In general the results show excellent agreement of the reference data and our simulation with the midpoint rule implementation. Even as the trapezoidal rule shows better results when compared to the exact solution, i.e. the relative error has a smaller absolute value, we will still be using the midpoint implementation for the next validations. The reason being that we will be using AFORS-HET as our source of reference data. Furthermore, if more accurate results are needed one can easily switch to the trapezoidal rule within our implementation.

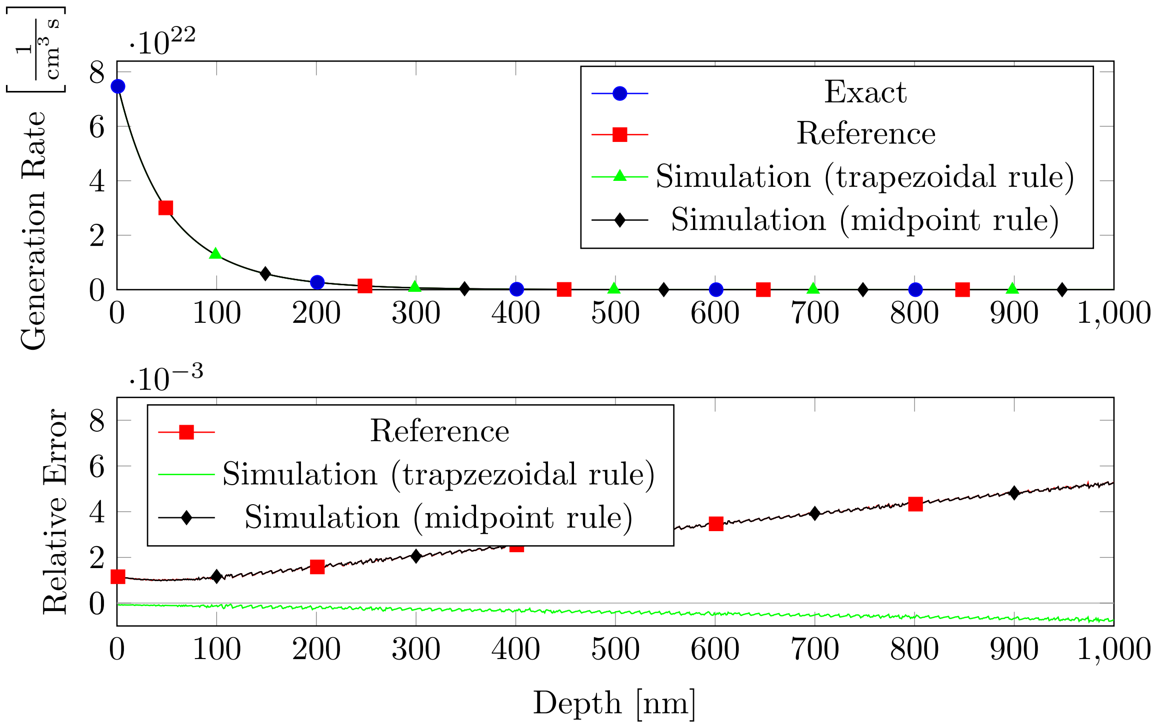

Figure 8.: An air-silicon-air layer system is treated with constant optical parameters. The total length L is uniformly divided by M points. The spectrum is taken to be constant as well with an irradiance I_0 and all values are specified in Table 4.
The upper plot shows the raw generation rate of the exact solution (2.12), reference data obtained from [47], and our simulation using midpoint, and trapezoidal integration rules.
The lower plot shows their relative error w.r.t. the exact solution.

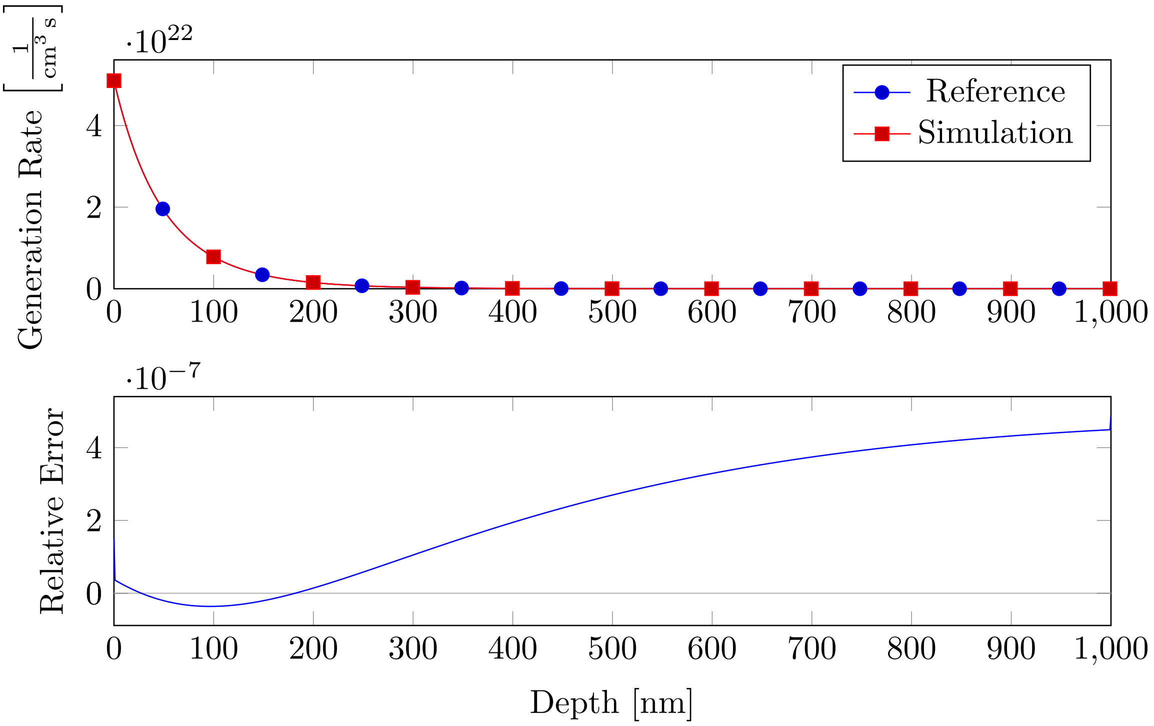

Figure 9.: An air-silicon-air layer system is treated with constant optical properties. The total length L is uniformly divided by M points. As incident spectrum the AM1.5g spectrum is chosen with wavelength limits $\lambda_{\text{min}}, \lambda_{\text{max}}$, and uniform step width $\Delta\lambda$. All constant values are specified in Table 4.
The upper plot shows the raw generation rate of reference data by AFORS-HET [47], and by our simulation. The lower plot shows the relative error of both data sets.

2.4.3. Generation rate – AM1.5

As our next step we will check our implementation with the real-world spectrum AM1.5. As the spectrum does not have a closed-form we cannot find an exact solution and can only validate against the reference program AFORS-HET [47].

The simulation is done for the same air-silicon-air layer setup as in the previous section. The material parameters can be reviewed again from Table 4 with the important change that the irradiance I is not anymore the constant value I_0. As irradiance we have chosen the standard solar spectrum AM1.5g which was discussed in Section 2.2.3. The wavelength limits $\lambda_{\text{min}}, \lambda_{\text{max}}$, and discretization step width $\Delta\lambda$ are specified in Table 4.

The data obtained from the reference program, and from our implementation are displayed in Figure 9. The upper plot shows the raw data and their relative error is shown in the lower plot. One can see the excellent agreement of both data sets as the relative error has a small order of magnitude.

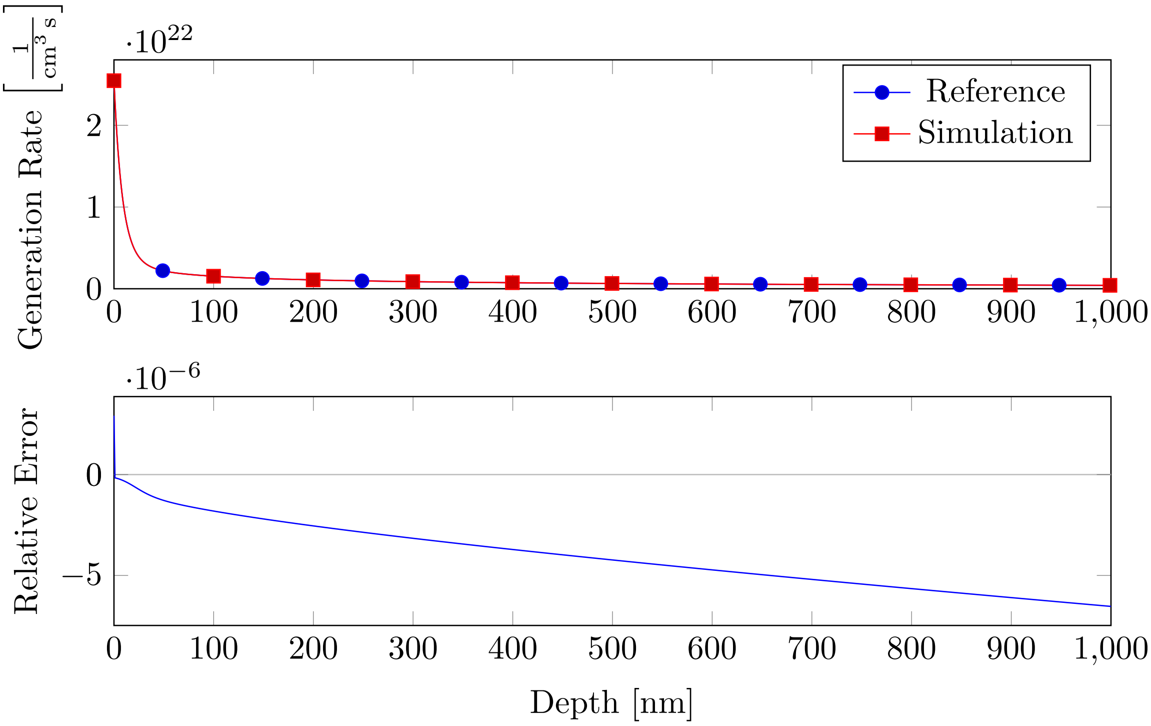

Figure 10.: An air-silicon-air layer system is treated with wavelength-dependent optical properties. The total length L is uniformly divided by M points. We have chosen a constant incident light spectrum. All constant values are specified in Table 4.

The upper plot shows the raw generation rate of reference data by AFORS-HET [47], and by our simulation. The lower plot shows the relative error of both data sets.

2.4.4. Generation rate – crystalline silicon

To resemble real-world materials our implementation also handles non-constant optical material parameters. The two important parameters to note are the refractive index n, and the extinction coefficient κ, see Section 2.2.1.

We will test our implementation by a similar model as before consisting of a one layer air-silicon-air setup. The simulation and discretization constants are the same as before which were given in Table 4. As layer material we have chosen crystalline silicon which leads to wavelength-dependent refraction index $n_{\mathrm{Si}} = n_{\mathrm{Si}}(\lambda)$, and extinction coefficient $\kappa_{\mathrm{Si}} = \kappa_{\mathrm{Si}}(\lambda)$. The AFORS-HET program is used as reference again.

The results obtained from the reference program, and our own implementation are displayed in the upper plot of Figure 10. One can see the good agreement of both data sets as one checks the relative error in the lower plot. The relative error is in the order of 10^{-6} which sounds reasonable as the reference program only works with an accuracy of 10^{-7}.

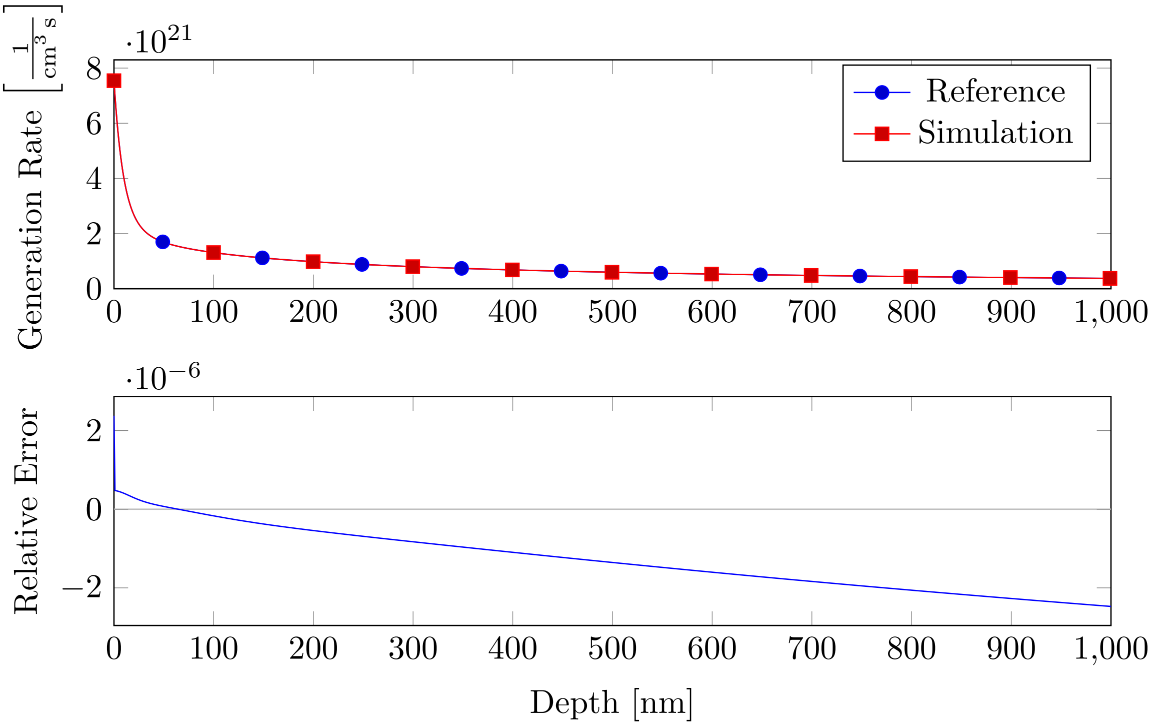

Figure 11.: An air-silicon-air layer system is treated with wavelength-dependent optical properties. The total length L is uniformly divided by M points. As incident spectrum the AM1.5g spectrum is chosen with wavelength limits $\lambda_{\text{min}}, \lambda_{\text{max}}$, and uniform step width $\Delta\lambda$. All constant values are specified in Table 4.
The upper plot shows the raw generation rate of reference data by AFORS-HET [47], and by our simulation. The lower plot shows the relative error of both data sets.

2.4.5. Generation rate – varying model

The combination of wavelength-dependent material parameters and spectrum will be looked upon in this section. The general setup is chosen as before to be a one-layer system consisting of air-silicon-air and the simulation constants are the same as in Table 4. The spectrum is set to be the AM1.5g and the material is crystalline silicon. Both data sets were taken from the AFORS-HET program and interpolated to fit into the wavelength range's discretization specified in Table 4.

Figure 11 displays the raw data of our implementation, and AFORS-HET in the upper plot. The lower plot shows the relative error which lets us conclude that both programs produce very similar results.

Parameter		Value
Length	L	$0.1\,\mu\text{m}$
Spatial nodes	M	1000
Bulk material		c-Si
Incident spectrum		AM1.5g
Minimal wavelength	λ_{min}	300 nm
Maximal wavelength	λ_{max}	1199 nm
Step width	$\Delta\lambda$	$(0.5, \ldots, 100)$nm

Table 5.: Simulations were run to test the dependence of generation rate upon the wavelength discretization. The exact values used are shown here. The step width of $\Delta\lambda = 0.5\,\text{nm}$ represents the exact spectrum and it was varied with logarithmically spaced steps from 1 nm to 100 nm.

2.4.6. Wavelength's sensitivity

The spectrum and material parameters have been sampled by a uniform wavelength discretization of $\Delta\lambda = 1\,\text{nm}$. This discretization choice is arbitrary and we will test the final generation rate's sensitivity on this parameter.

As incident light spectrum we have chosen the standard AM1.5g. The structure was chosen to be a one-layer system of crystalline silicon with length L. The spatial position is uniformly discretized by M nodes. The incident spectrum is propagated once through the whole structure without any reflection effects.

The AM1.5g spectrum is defined by a piecewise uniformly discretization of $\Delta\lambda = 0.5\,\text{nm}$ for wavelengths below $\lambda = 400\,\text{nm}$ and $\Delta\lambda = 1\,\text{nm}$ for larger wavelengths. The material parameters have different discretizations depending on material and source, see Section 2.3.4.3. The data sets were interpolated by cubic splines in the range of λ_{min} up to λ_{max} by different constant step widths $\Delta\lambda$. The exact values used are gathered in Table 5.

The computed generation rates are shown in the left picture of Figure 12. The data sets seem to match for step widths below $\Delta\lambda = 47\,\text{nm}$ and we will use the following scheme to measure the accuracy. The solution obtained from the discretization by the AM1.5 spectrum is treated as the "exact" solution G^*. Generation rates $G = G(\Delta\lambda)$ obtained for larger step widths $\Delta\lambda$ are measured by the following norms[2] $|\cdot|_{\tilde{\ell}^p}$

$$|G|_{\tilde{\ell}^p} := \frac{\|G^* - G\|_{\ell^p}}{\|G^*\|_{\ell^p}}, \quad p = 1, 2, \infty\,. \tag{2.13}$$

This definition arose from the idea that G^* is viewed as our exact solution and one wants to measure the "difference" introduced by using a coarser grid. We have decided to use the ℓ^p-norms as they measure sizes of vectors, and by dividing through $\|G^*\|_{\ell^p}$ we normalize it towards an average error. We have explicitly not chosen L^p-norms as

---

[2] The functions $|\cdot|_{\tilde{\ell}^p}$ are not *norms* in the mathematical sense but rather measuring functions of the relative distance towards the element G^*. Nonetheless we will call them norms for convenience.

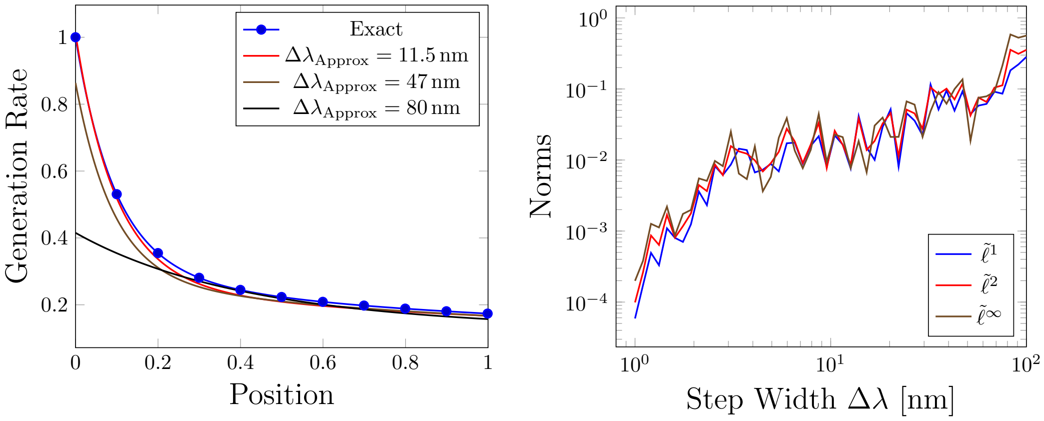

Figure 12.: The left image shows the generation rate for different step widths of the wavelength discretization. We have scaled the generation rates by the maximal value of the “exact” graph which has been calculated using the AM1.5g spectrum’s discretization ($\Delta\lambda = 0.5\,\text{nm}, 1\,\text{nm}$). Generation rates using coarser discretizations are also shown.
The right plot shows the errors of generations rate using different step widths calculated by the specialized norms $|\cdot|_{\tilde{\ell}^p}$, see equation (2.13).

they can be closely approximated by our normalized ℓ^p-norms for uniform grids which are a lot easier to compute.
The right plot of Figure 12 displays these values of $|G|_{\tilde{\ell}^p}$ for different grids. One can see that there is a large error introduced as one uses grids with step widths above two nm. We conclude that one should use the finest available grids as even for simple layer setups the errors tend to become large very fast.

2.4.7. Position’s sampling rate

The generation rate has been calculated along the depth of the solar cell by using a uniformly distributed grid. In previous runs the node number M was set fixed to 1000 and we will investigate if this number is reasonable.

For this purpose we have done simulations similar to the one from Section 2.4.6. The cell is again modeled by a single crystalline silicon layer of length L with a uniform grid of M nodes. As incident spectrum we have chosen the standard “AM1.5g” in between λ_{min}, and λ_{max} (see Section 2.3.4.1) which is propagated once through the whole structure. The exact values are gathered in Table 6.
To investigate the generation rate’s convergence rate we have calculated a generation rate G^* on a very dense grid using M^* nodes. The generation rate G^* is treated as the “exact” solution and other generation rates will be compared to it. For the purpose of comparing we define a norm $|\cdot|_{\tilde{L}^p}$ similar to the one defined in equation (2.13) but using integral L^p-norms instead. Let the generation rates using only $M \ll M^*$ nodes

Parameter		Value
Length	L	0.1 µm
Spatial nodes	M	10,20,50,100,500,1000,5000
“Exact” node	M^*	10^5
Bulk material		c-Si
Incident spectrum		AM1.5g
Minimal wavelength	$\lambda_{\min}$	300 nm
Maximal wavelength	$\lambda_{\max}$	1199 nm
Step width	$\Delta\lambda$	0.5 nm

Table 6.: Simulations were run to test the dependence of generation rate upon the spatial discretization. The exact values used are shown here. The positional node number M^* represents the exact solution.

be given by $G = G(M)$ such that

$$|G|_{\tilde{L}^p} := \frac{\|G^* - G\|_{L^p}}{\|G^*\|_{L^p}}, \quad p = 1, 2, \infty\,. \tag{2.14}$$

We have interpolated the generation rates $G(M)$ to fit the finer grid of G^* by using cubic splines. The integrals within the L^1, L^2-norms were approximated by a trapezoidal integration rule.

In Figure 13 one can see the raw generation rate using only $M = 10, 20$ nodes compared to the “exact” solution using $M^* = 10^5$ nodes.
The convergence rate will be calculated using the introduced measuring functions $|\cdot|_{\tilde{L}^p}$, see equation (2.14). Their obtained values are displayed within a double logarithmic plot in Figure 14. We have fitted linear polynomials $f_p = f_p(x; a_p, b_p)$

$$f_p(x; a_p, b_p) = a_p x + b_p\,, \quad p = 1, 2, \infty\,, \tag{2.15}$$

to the logarithmic data sets $\big(\log M, \log |G(M)|_{\tilde{L}^p}\big)_M$ such that the following should hold

$$f_p(\log M) \approx \log |G(M)|_{\tilde{L}^p}\,, \quad p = 1, 2, \infty\,.$$

The fitted polynomials are shown on top of the data points in Figure 14 and their residuals are also displayed. The polynomials agree good with the data sets, and their residuals show no obvious or strong dependencies. Together with the statistical fitting characteristics from Table 7 one can conclude that the double logarithmic data points show linear dependencies.
From Table 7 one can gather that the convergence rate for the error (calculated by $|\cdot|_{\tilde{L}^p}$) is around 4.4 computed by the L^1-norm, respectively 4.3 by the L^2-norm, and 3.9 by the L^∞-norm.

We con now answer our initial question using the errors $|\cdot|_{\tilde{L}^p}$ shown in Figure 14. Even a node number $M = 100$ would have given a solution with errors below 10^{-5}. We

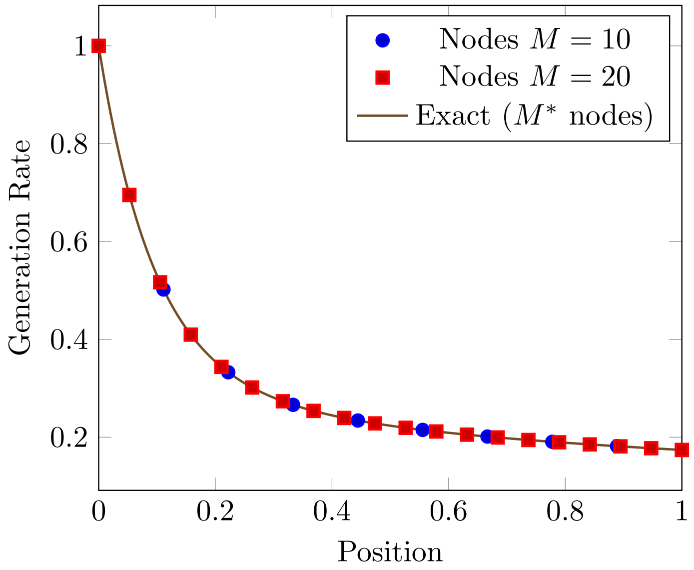

Figure 13.: Generation rates G for different node numbers M are shown. The position is scaled by the length L, and generation rates were scaled by the maximum of the “exact” solution using M^* nodes, see Table 6 for parameter values.

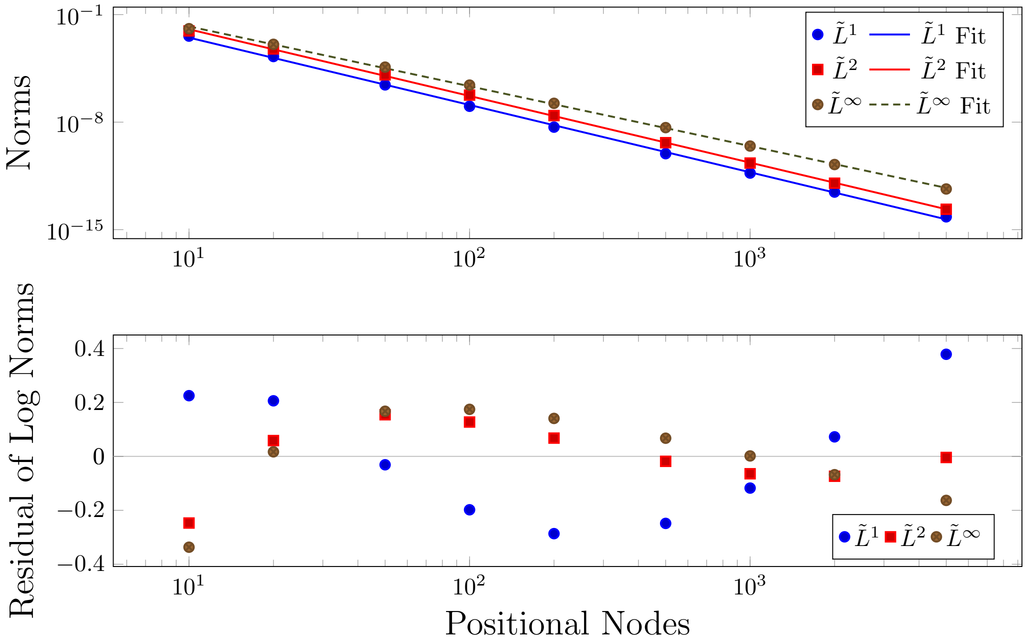

Figure 14.: The upper plots show the calculated values from measuring functions $|\cdot|_{\tilde{L}^p}$ (denoted just by “$\tilde{L}^p$”) for different node numbers M. Alongside the data their fits by functions f_p of type (2.15) are given by “$\tilde{L}^p$ Fit”. The lower plot shows the obtained residuals calculated from the double logarithmic data sets $\left(\log M, \log |G(M)|_{\tilde{L}^p}\right)_M$.

Parameter		$\tilde{L}^1$	$\tilde{L}^2$	$\tilde{L}^\infty$
p-norm	p	1	2	∞
Fit parameter	a_p	-4.38	-4.34	-3.89
Fit parameter	b_p	4.34	5.49	4.89
Lower bound	a_p^-	-4.48	-4.39	-3.97
Upper bound	a_p^+	-4.28	-4.29	-3.82
Lower bound	b_p^-	3.77	5.19	4.48
Upper bound	b_p^+	4.91	5.78	5.30
Residual sum of squares	RSS	0.440	0.119	0.228
Coefficient of determination	R^2	0.999	1.000	1.000
Degrees of freedom	DoF	7	7	7
Adjusted R^2	R^2_{adj}	0.999	1.000	1.000
Root-mean-square error	$RMSE$	0.251	0.130	0.180

Table 7.: The linear polynomials f_p have two parameters a_p, b_p, see equation (2.15). The values obtained from fitting the polynomials to the double logarithmic data sets $\left(\log M, \log |G(M)|_{\tilde{L}^p}\right)_M$ are shown here. Their 95% confidence intervals are given by $(a_p^-, a_p^+), (b_p^-, b_p^+)$. For each fit the standard statistical parameters $(RSS, R^2, Dof, R^2_{\text{adj}}, RMSE)$ are also given.

conclude that for simple one-layer structures the high node number $M = 1000$ is not worth the time consumption as the material data sets introduce far greater errors.

2.5. Lambert-Beer vs. Yee model

2.5.1. Wave model of light

A more accurate approach than possible by geometrical optics for the propagation of light is given by *electrodynamics*. Within electrodynamics light is treated as an electromagnetic wave which is governed by *Maxwell's equations*. Maxwell's equations are a system of coupled, partial differential equations and in differential form using the SI unit system they are given as [15, p. 2]

$$\boldsymbol{\nabla} \cdot \mathbf{B} = 0\,, \qquad \boldsymbol{\nabla} \times \mathbf{E} + \frac{\partial \mathbf{B}}{\partial t} = 0 \tag{2.16}$$

$$\boldsymbol{\nabla} \cdot \mathbf{E} = \frac{\rho}{\epsilon_0}\,, \qquad \boldsymbol{\nabla} \times \mathbf{B} - \frac{1}{c^2}\frac{\partial \mathbf{E}}{\partial t} = \mu_0 \mathbf{J}\,, \tag{2.17}$$

The *independent* variables are given by position $\mathbf{x}$ and time t. The *dependent* variables are the electric field $\mathbf{E} = \mathbf{E}(\mathbf{x}, t)$, magnetic field $\mathbf{B} = \mathbf{B}(\mathbf{x}, t)$, displacement field $\mathbf{D} = \mathbf{D}(\mathbf{x}, t)$, and magnetizing field $\mathbf{H} = \mathbf{H}(\mathbf{x}, t)$. As *source terms* there are the electric charge density $\rho = \rho(\mathbf{x}, t)$, and electric current density $\mathbf{J} = \mathbf{J}(\mathbf{x}, t)$. Constants to the partial differential equations are the the vacuum permittivity ϵ_0, vacuum permeability μ_0, and speed of light c. Their values are given in the appendix.

To solve the equations one has to introduce *material laws*

$$\mathbf{D} = \mathbf{D}(\mathbf{E}, \mathbf{H})\,, \quad \mathbf{B} = \mathbf{B}(\mathbf{E}, \mathbf{H})\,.$$

The so-called *linear non-dispersive materials* are given by the following simplification

$$\mathbf{D} = \epsilon \mathbf{E}\,, \quad \mathbf{B} = \mu \mathbf{H}\,,$$

where we introduced the electric permittivity ϵ, and magnetic permeability μ. In general, both quantities are position-dependent tensors $\epsilon = \epsilon(\mathbf{x}), \mu = \mu(\mathbf{x}) \in \mathbb{R}^{3\times3}$. Usual approximations are given by *isotropic materials* $\epsilon = \epsilon(\mathbf{x}), \mu = \mu(\mathbf{x}) \in \mathbb{R}$, or *homogeneous materials* $\epsilon, \mu \equiv \text{const}$.

The Maxwell's equations are subject to a compatibility condition acting on the source terms which can be interpreted as a *charge conservation law* [48]

$$\frac{\partial \rho}{\partial t} + \boldsymbol{\nabla} \cdot \mathbf{J} = 0\,. \tag{2.18}$$

Another constitutive law is *Ohm's law*

$$\mathbf{J} = \sigma \mathbf{E} + \mathbf{J}_{\text{appl}}\,,$$

for a given *conductivity* $\sigma = \sigma(\mathbf{x}) > 0$, and applied current density $\mathbf{J}_{\text{appl}} = \mathbf{J}_{\text{appl}}(\mathbf{x})$.

After Fourier-transformation one works with position x, and frequency ω dependent fields $\mathbf{E} = \mathbf{E}(\mathbf{x}, \omega), \mathbf{H} = \mathbf{H}(\mathbf{x}, \omega)$. The *generation rate* $G = G(\mathbf{x})$ can be calculated via [25]

$$G(\mathbf{x}) = \int_{\Omega_{\text{AM1.5}}} \frac{\epsilon'' |\mathbf{E}|^2}{2\hbar}\, \mathrm{d}\omega\,, \tag{2.19}$$

where $\epsilon'' = \operatorname{Im}\epsilon$ is the imaginary part of the electric permittivity ϵ of the semiconducting material, and $\int_{\Omega_{\mathrm{AM1.5}}} \cdot \, d\omega$ represents a weighted integration over the incident AM1.5 spectrum in frequency domain.

2.5.2. Yee model

The Maxwell's equations (2.16) and (2.17) can be solved by a scheme introduced in 1966 by Kane Yee [55]. It approximates the Maxwell's equations with a second order accurate scheme by central finite differences in space-time. The time and space steppings are carefully chosen to ensure numerical stability. The electric and magnetic fields are solved for on a staggered space grid by a fully explicit scheme.

The idea to simulate the absorption by this rigorous Maxwell solver is quite different to the absorption by the Lambert-Beer model. Here the cell is illuminated only by monochromatic light sources. For each source the electric, and magnetic field strengths $\mathbf{E}, \mathbf{B}$ are solved for and then the generation rate is calculated via equation (2.19). Finally, the generation rates are averaged using weights from the incident light spectrum.

2.5.3. Lambert-Beer vs. Yee model

The Yee model should yield promising results, and the comparison to the simpler Lambert-Beer model is of great interest. We have implemented a rigorous Maxwell solver on the basis of the Yee model which solves the Maxwell's equations in two dimensions. By averaging one can get one-dimensional results which will be compared to the results from our Lambert-Beer implementation.

Our general setup was chosen to be a single layer crystalline silicon cell of length L. As incident spectrum we choose the standard AM1.5g spectrum in the range of λ_{min} to λ_{max}.

The Lambert-Beer simulation (dubbed “O1LB”) used a rear contact made of silver. The material parameters were interpolated by cubic splines to fit the discretization of the AM1.5 spectrum (see Section 2.3.4.1) which is quite dense – using step widths in the order of $\Delta\lambda = 1\mathrm{nm}$. The depth of the cell is uniformly sampled by M nodes.

The Yee implementation (dubbed “FDTD”) is run for an ideally conductive back layer which is important as it is an approximation to the silver rear contact layer of the O1LB setup. The material parameters, and incident spectrum are spectrally resolved by a different node numbers N. The Lambert-Beer simulation uses node numbers of around $N = 1000$. For the Yee implementation we will only be able to run simulations in the order of $N \approx 100$ because the computations were consuming too much resources – more than 300 GB of RAM were needed to run the simulation for $N = 100$. All parameters' values are gathered in Table 8.

Figure 15 shows the calculated generation rates by comparison. Both generation rates show the same overall behavior and are of the same order of magnitude but there is still a significant difference between both. We should definitely acknowledge that we assumed different back contact materials. This results from the fact that our FDTD implementation could not handle real-world metals and rather approximated them by

Parameter		Value
General setup		
Incident spectrum		AM1.5g
Bulk material		c-Si
Length	L	1 µm
Wavelength minimum	λ_{min}	300 nm
Wavelength maximum	λ_{max}	1199 nm
Lambert-Beer		
Rear material		Ag
Spectral step width	$\Delta\lambda$	0.5, 1 nm
Spectral nodes	N	1000
Positional nodes	M	1000
FDTD		
Rear material		perfect electric conductor
Spectral nodes	N	100
Positional nodes	M	500

Table 8.: Simulations were run by the Lambert-Beer model, and by the Yee implementation (“FDTD”). Parameters for the general setup as well as for each simulation are given here.

perfect electric conductors, i.e. their conductivity σ is infinite. The definite reasons for the difference were not clear to our group and further analysis is still needed.

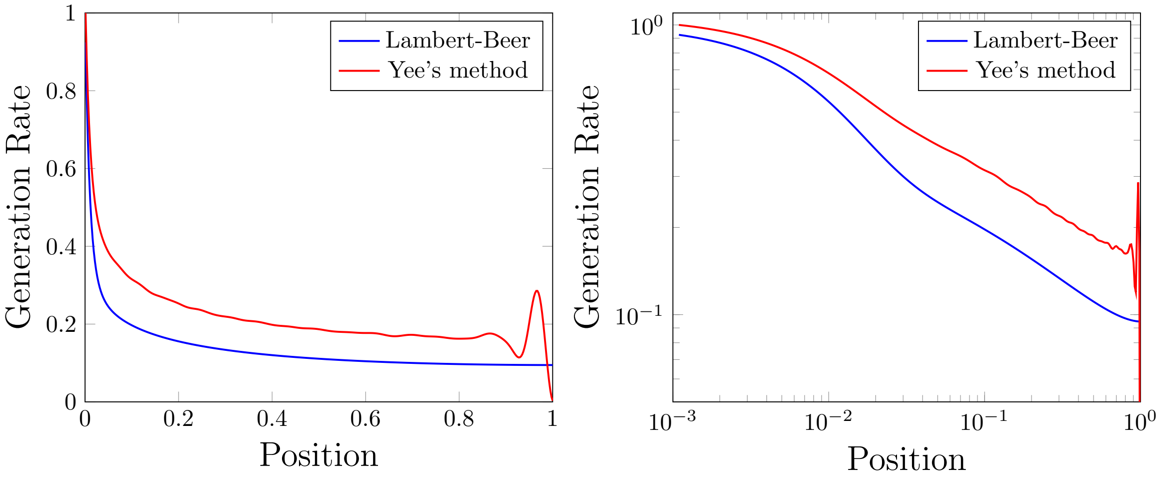

Figure 15.: Generation rates obtained from a Lambert-Beer, and Yee's method simulation are shown. The simulation setups are described in Table 8. The generation rates were scaled by the maximum of both data sets, and the position is also normalized. The left image shows both data sets on linear scales, and the right within a double logarithmic plot.

3. Charge Transport in Semiconductors

3.1. State of the art

Electrical charge transport within semiconductors can be modeled by the drift-diffusion equations. First simulations were done by Scharfetter et al. in 1967 [12]. Their purpose was to determine radiation's effect upon performance for outer space applications. In 1976 conventional silicon solar cells had efficiencies of around 11.8%. Simulations by Fossum helped to reveal cell design criteria and necessary material parameter refinements to possibly increase efficiencies above 20% [10]. Two-dimensional modeling became available in 1982 as Gray published his application SCAP2D [11]. The applications so far have all been using finite difference discretization schemes whereas the first finite element method program PC1D was available in 1985 [39]. It has been widely adopted in the photovoltaic industry and turned open-source in mid 1990's. Up to today, it is still the most widely used simulation program in the photovoltaics community despite being just one-dimensional and using out-dated models [38].
Today simulations are used on a broader field but often with specialized goals. For full device modeling the most widely used tools in the industry are Synopsys' Sentaurus™ [44], Silvaco's Atlas™ [41], and COMSOL Multiphysics® [3]. For specialized simulations resulting from specific tasks many researchers develop their own applications (e.g., Deceglie for nanophotonic light-trapping [4], exciton flow in organic solar cells [45]).

Apart from these general purpose device modeling applications there are programs especially written for solar cells. The Helmholtz-Zentrum Berlin has published a feature-rich Windows gui-tool AFORS-HET [47]. It can run numerical simulations for various input spectra and do advanced electrical transport simulations within heterostructures. The problem is that lots of numerical schemes are not fully documented such that the user does not know which numerical method is being used.

3.2. Semiconductors

3.2.1. Physical understanding

Solid matter can roughly be grouped into 3 categories: *metals, insulators, and semiconductors.* Their electric conductivity behavior is used for classification and Figure 16 shows a sketch of the general temperature dependence. The overall trend is that metals have a very high conductivity, insulators a negligible, and semiconductors a conductivity strongly increasing with temperature. A simple explanation for this behavior is given in solid-state physics in terms of their band structure. To understand the concept of band structures one should look at the simple test case of a single hydrogen atom. By quantum mechanical calculations one can show that the energy eigenstates are discrete. When grouping multiple hydrogen atoms together into a periodic potential one does not get discrete energy eigenstates anymore nor a complete spectrum but rather disjoint intervals of allowed and forbidden energy levels. These intervals are called the solid's *band structure.*

The general characterization by solid-state physics is given in terms of the highest filled energy state. The energy states are filled from the bottom to the top and for metals the highest state is right within a partially filled band. For insulators and semiconductors the band ("valence band") is fully filled and there is a gap to the next band. This *band gap* is a forbidden region without any possible electron states. Insulators and semiconductors differ in their size of the forbidden region between the filled valence band and the first empty one – called *conduction band.* Typically for band gaps smaller than 4 eV one thinks of semiconductors and for larger values of insulators [49]. Figure 17 shows the different schemes of band structures.

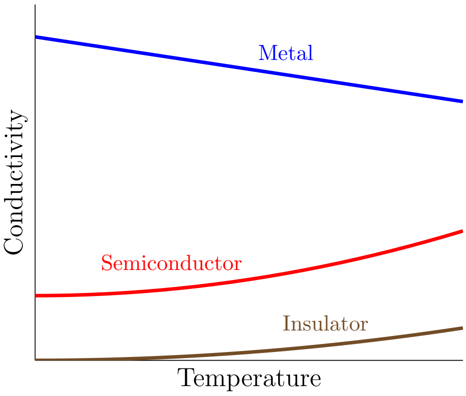

Figure 16.: A schematic sketch of the conductivity's temperature dependence for metals, insulators, and semiconductors.

The band picture holds only in an averaged sense that the electrons distribution among the energy states is given in this kind of band structure. By quantum mechanics, electrons actually follow the *Fermi distribution* $f(E,T)$ for energy E at temperature T with respect to the Fermi level[1] E_F [14, p. 144]

$$f(E,T) := \left(\exp\left(\frac{E-E_F}{k_BT}\right)+1\right)^{-1} = \left(\exp\left(\frac{\frac{E}{E_F}-1}{\frac{k_BT}{E_F}}\right)+1\right)^{-1}. \tag{3.1}$$

Figure 18 shows the Fermi distribution for different temperatures and one can clearly see that the distribution smears out for increasing temperatures. From this follows that electrons at the top of the valence band have a non-vanishing probability to have an energy which is larger than the bottom of the conduction band such that the electrons will get pushed above the band gap. This process is called *thermal excitation* and depicted within Figure 19.

The thermal excitation of electrons is the reason why semiconductors can conduct electricity better at higher temperatures. The resulting electron density in the conduction

---

[1] The Fermi level E_F describes the energy needed to add one electron to the system, and at thermodynamic equilibrium it represents a hypothetical energy level with 50% probability of being occupied.

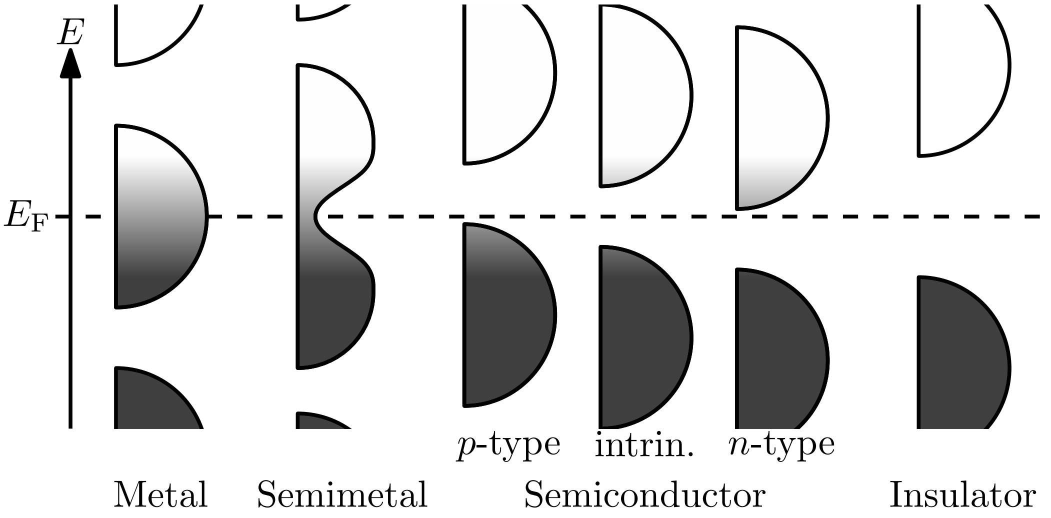

Figure 17.: A schematic plot of energy bands for different materials is shown. The energy bands have two characteristics: their shading, and horizontal dimension. The shading denotes the density of states which is the number of filled electron states at a given energy. Its scale goes from unfilled (white) up to filled (black). The horizontal dimension depicts the total number of electron states for a given energy level which explicitly includes filled as well as unfilled states. The dashed line denotes the Fermi level E_{F}.

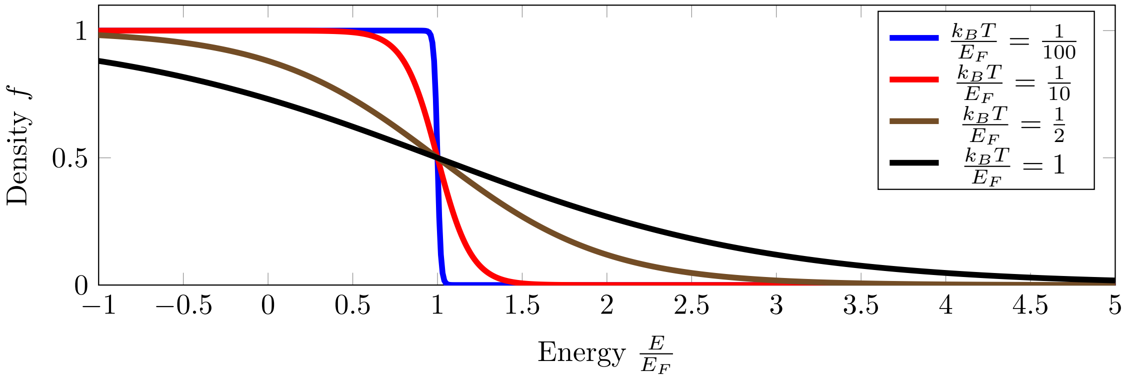

Figure 18.: The Fermi distribution f given by equation (3.1) is shown. Its dependence on the ratio of temperature T, and Fermi level E_F is clearly visible.

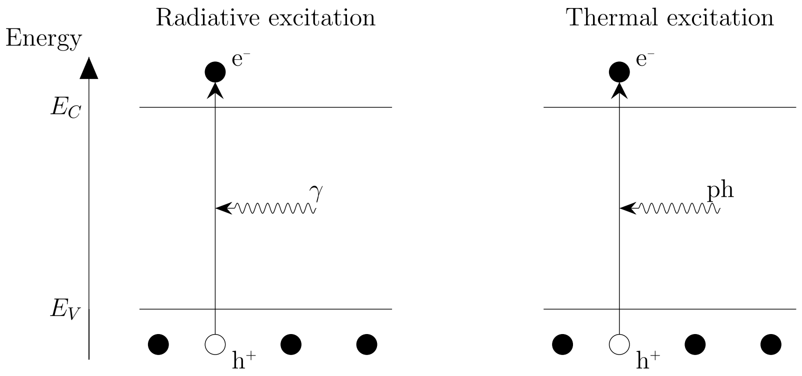

Figure 19.: Possible excitation processes within a solar cell are shown. An electron (e⁻) is excited from within the valence band into the conduction band and thus, creating a hole (h^+) in the valence band. The conduction band is denoted by its minimal energy E_C, and the valence band by its maximal energy E_V. In radiative excitation the process is triggered by an incoming photon (γ) whereas lattice vibrations ($\underline{\text{ph}}$onons) trigger thermal excitations.

band is called the *intrinsic carrier concentration* n_i which depends on the specific material and strongly on temperature. For silicon Misiakos et al. [23] have published a model which approximates experimental data on the range from 78 K up to 340 K with no more than 5% error. Their model is given by

$$n_i(T) = 5.29 \cdot 10^{19} \left(\frac{T}{300\,\mathrm{K}} \right)^{2.54} \exp\left(-\frac{6726\,\mathrm{K}}{T} \right) \frac{1}{\mathrm{cm}^3},$$

with a value at room temperature of $n_i(300\,\mathrm{K}) = (9.7 \pm 0.1) \times 10^9 \frac{1}{\mathrm{cm}^3}$.
Apart from the thermal excitation process there exists *radiative excitation* where electrons get pushed above the energy gap by absorbing energy from incoming photons. The absorption process is shown in Figure 19. To calculate this one needs detailed input of the optical processes which is usually done via numerical simulations, see Section 2.2.
Every excitation process is treated as increasing the occupation number of electrons within the conduction band and decreasing the valence band's number. Thus there is one electron missing inside the valence band – interpreted as a *hole* – which acts as another free but positive charge. Electrons in the conduction band and holes in the valence band are treated as charge carriers which can freely move around.
The electrons in the conduction band are in a meta-stable state and by a non-vanishing probability the electron will relax back down into the valence band. This motion can be interpreted as an annihilation of the electron with a hole, thus a process called *recombination*. There are three major types of recombination: radiative, Shockley-Read-Hall, and Auger. General sketches are shown in Figure 20.
Radiative recombination is in principle a reversed absorption process in which an electron from the conduction band, and a hole are annihilated and the energy difference

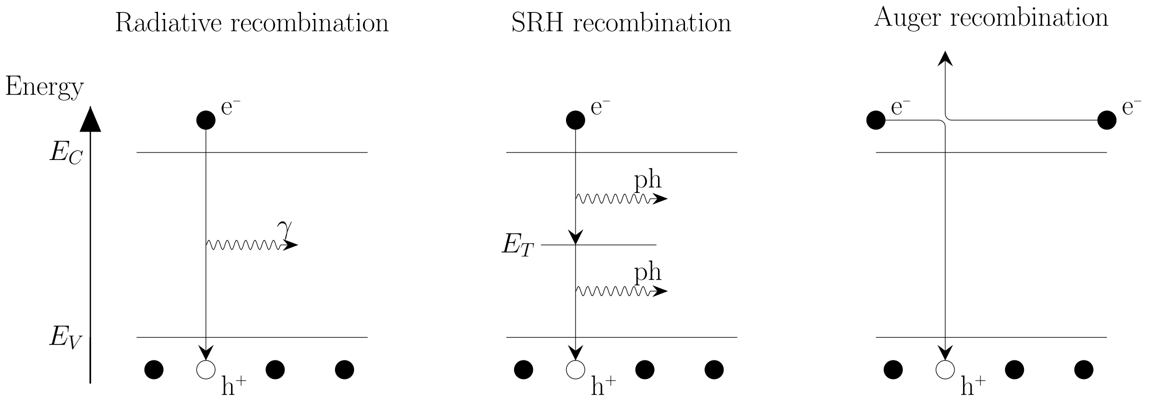

Figure 20.: Possible recombination processes within a solar cell are shown. Electrons (e⁻) in the conduction band are in a meta-stable state and recombination with holes (h^+) from the valence band are possible. The conduction band is denoted by its minimal energy E_C, and the valence band by its maximal energy E_V. Radiative recombination is a reverse radiative excitation process. Shockley-Read-Hall (SRH) recombination uses defect states of energy E_T within the band gap to mediate the recombination. Auger recombination is a three particle interaction process. A high energy hole or electron recombines and the excess energy is given off to another electron or hole. Only the electron-hole-electron interaction is sketched here.

is given off directly in form of photons. This process dominates the recombination in direct band gap semiconductors[2] such as gallium arsenide.
Another recombination process is possible if the periodic structure of the semiconductor's lattice is broken. These asymmetries are called *lattice impurities*. The impurities create new energy states in the forbidden region which help conduction electrons to move down into the valence band using energetically smaller steps. As the energy differences of each step are smaller, it is easier to exchange the energy with phonons (interaction with the lattice vibrations) or photons. This process is known as *Shockley-Read-Hall recombination*.
The third process, *Auger recombination*, is the reversed impact ionization. Here the conduction electron, and hole annihilate and the freed energy is absorbed by a third carrier. The third carrier's excitation energy is subsequently dissipated by generating new phonons.

The equilibrium concentration of carriers within the semiconductor can be altered by a process called *doping*. Herein one substitutes single atoms in the crystal lattice with atoms of a different element. Substituting it with an element of a higher group[3] will

---

[2] Electron states at the top of the valence band, and bottom of the conduction band are characterized by a specific crystal momentum out of the first Brillouin zone. In case they are the same the material is of *direct band gap* type, otherwise *indirect band gap* type. An important implication is that in a direct band gap semiconductor an electron can directly emit photons whereas in indirect ones they need to interact with traps, or phonons first.

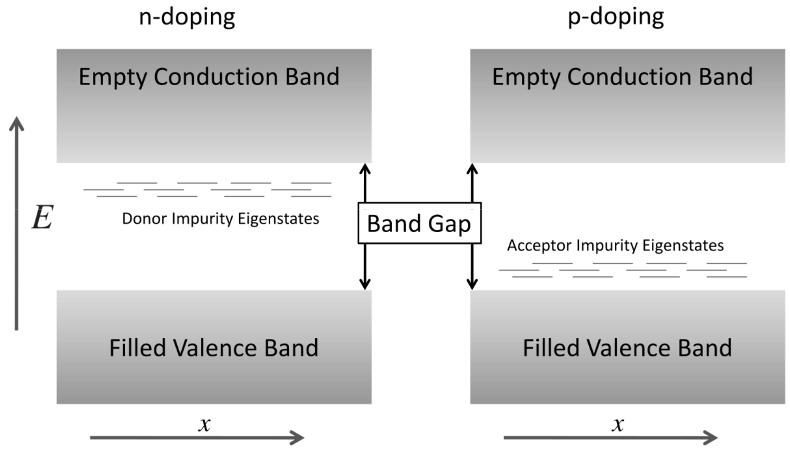

Figure 21.: The doping process adds intermediate energy states into the forbidden region. For n-type doped materials one uses elements that have one more electron than the lattice's element. Thus, it adds easily one electron to the conduction band and the newly introduced energy states are close to the conduction band's edge. For p-type doping it works the opposite way. Graphic taken from [42].

directly lead to more electrons in the conduction band. Vice-versa with less electrons it adds more holes to the semiconductor. The substituted elements are called *donor* atoms, and respectively *acceptor* atoms. Donor and acceptor atoms can be interpreted as creating energy states within the forbidden region which ease the process of jumping the band gap, see Figure 21.

Usually one dopes single regions only with donors or acceptors which results into a so-called *n-type* or *p-type* semiconductor. In n-type region there is an excess of electrons which are then called the *majority carriers* and *minority carriers* for holes. The naming scheme is reversed in a p-type region. The *Law of Mass Action* states that at equilibrium the product of electron density n_0 and hole density p_0 is a constant

$$n_0 \cdot p_0 = n_i^2 = \text{const}\,.$$

As the doping densities usually exceeds the intrinsic density by several orders of magnitude one can approximate the majority density by the doping density. Therefore, let N_D be the donor density, and respectively N_A the acceptor density, which leads to the following results for either n- or p-type regions

$$\begin{aligned} n\text{-type:} \quad & n_0 \approx N_D \quad \Longrightarrow \quad p_0 \approx \frac{n_i^2}{N_D} \\ p\text{-type:} \quad & p_0 \approx N_A \quad \Longrightarrow \quad n_0 \approx \frac{n_i^2}{N_A}\,. \end{aligned}$$

---

[3] Element groups refer to the columns of the periodic table of elements. Groups represent elements which have the same amount of electrons in their outer most shell and thus, similar properties.

For comparison purposes, in crystalline silicon the atom density is about $5 \times 10^{22} \, \frac{1}{\mathrm{cm}^3}$ and doping concentration might be in the range of $10^{13} \, \frac{1}{\mathrm{cm}^3}$ to $10^{18} \, \frac{1}{\mathrm{cm}^3}$. For doping concentrations above $10^{18} \, \frac{1}{\mathrm{cm}^3}$ one calls it *degenerately doped* and is usually abbreviated with being a "n+" or "p+" region.

3.2.2. Unipolar semiconductor model

Macrophysical models for semiconductors can be derived from a basic approach by treating the local charges via smeared out density distributions. The averages of these densities will lead to macrophysical equation systems which one can readily solve by numerical means.

In a first approximation we will only look at the electron charges and neglect holes – thus the *unipolar model*. This simplifies the notation by a great deal and the extensions towards an electron-hole model are straight-forward calculations of similar type. We will derive the drift-diffusion equations from the Boltzmann equation via a perturbation expansion called *Hilbert expansion*. It is mathematically rigorous and does not depend on physical intuitions as compared to the usual *moment method*. Furthermore, we will be doing the following approximations in detail

- diffusion scaling of the Boltzmann transport equation,
- low density approximation of the collision operator,
- parabolic band approximation,
- electrostatic approximation of an isotropically medium.

3.2.2.1. Semiconductor Boltzmann equation

From physical reasoning we know that semiconductors contain large numbers of electrons in their conduction band, see Section 3.2.1. Thus, we employ a statistical approach of treating electrons via a continuous density $n = n(\mathbf{x}, t)$ and its distribution $f = f(\mathbf{x}, \mathbf{k}, t)$ for position $\mathbf{x}$, time t, and momentum $\mathbf{k}$ [17, p. 46]

$$n(\mathbf{x}, t) = \int_{B_1} f(\mathbf{x}, \mathbf{k}, t) \frac{\mathrm{d}\mathbf{k}}{4\pi^3} \,, \tag{3.2}$$

where the integration is taken over the *first Brillouin zone*[4] B_1.

Now, f changes along a trajectory $\Gamma = \Big\{ \big(\mathbf{x}(t), \mathbf{k}(t) \big) \Big\}$ due to convective, and electric effects given by $\frac{\mathrm{d}f}{\mathrm{d}t}\Big|_{\Gamma}$. But we assume that its change balances the change due to collisions of particles – given by the operator $Q = Q[f]$,

$$Q[f] \overset{!}{=} \frac{\mathrm{d}f}{\mathrm{d}t} = \partial_t f + \dot{\mathbf{x}} \cdot \boldsymbol{\nabla}_{\mathbf{x}} f + \dot{\mathbf{k}} \cdot \boldsymbol{\nabla}_{\mathbf{k}} f \,.$$

---

[4] Semiconductors are treated as solids with arrays of atoms arranged within a periodic lattice. The momenta need to be periodic as well and one often looks at a specific unit cell – the *first Brillouin zone* [17, p. 4].

For band energy $\epsilon = \epsilon(\mathbf{k})$, and electrostatical potential $V = V(\mathbf{x}, t)$ one can state the semi-classical equations of motion for electrons in a semiconductor as [17, p. 21]

$$\hbar\mathbf{v} := \hbar\dot{\mathbf{x}} = \boldsymbol{\nabla}_{\mathbf{k}}\epsilon, \quad \hbar\dot{\mathbf{k}} = e\boldsymbol{\nabla}_{\mathbf{x}}V =: -e\mathbf{E}\,.$$

Together one gets the *semiconductor Boltzmann equation*, which is usually stated along with initial data f_{init}

$$\begin{gathered}\partial_t f + \frac{1}{\hbar}\boldsymbol{\nabla}_{\mathbf{k}}\epsilon \cdot \boldsymbol{\nabla}_{\mathbf{x}} f - \frac{e}{\hbar}\mathbf{E}\cdot\boldsymbol{\nabla}_{\mathbf{k}} f = Q[f] \\ \text{for} \quad \mathbf{x} \in \Omega \subset \mathbb{R}^3,\ t > 0,\ \mathbf{k} \in B_1 \subset \mathbb{R}^3 \\ \text{with} \quad f(\,\cdot\,,\,\cdot\,,0) = f_{\text{init}}\,.\end{gathered} \tag{3.3}$$

The position $\mathbf{x}$ belongs to the set Ω which represents the device's geometry.

3.2.2.2. Knudsen number

To derive macroscopic equations one looks at asymptotic behavior of the general Boltzmann equation (3.3). It can be scaled differently depending on the desired limiting test case. For the transformation via scaling we need to introduce the following scaling constants (usually denoted with a “hat” symbol) and scaled variables or functions (subscript “s”) [17, p. 47]

$$\begin{aligned}
\mathbf{x} &= \lambda\mathbf{x}_s\,, & & \\
\mathbf{v} &= \hat{v}\mathbf{v}_s\,, & \hat{v} &= \sqrt{\frac{k_B T}{m^*}}\,, \\
\mathbf{k} &= \hat{k}\mathbf{k}_s\,, & \hat{k} &= \frac{m^*\hat{v}}{\hbar}\,, \\
V &= U_T V_s\,, & U_T &= \frac{k_B T}{e}\,, \\
t &= \tau t_s\,, & & \\
\epsilon &= \hat{\epsilon}\epsilon_s\,, & \hat{\epsilon} &= k_B T\,, \\
\lambda_C &= \hat{v}\tau_C\,, & & \\
\mathbf{E} &= \hat{E}\mathbf{E}_s\,, & \hat{E} &= \frac{U_T}{\lambda}\,, \\
f(\mathbf{x},\mathbf{k},t) &= f_s(\mathbf{x}_s,\mathbf{k}_s,t_s)\,, & & \\
Q[f] &= \frac{1}{\tau_C}Q_s[f]\,. & &
\end{aligned}$$

Here the positional scaling constant λ represents a characteristic length scale (e.g., device's length), m^* is given by the effective electron mass, τ is a time which will be set later on, and τ_C is the average time between two consecutive collisions. The average collision time τ_C together with the average velocity $\hat{v}$ define the average distance between two collisions, the so-called *mean free path* λ_C.

We assume that the transport is dominated by scattering processes such that the distance between two consecutive collisions is much smaller than the characteristic device's length scale. This gives rise to the definition of the *Knudsen number* $Kn = \alpha := \frac{\lambda_C}{\lambda} \ll 1$ which is just the scaled mean free path. The Knudsen number will be used as a scaling constant for the general Boltzmann equation (3.3).
Concerning the time scaling constant τ there are two standard approaches. The *hydrodynamical scaling* sets τ equal to $\frac{\tau_C}{\alpha}$ and the *diffusion scaling* is given by $\tau = \frac{\tau_C}{\alpha^2}$. The specific scaling to choose depends on the equilibrium states associated with the collision operator [17, p. 47].

3.2.2.3. Diffusion scaling

The scaling constants and functions introduced in the previous section together with the diffusion scaling plugged into equation (3.3) lead to the *(diffusion) scaled semiconductor Boltzmann equation* [17, p. 47]

$$\begin{aligned}
&\left(\frac{1}{\tau}\partial_{t_s} f_s\right) + \frac{1}{\hbar}\left(\frac{\hat{\epsilon}}{\hat{k}}\boldsymbol{\nabla}_{\mathbf{k}_s}\epsilon_s\right)\cdot\left(\frac{1}{\lambda}\boldsymbol{\nabla}_{\mathbf{x}_s} f_s\right) - \frac{e}{\hbar}\left(\hat{E}\mathbf{E}_s\right)\cdot\left(\frac{1}{\hat{k}}\boldsymbol{\nabla}_{\mathbf{k}_s} f_s\right) = \frac{1}{\tau_C}Q_s[f_s] \\
\iff \quad & \alpha^2\partial_{t_s} f_s + \left(\frac{\hat{v}\tau_C\alpha^2}{\lambda}\right)\boldsymbol{\nabla}_{\mathbf{k}_s}\epsilon_s\cdot\boldsymbol{\nabla}_{\mathbf{x}_s} f_s - \left(\frac{e\hat{E}\tau_C\alpha^2}{\hbar\hat{k}}\right)\mathbf{E}_s\cdot\boldsymbol{\nabla}_{\mathbf{k}_s} f_s = Q_s[f_s] \\
\iff \quad & \alpha^2\partial_{t_s} f_s + \alpha(\boldsymbol{\nabla}_{\mathbf{k}_s}\epsilon_s\cdot\boldsymbol{\nabla}_{\mathbf{x}_s} f_s - \mathbf{E}_s\cdot\boldsymbol{\nabla}_{\mathbf{k}_s} f_s) = Q_s[f_s] \qquad (3.4) \\
& \text{for} \quad \mathbf{x}_s \in \Omega_s \subset \mathbb{R}^3,\ t_s > 0,\ \mathbf{k}_s \in B_s \subset \mathbb{R}^3 \\
& \text{with} \quad f_s(\,\cdot\,,\,\cdot\,,0) = f_{\text{init},s}\,,
\end{aligned}$$

with the straightforward scalings of Ω_s, B_s, $f_{\text{init},s}$.

3.2.2.4. Low density approximation for the collision operator

The *low density approximation* is important for many semiconductor devices as the value of the density distribution f is under most circumstances quite small

$$0 \le f(\mathbf{x},\mathbf{k},t) \ll 1\,.$$

The usual *collision integral term* $Q[f]$ of the semi-classical Boltzmann equation is given by [17, p. 47]

$$Q[f](\mathbf{x},\mathbf{k},t) = \int_{B_1} S(\mathbf{x},\mathbf{k}',\mathbf{k})f'(1-f) - S(\mathbf{x},\mathbf{k},\mathbf{k}')f(1-f')\,\mathrm{d}\mathbf{k}' \qquad (3.5)$$

$$\text{with abbr.:} \quad f = f(\mathbf{x},\mathbf{k},t),\ f' = f(\mathbf{x},\mathbf{k}',t)\,, \qquad (3.6)$$

where $S(\mathbf{x},\mathbf{k}',\mathbf{k})$ is the transition probability between the states $(\mathbf{x},\mathbf{k})$ and $(\mathbf{x},\mathbf{k}')$. For the low density approximation the quadratic terms in f are ignored which yields the *low density collision integral term* $Q_L[f]$ [22, p. 33],

$$Q_L[f](\mathbf{x},\mathbf{k},t) = \int_{B_1} S(\mathbf{x},\mathbf{k}',\mathbf{k})f' - S(\mathbf{x},\mathbf{k},\mathbf{k}')f\,\mathrm{d}\mathbf{k}'\,.$$

By physical reasoning collisions should not alter the total particle number at any given point and time. Thus, a collision operator is called *conservative* if and only if its integral over $\mathbf{k}$-space vanishes. One can readily check – by using the scattering rate's symmetric nature in $\mathbf{k}, \mathbf{k}'$ – that Q_L is truly a *conservative collision operator*, i.e.

$$\langle Q[f] \rangle = \int_{B_1} Q_L[f](\mathbf{x}, \mathbf{k}, t) \, \mathrm{d}\mathbf{k} = 0 \, . \tag{3.7}$$

In the low density approximation one uses a *Maxwellian* distribution M as approximation for the thermal *equilibrium* distribution f_{eq} [22, p. 33]. This is commonly done for Fermi-Dirac distributions in the limit of high temperature and low particle density

$$f_{\mathrm{eq}}(\mathbf{x}, \mathbf{k}, t) = M(\mathbf{k}) \, ,$$
$$\text{with} \quad M(\mathbf{k}) := C \exp\left(-\frac{\epsilon(\mathbf{k})}{k_B T}\right), \quad C := \left(\int_{B_1} \exp\left(-\frac{\epsilon(\mathbf{k})}{k_B T}\right) \mathrm{d}\mathbf{k}\right)^{-1} \, ,$$

where $\epsilon(\mathbf{k})$ represents the state's energy.

Starting off with the so-called *principle of detailed balance* which asserts that the local scattering probability vanishes for all states $(\mathbf{x}, \mathbf{k})$, $(\mathbf{x}, \mathbf{k}')$ in thermal equilibrium. Thus in the low density approximation this yields [22, p. 33]

$$\begin{aligned} S(\mathbf{x}, \mathbf{k}', \mathbf{k}) f'_{\mathrm{eq}} &= S(\mathbf{x}, \mathbf{k}, \mathbf{k}') f_{\mathrm{eq}} \\ \implies \quad S(\mathbf{x}, \mathbf{k}', \mathbf{k}) M(\mathbf{k}') &= S(\mathbf{x}, \mathbf{k}, \mathbf{k}') M(\mathbf{k}) \, . \end{aligned} \tag{3.8}$$

After realizing that the Maxwellian does not vanish for any wave vector $\mathbf{k}$ one can do the general ansatz [22, p. 34]

$$S(\mathbf{x}, \mathbf{k}, \mathbf{k}') = \phi(\mathbf{x}, \mathbf{k}, \mathbf{k}') M(\mathbf{k}') \, . \tag{3.9}$$

Plugging equation (3.9) into equation (3.8) yields a condition on ϕ: it should be symmetric in $\mathbf{k}, \mathbf{k}'$. This function ϕ is the called *collision cross-section.*

Using equation (3.9), and the symmetry property of ϕ gives the final form for the low density collision term

$$Q_L[f](\mathbf{x}, \mathbf{k}, t) = \int_{\mathbb{R}^3} \phi(\mathbf{x}, \mathbf{k}, \mathbf{k}') \big[M(\mathbf{k}) f(\mathbf{x}, \mathbf{k}', t) - M(\mathbf{k}') f(\mathbf{x}, \mathbf{k}, t) \big] \, \mathrm{d}\mathbf{k}' \, . \tag{3.10}$$

It is important to note that the integration domain has been extended to the whole space which is commonly done and convenient for further computations [17, p. 34].

3.2.2.5. Parabolic band approximation

Another approximation is needed – the *parabolic band approximation.* Therein, one assumes that the conduction electrons' energies ϵ are close to the conduction band minimum E_C [22, p. 85] ,

$$\epsilon(\mathbf{k}) = E_C + \frac{\hbar^2}{2m^*} |\mathbf{k}|^2 \, .$$

With the energy scaling introduced in Section 3.2.2.2 this reads as follows

$$\epsilon_s(\mathbf{k}_s) = \frac{\epsilon(\hat{k}\mathbf{k}_s)}{\hat{\epsilon}} = E_{C,s} + \frac{1}{2}|\mathbf{k}_s|^2 \quad \text{with} \quad E_{C,s} := \frac{E_C}{\hat{\epsilon}}\,.$$

3.2.2.6. Hilbert expansion

The *Hilbert expansion* is an expansion of solutions of the Boltzmann equation (3.4). The distribution f is expanded in powers of the Knudsen number α [22, p. 87],

$$f = f_0 + \alpha f_1 + \alpha^2 f_2 + \mathcal{O}\left(\alpha^3\right).$$

Substituting this expansion into the Boltzmann equation (3.4) and solving for different powers of α will yield a new equation system.
The leading order term results from comparing the coefficients of α^0,

$$0 = Q_L[f_0]\,.$$

Now, f_0 is within the kernel of the collision operator. Jüngel [17, p. 82] has shown that for a cross section $\phi = \phi(\mathbf{x}, \mathbf{k}, \mathbf{k}')$ which is positive, and symmetric in $\mathbf{k}, \mathbf{k}'$ the kernel is spanned by Maxwellians. Thus, we know the leading order term of the solution is given by

$$f_0(\mathbf{x}, \mathbf{k}, t) = \tilde{n}(\mathbf{x}, t) M(\mathbf{k})\,,$$
$$M(\mathbf{k}) = C \exp\left(-\frac{|\mathbf{k}|^2}{2}\right), \quad C = \left[\int_{\mathbb{R}^3} \exp\left(-\frac{|\mathbf{k}|^2}{2}\right) \frac{\mathrm{d}\mathbf{k}}{4\pi^3}\right]^{-1} = \left(2\pi^3\right)^{-1/2}.$$

Here the constant C was chosen such that the unspecified function $\tilde{n}$ represents the scaled electron density n_s.

The next order of coefficient α^1 leads to

$$\begin{aligned} Q[f_1] &= \nabla_{\mathbf{k}}\epsilon \cdot \nabla_{\mathbf{x}} f_0 - \mathbf{E} \cdot \nabla_{\mathbf{k}} f_0 \\ &= M\mathbf{k} \cdot (\nabla_{\mathbf{x}} n + n\mathbf{E})\,, \end{aligned} \tag{3.11}$$

where the identities $\nabla_{\mathbf{k}}\epsilon = \mathbf{k}$, and $\nabla_{\mathbf{k}} f_0 = -nM\mathbf{k}$ are used which have been derived from the parabolic band approximation.
A technical proposition by Jüngel [17, p. 101] states that solutions $h_i = h_i(\mathbf{k})$ of

$$Q[h_i] = M(\mathbf{k})k_i\,, \quad i = 1, 2, 3\,, \tag{3.12}$$

exist and uniqueness is guaranteed for functions satisfying $\langle h_i S\rangle = 0$ where we introduced the integral over $\mathbf{k}$-space – denoted by $\langle\,\cdot\,\rangle$. Since equation (3.11) is a linear combination of (3.12) with coefficients independent of $\mathbf{k}$ and by using the linearity of Q one can argue that the solution f_1 is uniquely given by

$$f_1 = \mathbf{h} \cdot (\nabla_{\mathbf{x}} n + n\mathbf{E})\,. \tag{3.13}$$

We need another propositions by Jüngel [17, p. 103] which assumes some technical assumptions about the collision cross section ϕ, i.e. regularity assumptions, and invariance w.r.t. isometric operations. Then there exists a non-negative function $\mu_0(\mathbf{x}) \geq 0$, such that for solutions h_i of equation (3.12) the following holds

$$\int_{\mathbb{R}^3} \mathbf{k} \otimes \mathbf{h} \frac{\mathrm{d}\mathbf{k}}{4\pi^3} = -\mu_0(\mathbf{x}) I_3 \,, \tag{3.14}$$

where $\mathbf{k} \otimes \mathbf{h}$ denotes a (3×3)-matrix with entries $(\mathbf{k} \otimes \mathbf{h})_{i,j} = k_i h_j$.
The first moment of f_1 leads to the definition of the *current density* $\mathbf{J}$ where we make use of equation (3.14)

$$\begin{aligned} \mathbf{J} &:= -\left\langle \mathbf{k} f_1 \right\rangle \\ &= -\left\langle \mathbf{k}\left(\mathbf{h} \cdot (\boldsymbol{\nabla}_{\mathbf{x}} n + n\mathbf{E})\right)\right\rangle \\ &= -\left\langle \mathbf{k} \otimes \mathbf{h} \right\rangle \cdot (\boldsymbol{\nabla}_{\mathbf{x}} n + n\mathbf{E}) \\ &= \mu_0 (\boldsymbol{\nabla}_{\mathbf{x}} n + n\mathbf{E}) \,. \end{aligned} \tag{3.15}$$

Finally, collecting coefficients of the order α^2 gives

$$\partial_t f_0 + \mathbf{v} \cdot \boldsymbol{\nabla}_{\mathbf{x}} f_1 - \mathbf{E} \cdot \boldsymbol{\nabla}_{\mathbf{k}} f_1 = Q[f_2] \,. \tag{3.16}$$

Taking the integral over $\mathbf{k}$-space of equation (3.16), using the statements above, and the conservative property (3.7) of Q yields

$$\begin{aligned} \left\langle Q[f_2] \right\rangle = \partial_t \left\langle f_0 \right\rangle + \boldsymbol{\nabla}_{\mathbf{x}} \cdot \left\langle \mathbf{v} f_1 \right\rangle - \mathbf{E} \cdot \left\langle \boldsymbol{\nabla}_{\mathbf{k}} f_1 \right\rangle &= 0 \\ \iff \quad \partial_t n - \boldsymbol{\nabla}_{\mathbf{x}} \cdot \mathbf{J} &= 0 \,. \end{aligned} \tag{3.17}$$

Equation (3.17) is a conservation law for the density n. The current density $\mathbf{J}$ is compromised of the *diffusion current* $\mu_0 \boldsymbol{\nabla}_{\mathbf{x}} n$, and the *drift current* $\mu_0 n \mathbf{E}$ where μ_0 is called the (scaled) *electron mobility*. Equation (3.17) makes up the so-called *drift diffusion model.*

3.2.2.7. Poisson's equation

So far, the electric field $\mathbf{E} = \mathbf{E}(\mathbf{x}, t)$ in equation (3.15) has been treated constant which is not accurate. It stems not only from external contributions but rather from internal charge distributions. The charge distribution $\rho = \rho(\mathbf{x}, t)$ is given by the electron density, and doping contributions $C = C(\mathbf{x})$ resulting from donors as well as acceptors $N_D = N_D(\mathbf{x}), N_A = N_A(\mathbf{x})$

$$\rho(\mathbf{x}, t) = e\big(-n(\mathbf{x}, t) + C(\mathbf{x})\big) \,, \quad C(\mathbf{x}) = N_D(\mathbf{x}) - N_A(\mathbf{x}) \,.$$

This charge distribution induces the electric field $\mathbf{E}$ by Gauss's law (one of Maxwell's equations)

$$\boldsymbol{\nabla} \cdot \big(\bar{\bar{\epsilon}} \mathbf{E}\big) = \rho \,,$$

where the dielectric tensor $\bar{\bar{\epsilon}}$ has been introduced. For isotropically materials one can approximate this tensor by a constant ϵ.
Furthermore, in the *electrostatic approximation* of slowly changing magnetic fields, and electric currents one can express the electric field by a scalar potential $V = V(\mathbf{x})$

$$\begin{aligned} & \mathbf{E} = -\boldsymbol{\nabla} V \\ \Longrightarrow \quad & \nabla^2 V = -\frac{\rho}{\epsilon} \,. \end{aligned} \tag{3.18}$$

Equation (3.18) is called the (electrostatic) *Poisson's equation.*
Its non-dimensionalization is done by scaling introduced in Section 3.2.2.2 together with a possible density scaling

$$\begin{aligned} n(\mathbf{x}, t) &= n(\lambda \mathbf{x}_s, \tau t_s) =: \hat{C} n_s(\mathbf{x}_s, t_s) \\ C(\mathbf{x}) &= C(\lambda \mathbf{x}_s) =: \hat{C} C_s(\mathbf{x}_s) \,, \\ \text{with} \qquad & \hat{C} := \max_{\mathbf{x}\in\Omega} \big| C(\mathbf{x}) \big| \;. \end{aligned}$$

Poisson's equation (3.18) is given in its scaled form as

$$\begin{aligned} & \nabla^2_{\mathbf{x}} V = -\frac{\rho}{\epsilon} \\ \Longleftrightarrow \qquad & \frac{1}{\lambda^2} \nabla^2_{\mathbf{x}_s} (U_T V_s) = -\frac{e\hat{C}}{\epsilon} (C_s - n_s) \\ \Longleftrightarrow \qquad & \lambda_D^2 \nabla^2_{\mathbf{x}_s} V_s = (n_s - C_s) \,, \end{aligned} \tag{3.19}$$

where the (scaled) *Debye length* $\lambda_D := \sqrt{\frac{U_T \epsilon}{\lambda^2 e \hat{C}}}$ has been introduced.

3.2.2.8. Semiconductor equations

Equations (3.15), (3.17), and (3.19) make up the (scaled) *semiconductor equations* in low-density, and small field approximation

$$\begin{aligned} \partial_t n - \boldsymbol{\nabla} \cdot \mathbf{J} = 0 \,, \quad & \mathbf{J} = \mu_0 (\boldsymbol{\nabla} n - n \boldsymbol{\nabla} V) \\ \lambda_D^2 \nabla^2 V = n - C \,, & \end{aligned}$$

where the gradient $\boldsymbol{\nabla}$ is w.r.t. position $\mathbf{x}$. The independent variables are given by time t, and position $\mathbf{x}$. The dependent variables one wants to solve for are the electron density $n = n(\mathbf{x}, t)$, and electrostatic potential $V = V(\mathbf{x}, t)$. The external parameters, and constants are the doping density $C = C(\mathbf{x})$, the Debye length $\lambda_D = \text{const}$, and the electron mobility $\mu_0 = \mu_0(\mathbf{x})$.
Furthermore, one should note that for notational convenience the scaling index "s" on each term has been omitted.

3.2.2.9. Mobility

To numerically solve the drift-diffusion model one needs accurate models for the material parameters. The charge mobility μ is one important material parameter which has non-linear dependencies.

The charge's mobility is limited by interaction processes. The most commonly used effects are the interaction with thermally generated lattice vibrations (phonons), ionized impurities, and carrier-carrier interaction. Selberherr has approximated this mobility by an overall constant $\mu^* = 1430\,\frac{\mathrm{cm}^2}{\mathrm{V\,s}}$ [40, p. 80]. It is important to note that the mobility saturates for high electric field, and Caughey et al. have proposed a model to include the saturation [2],

$$\mu = \mu^* \left(1 + \left(\frac{\mu^* |\mathbf{E}|}{v^{\mathrm{sat}}} \right)^{\beta} \right)^{-1/\beta} , \tag{3.20}$$

where the saturation velocity v^{sat}, and β were introduced as new parameters. Different authors have published different fitting data for these parameters and we will be using the original data by Caughey et al. [2],

$$\beta = 2 , \quad v^{\mathrm{sat}} = 1.1 \times 10^7 \,\frac{\mathrm{cm}}{\mathrm{s}} .$$

The values presented here are for electrons only and one should keep in mind that all parameters $(\mu^*, v^{\mathrm{sat}}, \beta)$ depend on the carrier type.

3.2.3. Bipolar semiconductor model

The charge current flow in semiconductors is only treated in the lowest approximation as being compromised exclusively of electrons. As explained in Section 3.2.1 for each electron which has been excited above the band gap there exists a hole in the valence band. These holes contribute to the current flow as well with a positive charge.

The treatment of holes is very similar to the treatment of electrons from before. The starting point are Boltzmann distribution functions f (see equation (3.2)) but to differentiate between electron and hole specific values one introduces subscripts "n" for electrons, resp. "p" for holes

$$n(\mathbf{x}, t) = \int_{B_1} f_n(\mathbf{x}, \mathbf{k}, t) \frac{\mathrm{d}\mathbf{k}}{4\pi^3} , \quad p(\mathbf{x}, t) = \int_{B_1} f_p(\mathbf{x}, \mathbf{k}, t) \frac{\mathrm{d}\mathbf{k}}{4\pi^3} .$$

For each distribution function one derives a Boltzmann transport equation similar to equation (3.3) but there are two differences to note. One being the obvious different electrical charge sign of holes which will lead to a sign change for the drift term. The other one being that one can also include a generation-recombination term which couples both transport equations.

This model leads to the so-called *bipolar Boltzmann semiconductor equation system* which reads in their unscaled form as [17, p. 92]

$$\begin{aligned} \partial_t f_n + \mathbf{v}_n \cdot \boldsymbol{\nabla}_{\mathbf{x}} f_n - \frac{e}{\hbar}\mathbf{E} \cdot \boldsymbol{\nabla}_{\mathbf{k}} f_n &= Q_n[f_n] + I_n[f_n, f_p] \,, \\ \partial_t f_p + \mathbf{v}_p \cdot \boldsymbol{\nabla}_{\mathbf{x}} f_p + \frac{e}{\hbar}\mathbf{E} \cdot \boldsymbol{\nabla}_{\mathbf{k}} f_p &= Q_p[f_p] + I_p[f_n, f_p] \,, \end{aligned}$$

and shortened with typical abbreviations

$$\begin{aligned} \partial_t f_j + \mathbf{v}_j \cdot \boldsymbol{\nabla}_{\mathbf{x}} f_j + \frac{q_j}{\hbar}\mathbf{E} \cdot \boldsymbol{\nabla}_{\mathbf{k}} f_j &= Q_j[f_j] + I_j[f_n, f_p] \,, \quad j = n, p \,, \\ &\text{for} \quad \mathbf{x} \in \Omega \subset \mathbb{R}^3 \,,\ t > 0 \,,\ \mathbf{k} \in B_1 \subset \mathbb{R}^3 \,, \\ &\text{with} \quad f_j(\,\cdot\,, \,\cdot\,, 0) = f_{j,\text{init}} \,, \end{aligned} \tag{3.21}$$

where the particle type's charge $q_j = \pm e$ was defined (positive for holes, and negative for electrons). The generation-recombination of electron-hole pairs is included within the *generation-recombination* operators $I_j = I_j\big[f_n, f_p\big](\mathbf{x}, \mathbf{k}, t)$ [17, p. 92]

$$\begin{aligned} I_n\big[f_n, f_p\big](\mathbf{x}, \mathbf{k}, t) &= \int_{B_1} g\big(\mathbf{x}, \mathbf{k}, \mathbf{k}'\big)(1 - f_n)\Big(1 - f_p'\Big) - r\big(\mathbf{x}, \mathbf{k}, \mathbf{k}'\big) f_n f_p' \, \mathrm{d}\mathbf{k}' \,, \\ I_p\big[f_n, f_p\big](\mathbf{x}, \mathbf{k}, t) &= \int_{B_1} g\big(\mathbf{x}, \mathbf{k}', \mathbf{k}\big)\big(1 - f_n'\big)\big(1 - f_p\big) - r\big(\mathbf{x}, \mathbf{k}', \mathbf{k}\big) f_n' f_p \, \mathrm{d}\mathbf{k}' \,, \\ \text{with abbr.:} \quad f_j &= f_j(\mathbf{x}, \mathbf{k}, t), \ f_j' = f_j(\mathbf{x}, \mathbf{k}', t) \,. \end{aligned}$$

Here the local *generation rate* $g = g(\mathbf{x}, \mathbf{k}, \mathbf{k}')$ was introduced which describes the rate of creation of an electron in state $(\mathbf{x}, \mathbf{k})$, and a hole in $(\mathbf{x}, \mathbf{k}')$. Similarly, $r(\mathbf{x}, \mathbf{k}, \mathbf{k}')$ is the local *recombination rate* of electron-hole pairs. The factors of f_j have their meaning that the probability for generation-recombination is larger if the state is filled, respectively for a factor $(1 - f_j)$ the state should be empty.
The collision operators $Q_j[f_j]$ are both given as before by equation (3.5).

3.2.3.1. Bipolar diffusion scaling

The scaling process is quite similar to the one done in Section 3.2.2.2. The differences are subtle but important. One introduces another time scale τ_R which describes the average time between two consecutive generation-recombination events. This τ_R is of the order of $1 \times 10^{-9}\,\mathrm{s}$ which is a lot bigger than the average collision time $\tau_C \approx 1 \times 10^{-12}\,\mathrm{s}$ [22, p. 86].
A scaling overview is given by the following

$$\begin{aligned} \mathbf{v}_j &= \hat{v}\mathbf{v}_{j,s} \,, & \hat{v} &= \sqrt{\frac{k_B T}{m_n^*}} \,, \\ \lambda_C &= \tau_C \hat{v} \,, \quad \lambda_R = \tau_R \hat{v} \,, & & \\ \mathbf{x} &= \lambda_0 \mathbf{x}_s \,, & \lambda_0 &= \sqrt{\lambda_C \lambda_R} \,, \\ \alpha &= \frac{\lambda_C}{\lambda_0} = \sqrt{\frac{\tau_C}{\tau_R}} \,, & & \end{aligned}$$

$$\begin{aligned}
\mathbf{k} &= \hat{k}\mathbf{k}_s\,, & \hat{k} &= \frac{m_n^*\hat{v}}{\hbar}\,,\\
t &= \tau_R t_s\,, & &\\
E &= \hat{E}E_s\,, & \hat{E} &= \frac{U_T}{\lambda_0}\,,\\
f_j(\mathbf{x},\mathbf{k},t) &= f_{j,s}(\mathbf{x}_s,\mathbf{k}_s,t_s)\,, & &\\
Q_j[f] &= \frac{1}{\tau_C}Q_{j,s}[f]\,, & &\\
I_j[f_n,f_p] &= \frac{1}{\tau_R}I_{j,s}[f_n,f_p]\,. & &
\end{aligned}$$

Similar to the unipolar scaling one is using the parabolic band approximation again. The band structure approximation of holes differs from the electron's one [22, p. 85]

$$\begin{aligned}
\epsilon_n(\mathbf{k}) &= E_c + \frac{\hbar^2}{2m_n}\left|\mathbf{k}^2\right|\,,\\
\epsilon_p(\mathbf{k}) &= E_v - \frac{\hbar^2}{2m_p}\left|\mathbf{k}^2\right|\,.
\end{aligned}$$

Velocities in those bands are defined as before [22, p. 85]

$$\begin{aligned}
\mathbf{v}_n(\mathbf{k}) &= \frac{1}{\hbar}\boldsymbol{\nabla}_{\mathbf{k}}\epsilon_n = \frac{\hbar}{m_n}\mathbf{k}\,,\\
\mathbf{v}_p(\mathbf{k}) &= \frac{-1}{\hbar}\boldsymbol{\nabla}_{\mathbf{k}}\epsilon_p = \frac{\hbar}{m_p}\mathbf{k}\,.
\end{aligned}$$

The scaling velocity $\hat{v}$ leads to the following scaled dependencies [22, p. 85]

$$\begin{aligned}
& \mathbf{v}_{n,s}(\mathbf{k}_s) = \mathbf{k}_s, \quad \mathbf{v}_{p,s}(\mathbf{k}_s) = \frac{m_n}{m_p}\mathbf{k}_s\\
\implies \quad & \mathbf{v}_{j,s}(\mathbf{k}_s) = \beta_j\mathbf{k}_s\,, \quad \beta_n := 1\,, \quad \beta = \beta_p := \frac{m_n}{m_p}\,.
\end{aligned}$$

Scaling the system (3.21) gives

$$\begin{aligned}
& \left(\frac{1}{\tau_R}\partial_{t_s}f_j\right) + \left(\hat{v}\mathbf{v}_{j,s}\right)\cdot\left(\frac{1}{\lambda_0}\boldsymbol{\nabla}_{\mathbf{x}_s}f_j\right) + \frac{q_j}{\hbar}\left(\hat{E}\mathbf{E}_s\right)\cdot\left(\frac{1}{\hat{k}}\boldsymbol{\nabla}_{\mathbf{k}_s}f_j\right)\\
& \qquad = \left(\frac{1}{\tau_C}Q_{j,s}[f_j]\right) + \left(\frac{1}{\tau_R}I_{j,s}[f_n,f_p]\right)\\
\iff \quad & \frac{\tau_C}{\tau_R}\partial_{t_s}f_j + \frac{\hat{v}\tau_C}{\lambda_0}\mathbf{v}_{j,s}\cdot\boldsymbol{\nabla}_{\mathbf{x}_s}f_j + \frac{q_j\hat{E}\tau_C}{\hbar\hat{k}}\mathbf{E}_s\cdot\boldsymbol{\nabla}_{\mathbf{k}_s}f_j\\
& \qquad = Q_{j,s}[f_j] + \frac{\tau_C}{\tau_R}I_{j,s}[f_n,f_p]\\
\iff \quad & \alpha^2\partial_{t_s}f_j + \alpha(\mathbf{v}_{j,s}\cdot\boldsymbol{\nabla}_{\mathbf{x}_s}f_j - \frac{q_j}{e}\mathbf{E}_s\cdot\boldsymbol{\nabla}_{\mathbf{k}_s}f_j)
\end{aligned}$$

$$= Q_{j,s}[f_j] + \alpha^2 I_{j,s}[f_n, f_p]\,, \tag{3.22}$$

which is called the *scaled bipolar Boltzmann semiconductor equation system.*

3.2.3.2. Bipolar Hilbert expansion

For the bipolar model one can do a Hilbert expansion similar to the one done in the unipolar model's case. We start by expanding in terms of the Knudsen number α for each distribution f_j ,

$$f_j = f_{j,0} + \alpha f_{j,1} + \alpha^2 f_{j,2} + \mathcal{O}\big(\alpha^3\big)\,, \quad j = n, p\,,$$

where we will drop the scaling index “s” from now on for notational convenience. Inserting these expansions into the Boltzmann system (3.22) and collecting coefficients for powers of α gives [17, p. 110] ,

$$\alpha^0 : \qquad 0 = Q_j[f_{j,0}] \quad \Longrightarrow \quad f_{j,0} = jM_j$$

$$\begin{aligned}
\alpha^1 : \qquad & \mathbf{v}_j \cdot \boldsymbol{\nabla}_{\mathbf{x}} f_{j,0} - \frac{q_j}{e}\mathbf{E} \cdot \boldsymbol{\nabla}_{\mathbf{k}} f_{j,0} = Q_j[f_{j,1}] \\
& \text{with} \quad \mathbf{J}_n := \mu_{0,n}(\boldsymbol{\nabla}_{\mathbf{x}} n + n\mathbf{E})\,, \quad \mathbf{J}_p := -\beta\mu_{0,p}(\boldsymbol{\nabla}_{\mathbf{x}} p - p\mathbf{E}) \\
& \Longrightarrow \quad \big\langle \mathbf{k} f_{n,1} \big\rangle = -\mathbf{J}_n\,, \quad \beta \big\langle \mathbf{k} f_{p,1} \big\rangle = \mathbf{J}_p
\end{aligned} \tag{3.23}$$

$$\begin{aligned}
\alpha^2 : \qquad & \partial_t f_{j,0} + \mathbf{v}_j \cdot \boldsymbol{\nabla}_{\mathbf{x}} f_{j,1} - \frac{q_j}{e}\mathbf{E} \cdot \boldsymbol{\nabla}_{\mathbf{k}} f_{j,1} = Q_j[f_{j,2}] + I_j[f_{n,0}, f_{p,0}] \\
& \Longrightarrow \quad \partial_t \big\langle f_{j,0} \big\rangle + \beta_j \boldsymbol{\nabla}_{\mathbf{x}} \cdot \big\langle \mathbf{k} f_{j,1} \big\rangle = \big\langle I_j[f_{n,0}, f_{p,0}] \big\rangle =: U \qquad (3.24) \\
& \Longrightarrow \quad \begin{cases} \partial_t n - \boldsymbol{\nabla} \cdot \mathbf{J}_n = U \\ \partial_t p + \boldsymbol{\nabla} \cdot \mathbf{J}_p = U\,, \end{cases} \qquad (3.25)
\end{aligned}$$

where the *total generation-recombination* term $U = U(\mathbf{x}, t)$ has been introduced. The equations (3.23) and (3.25) represent the *bipolar scaled drift-diffusion equations.*

3.2.3.3. Generation-recombination

The generation-recombination term U from system equation (3.25) can be calculated if one assumes the following relation between the local generation rate g, and recombination rate r [17, p. 92] ,

$$r(\mathbf{x}, \mathbf{k}, \mathbf{k}') = \exp\bigg(\frac{\epsilon_n(\mathbf{k}) - \epsilon_p(\mathbf{k}')}{k_B T}\bigg) g(\mathbf{x}, \mathbf{k}', \mathbf{k})\,.$$

Substituting this relation into the definition (3.24) of U yields [17, p. 111]

$$U(n, p) = A\big(np - n_i^2\big)\,, \tag{3.26}$$

$$\text{with} \quad \begin{cases} n_i = n_i(E_{\text{gap}}, T) \\ A = A(\mathbf{x}) := n_i^{-2} \displaystyle\int_{\mathbb{R}^3} \int_{\mathbb{R}^3} g(\mathbf{x}, \mathbf{k}, \mathbf{k}')\, \mathrm{d}\mathbf{k}\, \mathrm{d}\mathbf{k}'\,. \end{cases}$$

3.2.3.4. Bipolar semiconductor equations

Poisson's equation from the uni- and bipolar system differ only by the newly included positive hole charge density $p = p(\mathbf{x}, t)$,

$$\begin{aligned} & \rho(\mathbf{x}, t) = p(\mathbf{x}, t) - n(\mathbf{x}, t) + C(\mathbf{x}) \\ \Longrightarrow \quad & \lambda_D^2 \boldsymbol{\nabla} \cdot \mathbf{E} = -\lambda_D^2 \nabla^2 V = \rho \\ \Longleftrightarrow \quad & \lambda_D^2 \nabla^2 V = n - p - C \,. \end{aligned} \tag{3.27}$$

This completes the *scaled, bipolar semiconductor equation system* which are made up of equations (3.23), (3.25) and (3.27).

3.2.4. Model reduction

The scaled, bipolar semiconductor equation system derived beforehand can be simplified which leads to an easier numerical handling. The simpler test cases could be incrementally extended to represent the full model once again.

3.2.4.1. Unipolar model: electrons only

Holes and electrons are included in the equation system but as a first test case one can only solve the system for one charge carrier. We chose electrons which are often rather looked at. This leads to the following equation system

$$\begin{cases} \partial_t n - \boldsymbol{\nabla} \cdot \mathbf{J} = U & (3.28) \\ \mu_0(\boldsymbol{\nabla} n - n \boldsymbol{\nabla} V) = \mathbf{J} & (3.29) \\ \lambda_D^2 \nabla^2 V = n - C \,, & (3.30) \end{cases}$$

where the index "n" on the current density has been dropped.

3.2.4.2. Steady state

The temporal behavior is usually not sought after in the context of solar cells as there are no fast changing environmental conditions. Therefore, one neglects the time dependence

$$\begin{cases} -\boldsymbol{\nabla} \cdot \mathbf{J} = U \\ \mu_0(\boldsymbol{\nabla} n - n \boldsymbol{\nabla} V) = \mathbf{J} \\ \lambda_D^2 \nabla^2 V = n - C \,. \end{cases}$$

3.2.4.3. Generation-recombination

As a further simplification one can neglect the generation-recombination of electron-hole pairs which is not physically meaningful but serves as an easy test case

$$\begin{cases} \boldsymbol{\nabla} \cdot \mathbf{J} = 0 & (3.31) \\ \mu_0(\boldsymbol{\nabla} n - n \boldsymbol{\nabla} V) = \mathbf{J} & (3.32) \\ \lambda_D^2 \nabla^2 V = n - C \,. & (3.33) \end{cases}$$

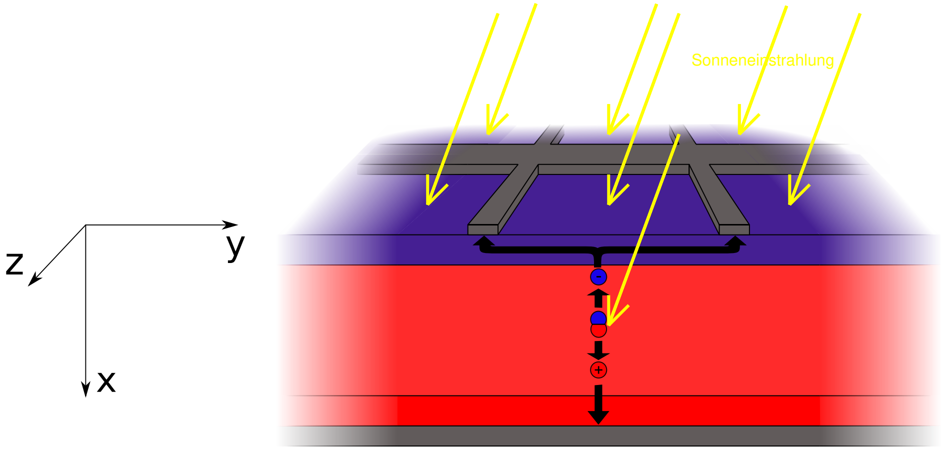

Figure 22.: A coordinate choice for the solar cell is shown. The x-direction denotes the depth of the cell whereas y-, and z-directions at $x = 0$ describe the cell's inlet for incoming solar radiation. One will assume translational invariance in y-, and z-direction for a one-dimensional model. Basic graphic taken from [8].

3.2.4.4. One-dimensional

Up to now the model has been treated as being three-dimensional but for many purposes one can approximate solar cells quite well with only one or two dimensions. For the reduction down to a one-dimensional model we assume translational symmetry in y-, and z-direction – directions perpendicular to the incident light as depicted in Figure 22. Thus, the density n, and potential V will simplify to

$$\Omega = \Omega_x \times \mathbb{R}^2 \,, \quad \Omega_x \subset \mathbb{R}$$
$$n(x,y,z) = n(x) \,, \quad V(x,y,z) = V(x) \,.$$

Using these approximations one can readily derive the following *one-dimensional, scaled semiconductor equation system*

$$\begin{cases} -J' = U \\ \mu_0\big(n' - nV'\big) = J \\ \lambda_D^2 V'' = n - C \,. \end{cases}$$

3.2.5. Boundary conditions

The device is defined within the bounded domain $\Omega \subset \mathbb{R}^3$ and we need to derive boundary and initial conditions. For the bipolar semiconductor equation systems (3.25), (3.27) the conditions are phenomenologically derived from physical intuition about the system in its thermal equilibrium state.

3.2.5.1. Thermal equilibrium state

The state where electrons and holes are in thermal equilibrium suggests that there should not be any net flows [17, p. 112]

$$\partial_t n = \partial_t p = 0 \quad \text{and} \quad \mathbf{J}_n = \mathbf{J}_p = 0 \qquad \text{in } \Omega \,.$$

Thus, using the bipolar semiconductor equations the generation and recombinations should balance each other (see equation (3.26))

$$\begin{aligned} & U = A\big(np - n_i^2\big) \overset{!}{=} 0 \\ \Longrightarrow \quad & np = n_i^2 \,, \end{aligned} \tag{3.34}$$

and the vanishing current flow gives (cf. equation (3.23)) [17, p. 113]

$$\begin{cases} 0 \overset{!}{=} \boldsymbol{\nabla} n + n\mathbf{E} = n\boldsymbol{\nabla}(\log n - V) \\ 0 \overset{!}{=} \boldsymbol{\nabla} p - p\mathbf{E} = p\boldsymbol{\nabla}(\log p + V) \,. \end{cases}$$

From this one can deduce

$$\begin{aligned} & \begin{cases} \log n - V = c_1 = \text{const} \\ \log p + V = c_2 = \text{const} \end{cases} \\ \Longrightarrow \quad & \begin{cases} n = \exp(c_1 + V) \\ p = \exp(c_2 - V) \,. \end{cases} \end{aligned}$$

The constants c_i can be determined by using equation (3.34)

$$np = n_i^2 \quad \Longrightarrow \quad c_1 + c_2 = 2 \log n_i \,,$$

and by employing the fact that the potential V is only defined up to a constant [17, p. 113]

$$\begin{aligned} & \widetilde{V} := V + \gamma \,, \quad \gamma := \log(n_i) - c_1 \\ \Longrightarrow \quad & \begin{cases} n = \exp\Big(c_1 + \widetilde{V}\Big) = n_i \exp(V) \\ p = \exp\Big(c_2 - \widetilde{V}\Big) = n_i \exp(-V) \,. \end{cases} \end{aligned} \tag{3.35}$$

Substituting theses equation (3.35) into Poisson's equation (3.27) gives a characteristic equation for the potential

$$\begin{aligned} \lambda_D^2 \nabla^2 V &= n - p - C \\ &= n_i\big(\exp(V) - \exp(-V)\big) - C \\ &= \frac{n_i}{2} \sinh(V) - C \,. \end{aligned} \tag{3.36}$$

The *boundary* $\partial\Omega$ is split up into two disjoint subsets: a *Dirichlet part* $\partial\Omega_D$, and a *Neumann part* $\partial\Omega_N$ [22, p. 105],

$$\partial\Omega = \partial\Omega_D \cup \partial\Omega_N\,, \quad \partial\Omega_D \cap \partial\Omega_N = \varnothing\,.$$

On the Dirichlet part one prescribes Dirichlet boundary conditions [17, p. 113]

$$n = n_D, \quad p = p_D, \quad V = V_D \quad \text{on } \partial\Omega_D\,,$$

and similarly, on the Neumann part one prescribes Neumann boundary conditions for the current densities $\mathbf{J}_j$, and electric field $\mathbf{E} = -\boldsymbol{\nabla} V$,

$$\mathbf{J}_j \cdot \mathbf{N} = \boldsymbol{\nabla} V \cdot \mathbf{N} = 0 \quad \text{on } \partial\Omega_N\,,$$

which is the same as when applying the definitions (3.23) of $\mathbf{J}_j$,

$$\boldsymbol{\nabla} n \cdot \mathbf{N} = \boldsymbol{\nabla} p \cdot \mathbf{N} = \boldsymbol{\nabla} V \cdot \mathbf{N} = 0 \quad \text{on } \partial\Omega_N\,,$$

where the unit outward vector $\mathbf{N}$ on the surface $\partial\Omega$ has been introduced.

The boundary functions n_D, p_D, V_D still need to be derived. This is done with physical reasoning as the Dirichlet boundary part represents *Ohmic contacts.* On Ohmic contacts we assume vanishing charges, equilibrium densities, and we also include that the voltage is a superposition of an externally applied voltage V_appl, and the internally built-in potential V_bi which stems from the doping [17, p. 113]

$$\left.\begin{aligned} 0 = \rho &= p_D - n_D + C \\ n_D p_D &= n_i^2 \\ V_D &= V_\text{appl} + V_\text{bi} \end{aligned}\right\} \quad \text{on } \partial\Omega_D\,.$$

By substitution one can find the densities' solutions [17, p. 114]

$$n_D = \frac{1}{2}\left(C + \sqrt{4n_i^2 + C^2}\right), \quad p_D = \frac{1}{2}\left(-C + \sqrt{4n_i^2 + C^2}\right).$$

The vanishing charge density leads to an equality similar to the Poisson's equation (3.36) for the built-in potential

$$\begin{aligned} 0 &= 2n_i \sinh(V_\text{bi}) - C \\ \iff \quad V_\text{bi} &= \operatorname{arsinh}\left(\frac{C}{2n_i}\right). \end{aligned}$$

Furthermore, we have to specify *initial conditions* [22, p. 106]

$$n(\,\cdot\,, 0) = n_\text{init}\,, \quad p(\,\cdot\,, 0) = p_\text{init} \quad \text{in } \Omega\,.$$

3.3. Electrical model

The modeling process of electrical transport mechanism within semiconducting layers will be explained in this section.

3.3.1. One-dimensional finite differences

The one-dimensional drift-diffusion transport model introduced in Section 3.2.4 will be discretized in space by a finite difference scheme.

3.3.1.1. Equidistant grid

The position $x \in [0, 1]$ along the depth of the cell is discretized with an *equidistant grid* of step width Δx,

$$\begin{gathered} 0 = x_L = x_0 < x_1 < \cdots < x_{N+1} = x_R = 1 \\ \Delta x = x_{i+1} - x_i = \frac{1}{N+1}\,. \end{gathered}$$

Each variable will be discretized within this equidistant grid, especially the electrons' density n and potential V,

$$n_i = n(x_i)\,, \quad V_i = V(x_i) \quad \forall\, i = 0, \dots, N+1\,.$$

3.3.1.2. Poisson's equation

The one-dimensional Poisson's equation (3.33) discretized by finite differences yields

$$\lambda^2 \frac{V_{i-1} - 2V_i + V_{i+1}}{(\Delta x)^2} = (n - C)_i + \mathcal{O}\Big((\Delta x)^2\Big)\,. \tag{3.37}$$

The voltage V and density n are under Dirichlet boundary conditions at the left and right interfaces

$$n(x_L) = n_L\,, \quad n(x_R) = n_R \tag{3.38}$$

$$V(x_L) = V_L\,, \quad V(x_R) = V_R\,. \tag{3.39}$$

The approximation (3.37) and the boundary conditions (3.38), (3.39) lead to a linear equation system for the voltage V,

$$AV = b\,, \tag{3.40}$$

where the matrix A is the usual finite difference approximation matrix for second derivatives

$$A := \begin{pmatrix} -2 & 1 & & \\ 1 & \ddots & \ddots & \\ & \ddots & \ddots & 1 \\ & & 1 & -2 \end{pmatrix} \in \mathbb{R}^{N \times N}\,,$$

and the vectors V and b are given by

$$V := (V_1, \dots, V_N)^T \in \mathbb{R}^N$$

$$
\begin{aligned}
b &:= (b_1, \ldots, b_N)^T \in \mathbb{R}^N \\
b_i &:= \begin{cases} \left(\frac{\Delta x}{\lambda}\right)^2 (n_i - C_i) - V_L \,, & i = 1 \\ \left(\frac{\Delta x}{\lambda}\right)^2 (n_i - C_i) - V_R \,, & i = N \\ \left(\frac{\Delta x}{\lambda}\right)^2 (n_i - C_i) \,, & \text{else.} \end{cases}
\end{aligned}
$$

3.3.1.3. The Continuity Equation

The continuity equation (3.31) is discretized along the equidistant grid by a finite difference scheme centered around the discretization points

$$
-U_i = J_i' = \frac{J_{i+1/2} - J_{i-1/2}}{\Delta x} + \mathcal{O}(\Delta x) \tag{3.41}
$$

$$
\text{with} \quad J(x_{i+1/2}) =: J_{i+1/2} = \mu_{i+1/2}\Big(n'_{i+1/2} - n_{i+1/2} V'_{i+1/2}\Big) \,. \tag{3.42}
$$

The naive approach to discretize all the off-grid terms within $J_{i+1/2}$ leads to stability problems which can either be tackled by refining the grid, or following the ideas by Scharfetter and Gummel [12]. At first, they approximated the electric field $V'_{i+1/2}$ and mobility term $\mu_{i+1/2}$ with finite differences. Then they assumed that the divergence of J is zero everywhere except at the discretization points x_i. This leads to an ordinary differential equation for n which is given by

$$
\big(n'(x) - \alpha n(x)\big) = \text{const} \quad \text{for} \quad x \in [x_i, x_{i+1}] \,, \tag{3.43}
$$

$$
\text{with} \quad \begin{cases} n(x_i) = n_i \,, \quad n(x_{i+1}) = n_{i+1} \\ \alpha := \frac{V_{i+1} - V_i}{\Delta x} \,. \end{cases}
$$

The solution of equation (3.43) is

$$
n(x) = \frac{n_{i+1} - n_i}{\exp(\alpha \Delta x) - 1} \Big[\exp\big(\alpha(x - x_i)\big) - 1\Big] + n_i \quad \forall\, x \in [x_i, x_{i+1}] \,.
$$

Substituting the solution n back into the current $J_{i+1/2}$ leads to

$$
\begin{aligned}
J_{i+1/2} &= \mu_{i+1/2}\Big(n'_{i+1/2} - n_{i+1/2} V'_{i+1/2}\Big) \\
&= \mu_{i+1/2}\, \alpha \frac{n_{i+1} - n_i \exp(\alpha \Delta x)}{\exp(\alpha \Delta x) - 1} \\
&= \mu_{i+1/2} \frac{V_{i+1} - V_i}{\Delta x} \frac{n_{i+1} - n_i \exp(V_{i+1} - V_i)}{\exp(V_{i+1} - V_i) - 1} \\
&= \frac{\mu_{i+1/2}}{\Delta x} \left[B(V_{i+1} - V_i) n_{i+1} - B(V_i - V_{i+1}) n_i\right] \qquad (3.44) \\
&= \frac{\mu_{i+1/2}}{\Delta x} \left[B_{i+1,i} n_{i+1} - B_{i,i+1} n_i\right] \,,
\end{aligned}
$$

where the Bernoulli function B and its shorthand notation $B_{i,j}$ were used

$$
B(x) := \begin{cases} \frac{x}{e^x - 1} \,, & x \neq 0 \\ 1 \,, & x = 0 \end{cases}
$$

$$B_{i,j} := B(V_i - V_j) \quad \forall\, i,j = 0,\, \dots\, , N+1\,.$$

Finally we can plug the solution (3.44) for $J_{i+1/2}$ into the approximation (3.41) of the continuity equation

$$\begin{aligned} U_i &= \frac{1}{(\Delta x)^2}\Big[\mu_{i-1/2}\big(-B(V_{i-1}-V_i)n_{i-1} + B(V_i - V_{i-1})n_i\big) \\ &\qquad - \mu_{i+1/2}\big(-B(V_i - V_{i+1})n_i + B(V_{i+1}-V_i)n_{i+1}\big)\Big] \\ &= \frac{1}{(\Delta x)^2}\Big[-\mu_{i-1/2}B_{i-1,i}n_{i-1} + \big(\mu_{i-1/2}B_{i,i-1} + \mu_{i+1/2}B_{i,i+1}\big)n_i \\ &\qquad - \mu_{i+1/2}B_{i+1,i}n_{i+1}\Big]\,. \end{aligned} \tag{3.45}$$

Equation (3.45) together with the boundary conditions (3.38), and (3.39) lead to a linear equation system for the density n,

$$\begin{aligned} Dn &= d \\ D = D(V) \in \mathbb{R}^{N\times N}\,,\ & n \in \mathbb{R}^N\,,\ d = d(V) \in \mathbb{R}^N\,, \end{aligned} \tag{3.46}$$

where the matrix D has a tridiagonal structure with entries

$$\begin{aligned} \big(D_{i+1,i}\big)_i &= -\big(\mu_{3/2}B_{2,1},\, \dots\, , \mu_{N-1/2}B_{N,N-1}\big) \in \mathbb{R}^{N-1} \\ \big(D_{i,i}\big)_i &= \big(\mu_{1/2}B_{1,0} + \mu_{3/2}B_{1,2},\, \dots\, , \mu_{N-1/2}B_{N,N-1} + \mu_{N+1/2}B_{N,N+1}\big) \in \mathbb{R}^N \\ \big(D_{i,i+1}\big)_i &= -\big(\mu_{3/2}B_{1,2},\, \dots\, , \mu_{N-1/2}B_{N-1,N}\big) \in \mathbb{R}^{N-1}\,. \end{aligned}$$

The right-hand side d is given by

$$d_i = \begin{cases} (\Delta x)^2 U_1 + n_L \mu_{0.5} B_{0,1}\,, & i = 1 \\ (\Delta x)^2 U_N + n_R \mu_{N+0.5} B_{N+1,N}\,, & i = N \\ (\Delta x)^2 U_i\,, & \text{else.} \end{cases}$$

The mobility terms $\mu_{i+0.5}$ will be evaluated using their definition given in equation (3.20) and approximated by finite differences

$$\begin{aligned} \mu_{i+1/2} &= \mu^T \left(1 + \left(\frac{\mu^T \left|\mathbf{E}_{i+1/2}\right|}{v^{\text{sat}}}\right)^2\right)^{-1/2} \\ \mathbf{E}_{i+1/2} &= -\boldsymbol{\nabla} V(x_{i+1/2}) \approx \frac{V_i - V_{i+1}}{\Delta x} \\ \Longrightarrow \quad \mu_{i+1/2} &= \mu^T \left(1 + \left(\frac{\mu^T}{\Delta x\, v^{\text{sat}}}\right)^2 (V_i - V_{i+1})^2\right)^{-1/2}. \end{aligned}$$

3.3.2. Newton's method

The equation systems (3.40), (3.46) are linear in either n, or V but non-linear in the other one. Thus we need to employ Newton's method for finding solutions.

3.3.2.1. Definitions

The equation systems (3.40), (3.46) can be gathered into one function

$$\mathbf{F} : \mathbb{R}^{2N} \to \mathbb{R}^{2N}, \begin{pmatrix} \mathbf{V} \\ \mathbf{n} \end{pmatrix} \mapsto \begin{pmatrix} \mathbf{F}_1 \\ \mathbf{F}_2 \end{pmatrix} = \begin{pmatrix} \mathbf{AV} - \mathbf{b} \\ \mathbf{Dn} - \mathbf{d} \end{pmatrix} .$$

Newton's method can be depicted with the following flow chart where upper indices are now used for the Newton's method iteration step.

1. At step $k = 0$ use an initial guess $\mathbf{V}^k, \mathbf{n}^k$.
2. Run $k = 1, \dots, M$ iterations of the following type.
   a) Calculate the Jacobian $\mathbf{J} := \mathbf{F}'$ for the iteration $\mathbf{J}^k := \mathbf{J}(\mathbf{V}^k, \mathbf{n}^k) \in \mathbb{R}^{2N \times 2N}$.
   b) Solve a linear equation system for $\mathbf{s}^k \in \mathbb{R}^{2N}$,

$$\begin{aligned} 0 &= \mathbf{F}^k + \mathbf{J}^k \mathbf{s}^k \quad \text{with} \quad \mathbf{F}^k := \mathbf{F}(\mathbf{V}^k, \mathbf{n}^k) \\ \implies \quad \mathbf{s}^k &= -\left(\mathbf{J}^k\right)^{-1} \mathbf{F}^k . \end{aligned}$$

   c) Update the approximation

$$\begin{pmatrix} \mathbf{V}^{k+1} \\ \mathbf{n}^{k+1} \end{pmatrix} := \begin{pmatrix} \mathbf{V}^k \\ \mathbf{n}^k \end{pmatrix} + \mathbf{s}^k .$$

3.3.2.2. The initial guess

Newton's method starts the iteration with an initial guess for the solution. The current implementation works with a stack of three different doping layers. The density is initialized as

$$\begin{aligned} n_{\text{init}}(x) &= n_L - d_0 \left(\tanh\left(\frac{x - x_1}{s} \right) - \tanh\left(\frac{x - x_2}{s} \right) \right), \quad x \in [0, L] \\ d_0 &= n_L \frac{1 - {}^1\!/_{100}}{2}, \quad s = 20\,\text{nm}, \end{aligned}$$

which assumes a specific doping profile, see equation (3.47).
The voltage is initialized by a linear interpolation of the boundary conditions

$$V_{\text{init}}(x) = V_L + \frac{V_R - V_L}{L}(x - x_L), \quad x \in [0, L] .$$

3.3.2.3. The Jacobian

The Jacobian $\mathbf{J}$ of $\mathbf{F}$ will be calculated in this section. At first we note that it consists of four blocks

$$\mathbf{J} = \begin{pmatrix} \frac{\partial \mathbf{F}_1}{\partial \mathbf{V}} & \frac{\partial \mathbf{F}_1}{\partial \mathbf{n}} \\ \frac{\partial \mathbf{F}_2}{\partial \mathbf{V}} & \frac{\partial \mathbf{F}_2}{\partial \mathbf{n}} \end{pmatrix} .$$

The first two blocks are readily computed

$$\frac{\partial \mathbf{F}_1}{\partial \mathbf{V}} = \mathbf{A}$$
$$\frac{\partial \mathbf{F}_1}{\partial \mathbf{n}} = -\left(\frac{\Delta x}{\lambda}\right)^2 \mathbf{I}_N .$$

The next block $\frac{\partial \mathbf{F}_2}{\partial \mathbf{V}}$ can be split up

$$\frac{\partial \mathbf{F}_2}{\partial \mathbf{V}} = \frac{\partial \mathbf{D}\mathbf{n}}{\partial \mathbf{V}} - \frac{\partial \mathbf{d}}{\partial \mathbf{V}} .$$

To simplify the following computations concerning the first term we will need auxiliary variables

$$\begin{aligned}
\zeta_i^- &:= \frac{\partial \mu_{i-1/2} B_{i-1,i}}{\partial V_i} = \mu_{i-1/2} B_{i-1,i}^{(i)} + \mu_{i-1/2}^{(i)} B_{i-1,i} , \quad && \mathbf{Z}^- := \left(\zeta_1^-, \dots, \zeta_N^-\right) \\
\zeta_i^+ &:= \frac{\partial \mu_{i+1/2} B_{i,i+1}}{\partial V_i} = \mu_{i+1/2} B_{i,i+1}^{(i)} + \mu_{i+1/2}^{(i)} B_{i,i+1} , \quad && \mathbf{Z}^+ := \left(\zeta_1^+, \dots, \zeta_N^+\right) \\
\eta_i^- &:= \frac{\partial \mu_{i-1/2} B_{i,i-1}}{\partial V_i} = \mu_{i-1/2} B_{i,i-1}^{(i)} + \mu_{i-1/2}^{(i)} B_{i,i-1} , \quad && \mathbf{H}^- := \left(\eta_1^-, \dots, \eta_N^-\right) \\
\eta_i^+ &:= \frac{\partial \mu_{i+1/2} B_{i+1,i}}{\partial V_i} = \mu_{i+1/2} B_{i+1,i}^{(i)} + \mu_{i+1/2}^{(i)} B_{i+1,i} , \quad && \mathbf{H}^+ := \left(\eta_1^+, \dots, \eta_N^+\right) ,
\end{aligned}$$

where we used the Bernoulli function's derivative

$$\begin{aligned}
B'(x) &= \begin{cases} -\frac{1+(x-1)e^x}{(e^x-1)^2} , & x \neq 0 \\ -1/2 , & x = 0 \end{cases} \\
B_{i,j}^{(k)} &:= \frac{\partial B(V_i - V_j)}{\partial V_k} \\
&= \left(\delta_{i,k} - \delta_{j,k}\right) B'(V_i - V_j) \quad \forall\, i,j,k = 0, \dots, N+1 .
\end{aligned}$$

After some straight-forward calculations the first term reveals a tridiagonal structure consisting of the diagonal vectors $\mathbf{D}^{(j)}, j = -1, 0, 1$,

$$\left(\frac{\partial \mathbf{D}\mathbf{n}}{\partial \mathbf{V}}\right)_{i,i+j} = \begin{cases} D_i^{(j)}, & j = -1, 0, 1 \\ 0 , & \text{else,} \end{cases}$$

and the diagonal terms can be expressed via the auxiliary variables

$$\mathbf{D}^{(1)} = \mathbf{Z}^{-}_{(2:\text{end})} \circ \mathbf{n}_{(1:\text{end}-1)} - \mathbf{H}^{-}_{(2:\text{end})} \circ \mathbf{n}_{(2:\text{end})} \in \mathbb{R}^{N-1}$$

$$\mathbf{D}^{(0)} = \left(0, -\mathbf{Z}^{-}_{(2:\text{end})} \circ \mathbf{n}_{(1:\text{end}-1)}\right) + \left(\mathbf{H}^{-} + \mathbf{Z}^{+}\right) \circ \mathbf{n} - \left(\mathbf{H}^{+}_{(1:\text{end}-1)} \circ \mathbf{n}_{(2:\text{end})}, 0\right) \in \mathbb{R}^{N}$$
$$\mathbf{D}^{(-1)} = -\mathbf{Z}^{+}_{(1:\text{end}-1)} \circ \mathbf{n}_{(1:\text{end}-1)} + \mathbf{H}^{+}_{(1:\text{end}-1)} \circ \mathbf{n}_{(2:\text{end})} \in \mathbb{R}^{N-1} .$$

Here extensive use was made of the Hadamard Product $(\cdot \circ \cdot)$, and a vector slicing notation which are defined in the appendix by equations (A.1) and (A.2).
The second term of the $\frac{\partial \mathbf{F}_2}{\partial \mathbf{V}}$-block yields

$$\left(\frac{\partial \mathbf{d}}{\partial \mathbf{V}}\right)_{ij} = \begin{cases} n_L \zeta_1^- \,, & i = j = 1 \\ n_R \eta_N^+ \,, & i = j = N \\ 0 \,, & \text{else.} \end{cases}$$

and the last block follows easily

$$\frac{\partial \mathbf{F}_2}{\partial \mathbf{n}} = \mathbf{D} \,.$$

3.4. Case studies

The previous sections have introduced a model which describes the transport of electrical charges in semiconductors. We have implemented a model which solves the equation system from Section 3.2.2.8. This section runs our implementation for various test cases – this includes tests for constant, and varying mobilities.

A solar cell depends strongly upon its doping profile C, see Section 3.2.2.7. For testing purposes we will restrict ourself to a standard n+nn+ profile consisting of piecewise constant values

$$C(x) = \begin{cases} n_0 & \text{for } x_0 \leq x < x_1 \\ n_1 & \text{for } x_1 \leq x \leq x_2 \\ n_0 & \text{for } x_2 < x \leq x_3 \,, \end{cases} \tag{3.47}$$

such as depicted in Figure 23.

3.4.1. Constant mobility

As a first test case we will look at a model of constant mobility ($\mu = \text{const}$) and vanishing source term ($U = 0$). We consider a single layer silicon cell of length L. The standard three layer doping profile from equation (3.47) is assumed and its interface positions are given by $x_i, i = 0, \ldots, 3$, and doping values by $n_i, i = 0, 1, 2$. The applied

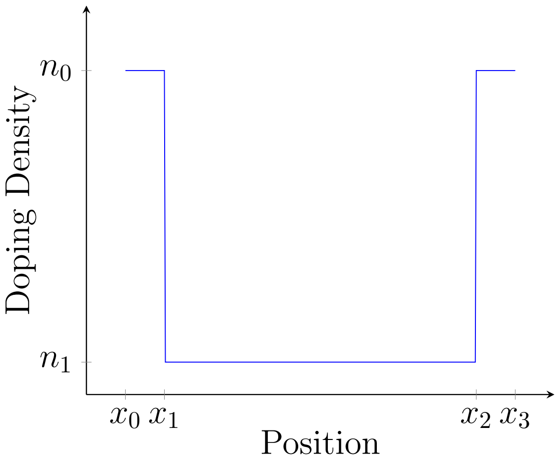

Figure 23.: The density profile of a n+nn+ diode. The positions $(x_i)_i$, and densities $(n_i)_i$ are defined by equation (3.47).

voltages at the left, and right interfaces are denoted by $V_{\text{appl,L}}, V_{\text{appl,R}}$.
Professor Jungemann implemented a model for this specific test case [18]. Some parameters were clearly stated while others had to be read off from graphs or be guessed. The simulation's parameters are collected in Table 9.

Jungemann published his results only in graphical form such that we needed to extract his results by a digitalization procedure. We employed the program "engauge" [24] which introduced an error source. The error is approximated as 0.5% of the axis length.

A comparison of densities published by Jungemann and calculations by our implementation is shown in Figure 24. One can see the raw data as well as an absolute error plot. Let n_{Sim} be the density from our implementation, respectively n_{Ref} Jungemann's density, and let the error be denoted by $e := n_{\text{Ref}} - n_{\text{Sim}}$. Then, scaled L^p-norms for the error yield

$$\frac{\|e\|_{L^p}}{\|n_{\text{Ref}}\|_{L^p}} = \begin{cases} 0.006, & p = 1 \\ 0.009, & p = 2 \\ 0.044, & p = \infty\,. \end{cases}$$

These values for the $p = 1, 2$ norms are below 1% which shows good agreement of both datasets in the overall picture. The larger error of the $p = \infty$ norm stems from differences around the interface positions x_1, x_2. This might be the result of unclear parameters for the reference model, and a small error results from the digitalization procedure as well. Around the interfaces the density has a high valued slope and the step width should be smaller to yield high resolution results.

The potential resulting for this test case has also been published by Jungemann. We extracted it again with the engauge application. In Figure 25 one can see the raw potential data of our implementation, and Jungemann's as well as their relative errors. The data show good agreement and the errors are in the error range introduced by the data extraction program.

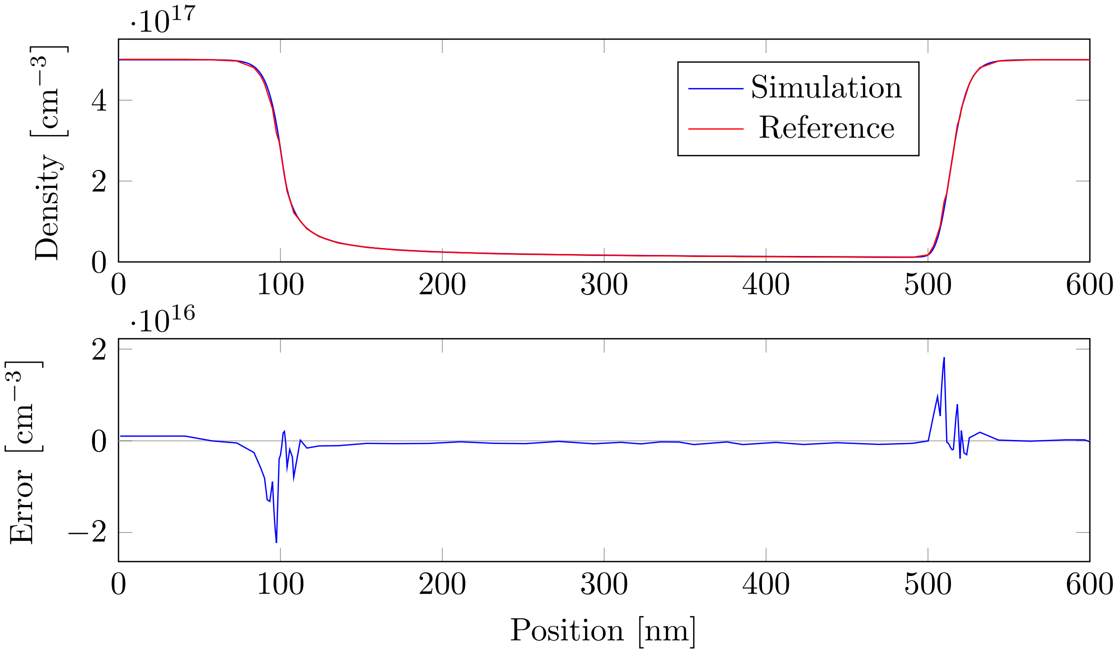

Figure 24.: The electron density resulting for a n+nn+ doping profile is shown and simulation parameters are collected within Table 9. Upper figure shows the raw data from our simulation, and the data from Jungemann's implementation taken as reference values [18]. The lower figure displays the difference of both data sets.

Parameter		Value	Clearly stated
Length	L	$600\,\mathrm{nm}$	✓
Step width	Δx	$1\,\mathrm{nm}$	✓
Interface positions	$(x_i)_{i=0,\,\dots\,,3}$	$(0, 101, 502, 600) \cdot 1\,\mathrm{nm}$	(✓, ✗, ✗, ✓)
Doping concentrations	$(n_i)_{i=0,1,2}$	$(500, 3, 500) \cdot 10^{15}\,\mathrm{cm}^{-3}$	(✓, ✗, ✓)
Applied voltage (left)	$V_{\mathrm{appl,L}}$	$0\,\mathrm{V}$	✓
Applied voltage (right)	$V_{\mathrm{appl,R}}$	$3\,\mathrm{V}$	✓
Newton iterations	M	200	✗
Mobility	μ	$1350\,\frac{\mathrm{cm}}{\mathrm{s}}$	✗
Thermal voltage	U_T	$26\,\mathrm{mV}$	✗

Table 9.: The constant mobility models is simulated for a layer of Length L with uniform discretization step width Δx. The structure is defined by its doping profile with interface positions $(x_i)_i$, and doping concentrations $(n_i)_i$ as was discussed equation (3.47). The Newton method is M-times iterated. The values represent the model published by Professor Jungemann [18], but not all values were clearly stated. The positions x_1, x_2, and density n_1 were hard to be read off from graphs. Furthermore, the values for M, μ, U_T were not given at all.

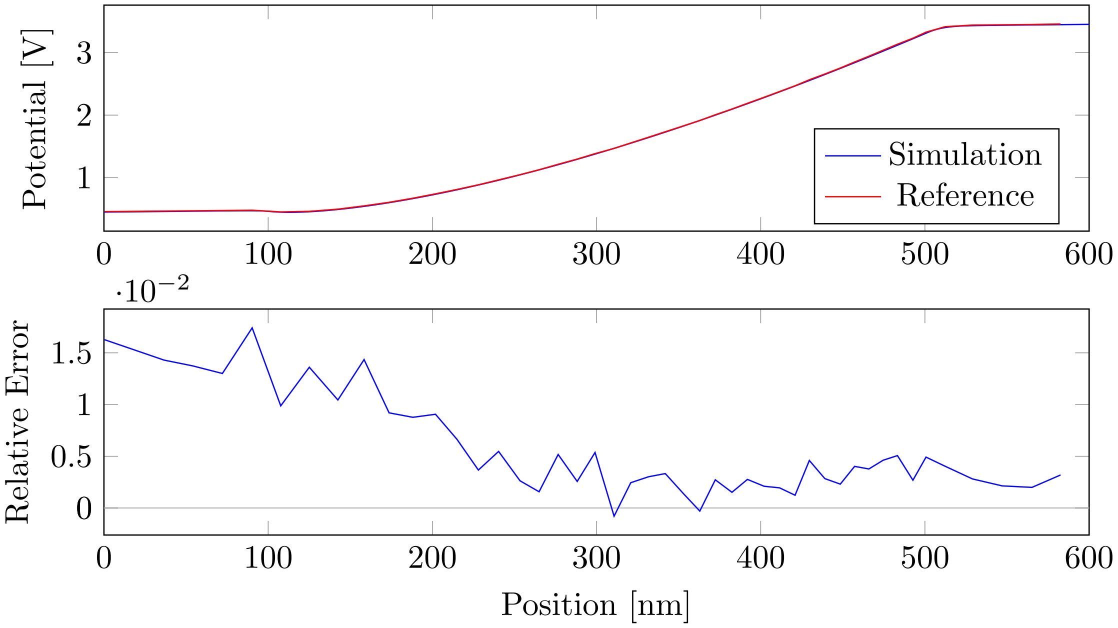

Figure 25.: The potential resulting for a n+nn+ doping profile with simulation parameters collected in Table 9. Upper figure shows the raw data from my simulation, and the data from Jungemann's implementation taken as reference values [18]. The lower figure shows their relative error.

Parameter		Value
Length	L	$600\,\mathrm{nm}$
Step width	Δx	$3\,\mathrm{nm}$
Interface positions	$(x_i)_{i=0,\dots,3}$	$(0,1,5,6)\cdot 100\,\mathrm{nm}$
Doping concentrations	$(n_i)_{i=0,1,2}$	$(500,2,500)\cdot 10^{15}\,\mathrm{cm}^{-3}$
Applied voltage (left)	$V_{\mathrm{appl,L}}$	$0\,\mathrm{V}$
Applied voltage (right)	$V_{\mathrm{appl,R}}$	$(0,1,\dots,5)\cdot 1\,\mathrm{V}$
Newton iterations	M	200
Thermal voltage	U_T	$26\,\mathrm{mV}$
Thermal mobility	μ^*	$1430\,\frac{\mathrm{cm}^2}{\mathrm{V\,s}}$
Saturation velocity	v^{sat}	$1.1\times 10^7\,\frac{\mathrm{cm}}{\mathrm{s}}$

Table 10.: Simulation parameters for a model of varying mobility are shown. The structure is described by its interface positions x_i, and doping concentrations n_i as was discussed equation (3.47). The spatial discretization uses a uniform grid of step width Δx. The values represent a test case of a Monte Carlo solver published by Professor Jungemann [19], and the mobility values were taken from Selberherr [40, p. 95].

3.4.2. Varying mobility

Our implementation of the drift-diffusion equations also handles potential-dependent mobilities $\mu = \mu(V)$. This has been introduced in equation (3.20). The implementation will be validated with a test case presented in a book by Professor Jungemann [19]. Jungemann implemented a Monte Carlo solver for the one-dimensional drift-diffusion equations which creates an issue as our model is based upon finite difference approximations. The validation will be a *positive only* test that is to say, if the Monte Carlo solver's data agree with the data from our model then our implementation is validated but there is no conclusion in the case of disagreement.

Jungemann's setup for a potential-dependent mobility is similar to the one introduced in Section 3.4.1 and we have listed the simulation's parameters in Table 10. The data has been read out from graphs within his book in a similar manner as in the section before which introduces an error source again.

The simulation has been run for different voltage offsets at the right interface. The data sets by Jungemann and from our implementation are shown for applied voltages $V_{\mathrm{appl,R}} = 0\,\mathrm{V}, 2\,\mathrm{V}, 4\,\mathrm{V}, 5\,\mathrm{V}$ in Figure 26. The figure shows the raw data sets from both implementations for each applied voltage within a logarithmically scaled plot as was done in Jungemann's book. Below each figure with raw data a residual plot of the logarithmically scaled data is shown. The residuals $r = r(x)$ are shown in the form

$$r = (\log_{10} n)_{\mathrm{Ref}} - \log_{10}(n_{\mathrm{Sim}})\,,$$

where $(\log_{10} n)_{\mathrm{Ref}}$ is given by the reference value which was read out from a logarithmic plot and n_{Sim} is the data resulting from our implementation. One can see that both data sets agreement well inside the error bounds given from the data extraction routine.

Similarly, Figure 27 shows the comparison of the book's potential data and of our implementation's. The data sets do differ in the order of 5% relative error which seemed acceptable for us if one considers that we compare a Monte Carlo solver to our scheme using finite differences.

3.4.3. Optical and electrical coupling

The optical, and electrical simulations can be coupled by considering the generation rate G of electron-hole pairs. It is the result of optical absorption and acts as a source term for the drift-diffusion equation system, see equation (3.28). Recombination is still not taken into account.

We present here a simulation for a simple one-layered silicon cell with a bare air-silicon front interface, and a silver back contact. The bulk layer is of length L and position-dependent functions will be sampled by a uniformly distributed grid consisting of M nodes.

As incident spectrum we consider the usual AM1.5g spectrum. The total intensity has been scaled to represent different amounts of incident light. This is done by using an overall scaling factor s which is measured in units of 1 Sun. Here 1 Sun denotes the standard illumination of the AM1.5g spectrum, and 0 Sun denotes no incident light.

Electronically the cell is modeled for a n+nn+ diode consisting of the usual doping profile, see equation (3.47). It consists of interface positions $(x_i)_i$, and doping densities $(n_i)_i$. The cell is not under any externally applied voltages V_{appl} such that the illumination's effect is more easily visible. The exact values are gathered in Table 11.

The effect of shining different incident illuminations on a cell is shown in Figure 28. The upper row shows raw data whereas the lower row shows the difference resulting from using incident illumination versus no illumination. One should note here the overall "smallness" of the illumination's effect as the differences are in the order of 10^{-4} for the density, resp. 10^{-3} for the potential. Furthermore, the effect of the incident illumination is symmetric on density and potential w.r.t. position space which needs further investigation. This is is why we have compared our simulation to reference data gathered from the AFORS-HET program. Figure 29 shows a comparison of our simulation, and the reference data in the following form: The upper row displays raw density, and potential data for different illuminations. Whereas the difference of reference, and our simulation for each illumination are shown in the lower row. The density shows good agreement for most positions except around the interface positions where the reference solution is actually discontinuous. The difference does not change as we increase the illumination, and we conclude that the reference program probably includes higher order physical effects which have a stronger impact here than the illumination. For the potential one should note that both data sets are only defined upto a global shift. The potentials were shifted such that their minima are exactly at zero, and then normalized such that the overall maximum is exactly one. This gives reason to the large error at the outer edges. Concerning the illumination one can see that its

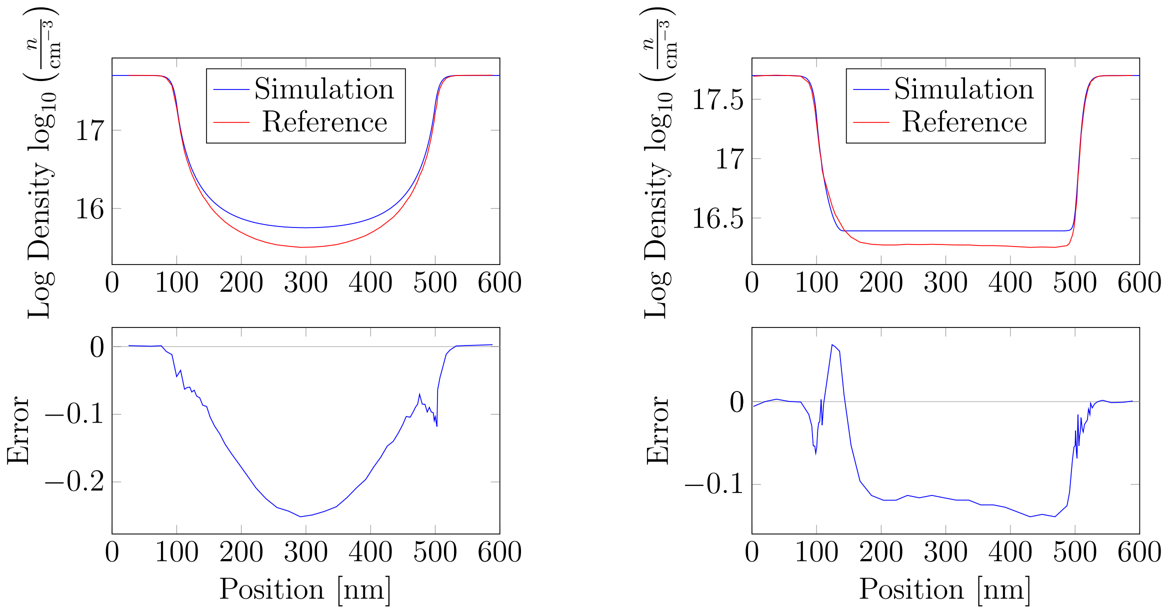

(a) Right applied voltage $V_{\mathrm{appl,R}} = 0\,\mathrm{V}$ (b) Right applied voltage $V_{\mathrm{appl,R}} = 2\,\mathrm{V}$

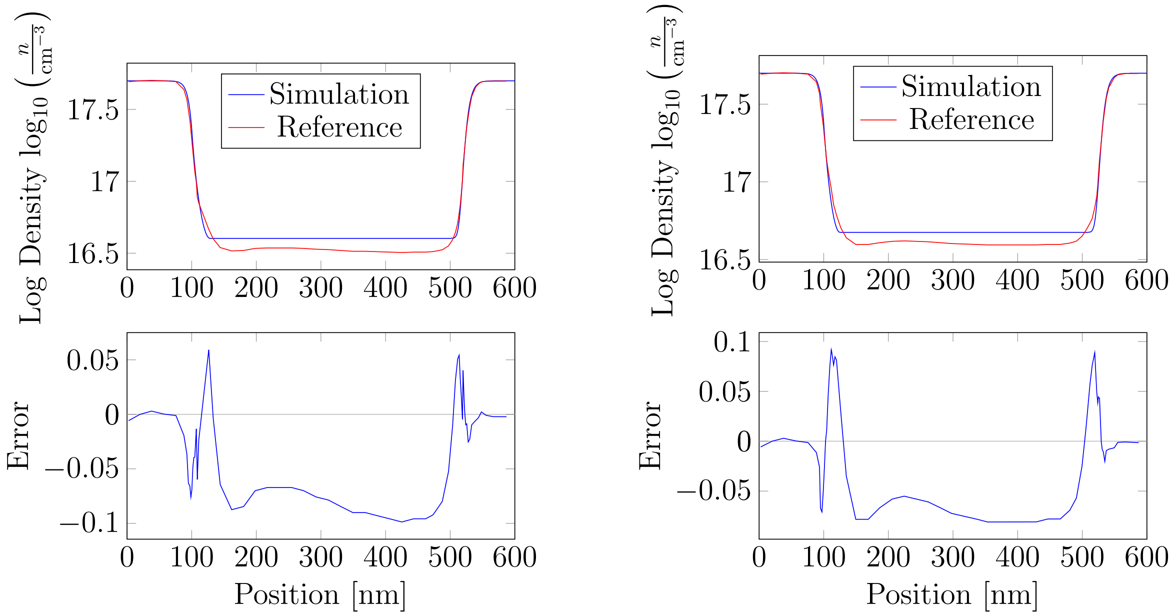

(c) Right applied voltage $V_{\mathrm{appl,R}} = 4\,\mathrm{V}$ (d) Right applied voltage $V_{\mathrm{appl,R}} = 5\,\mathrm{V}$

Figure 26.: Electron densities from simulations are compared to the Monte Carlo implementation by Jungemann [19]. The subfigures (a) to (d) show densities for different right applied voltages $V_{\mathrm{appl,R}}$. The densities are shown as logarithmic data as was done in the book by Jungemann and the error is w.r.t. these logarithmic data sets.

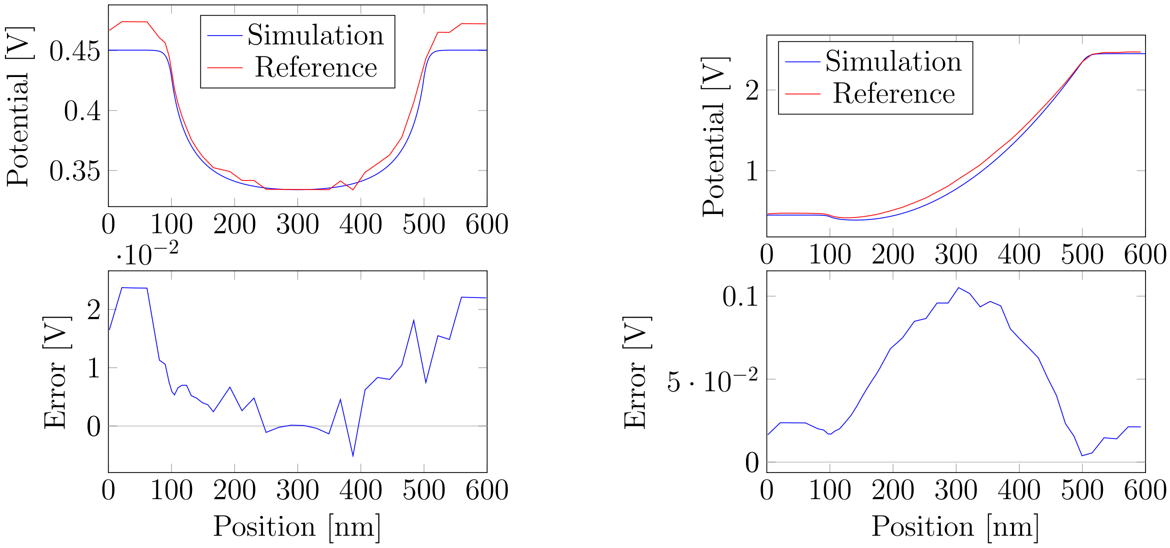

(a) Right applied voltage $V_{\mathrm{appl,R}} = 0\,\mathrm{V}$

(b) Right applied voltage $V_{\mathrm{appl,R}} = 2\,\mathrm{V}$

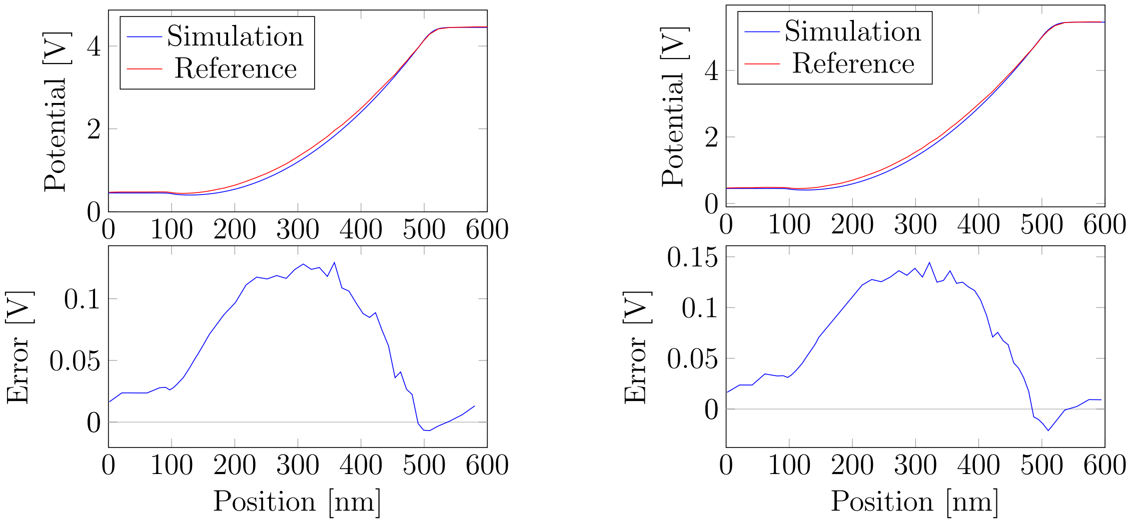

(c) Right applied voltage $V_{\mathrm{appl,R}} = 4\,\mathrm{V}$

(d) Right applied voltage $V_{\mathrm{appl,R}} = 5\,\mathrm{V}$

Figure 27.: Potentials from simulations are compared to the Monte Carlo implementation by Jungemann [19]. The subfigures (a) to (d) show potentials for different right applied voltages $V_{\mathrm{appl,R}}$ and the errors of both data sets.

Parameter		Value
Structure		
ARC layer		–
Bulk material		Silicon
Bulk length	L	$1\,\mu\text{m}$
Spatial nodes	M	1000
Rear contact		Silver
Optics		
Spectrum	I_0	AM1.5g
Scaling	s	$(0, 0.1, \ldots, 1) \cdot 1\,\text{Sun}$
Transport		
Interface positions	$(x_i)_{i=0,\ldots,3}$	$(0, 1, 9, 10) \cdot 100\,\text{nm}$
Doping concentrations	$(n_i)_{i=0,1,2}$	$(500, 1, 500) \cdot 10^{15}\,\text{cm}^{-3}$
Applied voltage (left)	$V_{\text{appl,L}}$	$0\,\text{V}$
Applied voltage (right)	$V_{\text{appl,R}}$	$0\,\text{V}$
Newton iterations	N	200
Thermal voltage	U_T	$26\,\text{mV}$
Thermal mobility	μ^*	$1000\,\frac{\text{cm}^2}{\text{V s}}$
Saturation velocity	v^{sat}	$1.1 \times 10^7\,\frac{\text{cm}}{\text{s}}$

Table 11.: Numerical parameters used for the coupled simulation.

effect is only visible in the inner range.

Altogether, our coupled model as well as the reference program AFORS-HET showed symmetric behavior. This is intuitively not clear as the illumination is a strongly non-symmetric influence on the system. The reference program gave results differing to our simulation's which is probably caused by hihger order effects as it includes advanced physical effects for the charge transportation, e.g. Schottky contacts, bandgap narrowing.

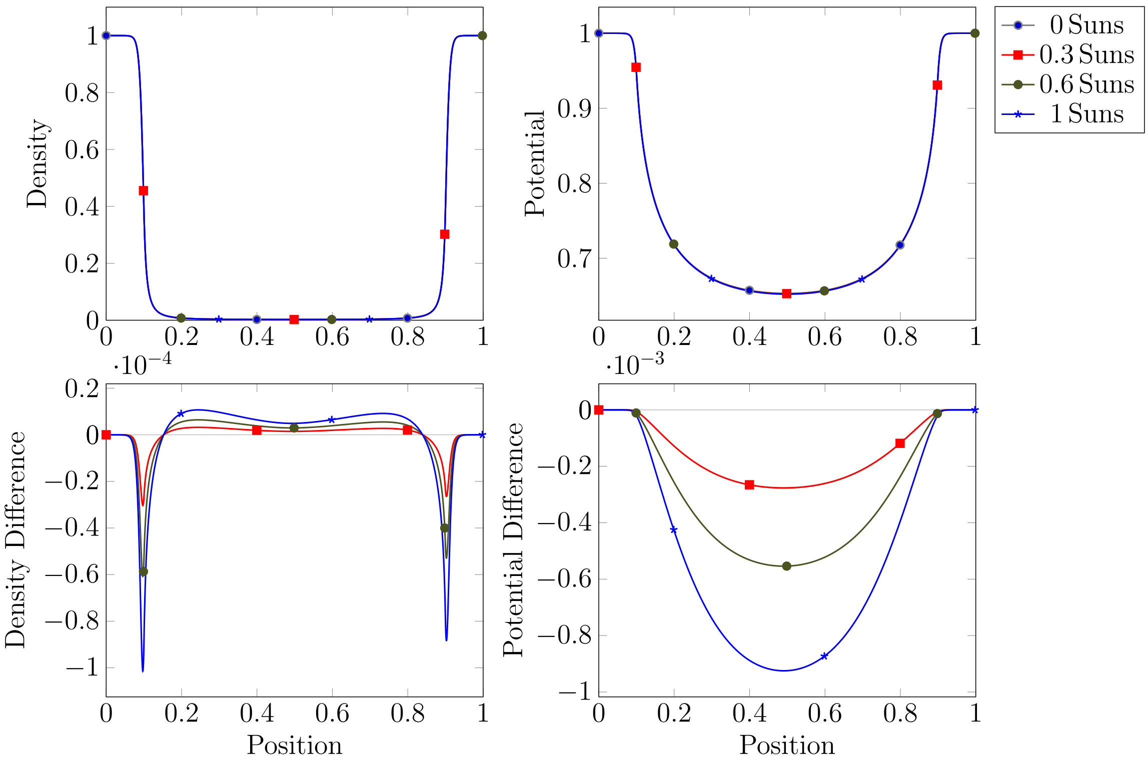

Figure 28.: The charge transport simulation's result for the coupled model are shown. The simulation corresponds to parameters given in Table 11. Different incident intensities were used which are given by an overall scaling factor in units of 1 Sun which represents the full AM1.5g spectrum.

The upper row shows the raw data for density, and potential. Both are scaled by their maximal value resulting from no illumination, and the position is scaled by the total length. The lower row shows the differences of using a coupled model with incident illumination compared to a cell in the dark.

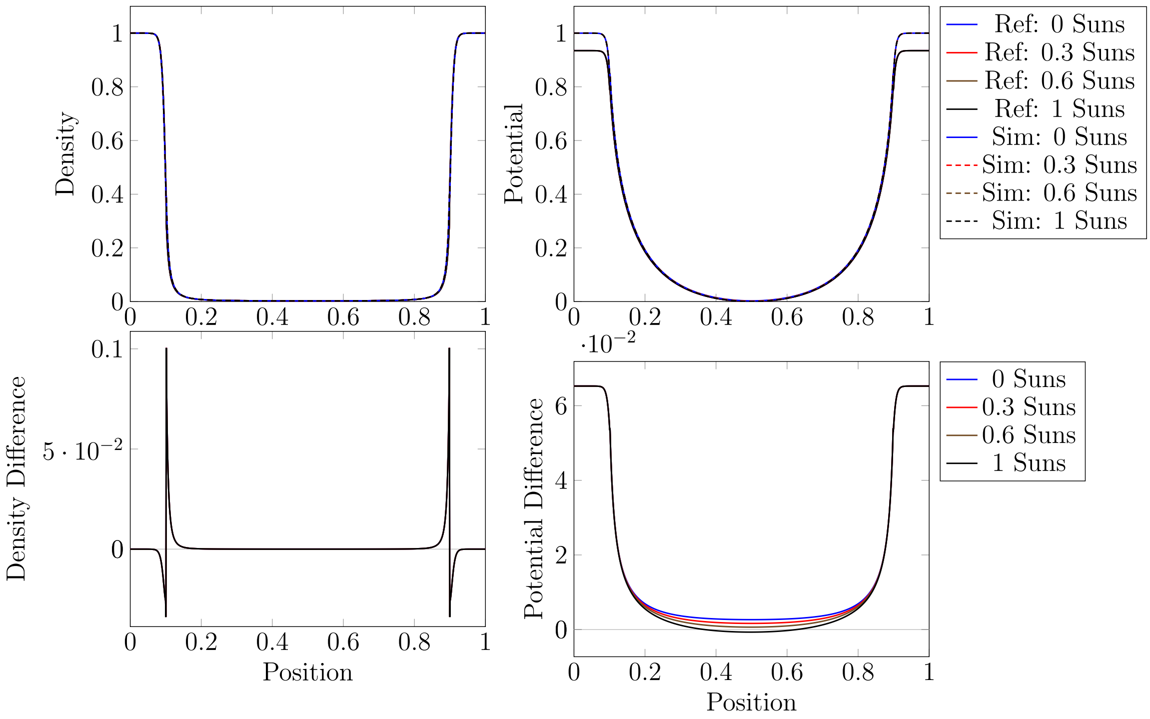

Figure 29.: The charge transport simulation's result for the coupled model are compared to results obtained from the reference program AFORS-HET. The simulation corresponds to parameters given in Table 11. Different incident intensities were used which are given by an overall scaling factor in units of 1 Sun which represents the full AM1.5g spectrum.
The upper row shows the raw data for density, and potential. The density has been scaled by its maximal value whereas the potentials were first shifted such that their minima were zero, and finally normalized into the range $[0, 1]$. The position is scaled by the total length. In the lower row the differences from of our simulation w.r.t the reference data is shown for each illumination.

4. Conclusion and Outlook

Within this thesis the two physically governing processes of photovoltaic devices were regarded. On the one hand the optical absorption of different incident spectra was discussed using a Lambert-Beer model. As the Lambert-Beer model is an incoherent light model, and inherently one-dimensional we implemented another coherent wave model using the Yee algorithm.

On the other hand, the electrical charge transport within semiconductors was also regarded in this thesis. A drift-diffusion model describing the charge transportation was implemented.

Conclusion

The absorption of sun light is of utmost importance in photovoltaic devices. Light can be modeled at different accuracies: for incoherent light the Lambert-Beer model is usually used. For higher accuracies, and higher dimensions one can solve the Maxwell's equations directly using the Yee algorithm.

The Lambert-Beer model was studied by using a self-made solver written in MATLAB®. An anti-reflection coating was introduced and tested against reference data. We were able to significantly lower the reflection in the overall spectrum as well as diminishing it altogether around the solar spectrum's peak. Light absorption within the solar cell's bulk layers generates electron-hole pairs. The generation rate strongly depends on the materials used, and the incident spectrum. We investigated the generation rate for constant spectra, and material parameters as well as for cases of varying data. The simulations' results were compared to data obtained from a reference program and errors lay within reasonable ranges.

For incident solar spectrum we used the industry standards AM1.5g,d which are spectrally defined on a fine grid by step widths of around $\Delta\lambda = 1\,\mathrm{nm}$. In contrast the obtained material parameters were given on much coarser grids often with step widths above $\Delta\lambda = 50\,\mathrm{nm}$. To calculate electron-hole generation rates one needs to define an underlying grid. The dependence of the calculated generation rates upon grids using different step widths was investigated. We concluded that even for simple setups one should use the fine grid defined by the incident solar spectrum.

The calculated generation rates were sampled in position space using a uniformly distributed grid. We measured errors introduced by using different node numbers. The convergence order in different L^p-norms ($p = 1, 2, \infty$) were all estimated to be around 4. Our analysis showed that for single layer cells one can achieve relative accuracies of below 10^{-5} with node numbers as low as $N = 100$.

For comparison purposes between coherent and incoherent light models we have implemented a rigorous Maxwell solver based on the Yee algorithm. For a single layer bulk system the calculated generation rates differed in their decaying rates. This result is still open for discussion and it could be the result from not implementing the exact same test cases for both models.

The second process within solar cells is the charge transport. The transport process can be modeled by the drift-diffusion equations which is an approximation to the general Boltzmann transport equation in semiconductors. Within this thesis the derivation has been done in great detail and the approximations needed were highlighted.

The drift-diffusion equations were implemented in a one-dimensional unipolar model. As the equations depend largely on the electron mobility μ we have run simulations for constant as well as varying mobilities. A test case for constant mobility was run against data obtained from a published reference and the varying mobility was run against a Monte Carlo solver for the Boltzmann transport equation. Every simulation showed good agreement.

The interesting case of coupling between the optical, and electrical model was also regarded. Our test case showed differences for a cell under illumination compared to a cell in the dark which were rather small, and symmetrical. These surprising results might be caused by our specific test case as we were using very thin sheets of cells.

Outlook

For an incoherent light model in higher dimensions one could extend the Lambert-Beer model using a ray tracing algorithm. They have been used as early as 2006 [53] to simulate absorptions within solar cells. Their resolution, and computational cost are supposedly in between Lambert-Beer models, and Yee's implementations [21].

The interfaces of cells are of great interest as specially constructed ones can significantly increase efficiencies. To tackle such textured interfaces one needs the above mentioned ray tracing or Yee models. Baker et al. [1] extended the usual planar interfaces to textured structures. They modeled different possible interfaces such as regular upright pyramids, regular inverted pyramids, random upright pyramids, and grooves. The truly newly introduced idea in their paper has been to parametrize the one-dimensional generation rate in a clever way. Instead of using the usual coordinate z describing the depth of the cell they introduce a parameter ζ describing the distance from the frontal surface. By using this ζ they were able to run detailed analysis of differently structured interfaces.

The incident illumination for conventional cells is just on one side but for high efficiency cells one can also think about bifacial illumination. This changes the overall layout of textured interfaces as has been shown by Wöhrle et al. [51]. The rear sides should be pyramidal textured for rear illumination exceeding $250\,\frac{\mathrm{W}}{\mathrm{m}^2}$ as opposed to a planar interface for lower illumination where they have assumed the normalized frontal illumination of $1000\,\frac{\mathrm{W}}{\mathrm{m}^2}$. Furthermore, even negligible rear illumination already changed the optimal rear contact spacing. Wöhrle et al. have done their simulations using a transfer matrix model by the Sentaurus Device software for textured front sides, and planar rear sides. The bulk's absorption was simulated by Sentaurus Device' ray tracer, and textured rear interfaces by an external ray tracer.

Ray tracing is computational expensive and one would like to yield similarly good results by less computational expensive approximations. Fell et al. [7] have introduced a model which needs just lumped input parameters. They suggested to use the wavelength-dependent external front surface transmission T_{ext}, as well as the path length enhancement Z as input parameters. This yields a rapid speed improvement and they also showed that the newly introduced errors for cells under usual working conditions are not significant.

Eisenlohr et al. [6] have introduced a new technique to efficiently compute the absorption in two dimensions given front and rear sided interfaces which operate in different optical regimes. One instance might be a silicon cell with pyramid frontal surface, and rear sided grating textures. The pyramidal front might be efficiently computed using ray tracers while the rear would need full FDTD simulation. The idea from Eisenlohr et al. has been to outsource the interfaces into single computations. This is done by grouping incident light into bins for ranges of solid angles. For each bin the interaction with the textured surface is computed using the desired model, e.g. ray tracers, and FDTD. This interaction is saved within a matrix that will act on the incident power density – saved within a vector according to the distribution along the solid angles'. The light will be propagated within the structure as incoherent light by the known Lambert-Beer model. The model by Eisenlohr et al. has also been extended into the third dimension [46] and their models are called Optical Properties of Textured Optical Sheets (OPTOS).

Different cell layouts can be analyzed by their overall efficiency and by using free energy loss analysis (FELA) one can compare the effect of different loss mechanisms on the resulting efficiency. This opens the door for optimization processes. Wöhrle et al. [52] have simulated a back-contact back-junction solar cell and optimizing with FELA increased the efficiency from 20.1% towards 21.2%.

The drift-diffusion implementation used in this work could be extended in multiple ways. On the one hand one can include a greater class of possible doping densities which involves a more general approach for initial guesses of Newton's method. On the other hand, one can extend the solver towards higher dimensions. Here, dimension two is of great interest as solar cells can often be well approximated by a two-dimensional structure. Also, the implementation uses a unipolar model and the inclusion of hole charges is necessary to represent broader classes of semiconducting devices.

The Boltzmann transport equation yields the drift-diffusion equations as lowest order diffusive approximation and for greater accuracy one could also include higher orders. This would lead to energy-transport, or SHE models [17]. A different scaling of the Boltzmann transport equation leads to hydrodynamical models which can be interpreted as an approximation in-between Boltzmann transport, and drift-diffusion model [17].

One could also implement a Monte Carlo solver for the Boltzmann transport equations within semiconductors as has been done by Jacoboni and Reggiani [16]. This would help to validate the above mentioned models as one could provide reference solutions. For very thin cells one could also use models from quantum mechanics. This would yield equivalents of the afore-mentioned models, such as quantum drift-diffusion, or quantum energy-transport model [17].

One could also work towards implementing perovskite solar cells which have been in the focus of research for the last years. Their efficiencies have currently increased from around 4% in 2009 [20] to above 22% in 2017 [54]. Simulations have been run by Huang et al. [13] with standard drift-diffusion solvers and only little modifications.

Organic materials are also of great interest as they promise low production cost, and open up flexible design choices. Current developments have also shown good results with possible efficiencies far above 10% [56]. Equations derived for inorganic materials are usually prone to errors as organic materials show different characteristics, such as relatively low carrier mobilities. A recent publication by Neher et al. [28] has shown simulation results, and comparison to an analytical model as well as introducing a new figure of merit α specific for organic solar cells.

Appendices

A. Definitions and Constants

The *Hadamard product* defines the element-wise product of vectors which is often used in computer science. It is given by [50]

$$\begin{aligned} \forall\, v = (v_i)_i, w = (w_i)_i \in \mathbb{R}^n : \quad & v \circ w \coloneqq u = (u_i)_i \in \mathbb{R}^n \\ \text{with} \quad u_i \coloneqq v_i w_i \quad & \forall\, i = 1, \ldots, n\,. \end{aligned} \tag{A.1}$$

An example is

$$v \coloneqq (v_1, v_2, v_3),\; w \coloneqq (w_1, w_2, w_3) \quad \Longrightarrow \quad v \circ w = (v_1 w_1, v_2 w_2, v_3 w_3)\,.$$

Within the thesis extensive use was made of a *vector slicing notation.* Its definition is given by

$$\forall\, v = (v_i)_i \in \mathbb{R}^n \;\forall\, k, l \in \mathbb{N},\; k \leq l \leq n : \quad v_{(k:l)} \coloneqq (v_k, v_{k+1}, \ldots, v_l)\,, \tag{A.2}$$

and a shorthand notation for the last entry

$$v_{(k:\text{end})} \coloneqq (v_k, v_{k+1}, \ldots, v_n)\,.$$

An example is as follows

$$v \coloneqq (v_1, v_2, v_3) \quad \Longrightarrow \quad v_{(1:2)} = (v_1, v_2), \quad v_{(2:\text{end})} = (v_2, v_3)\,.$$

Especially, note that the first element is indexed by $i = 1$.

Physical *constants* were used throughout computations within this thesis. Table 12 shows a list of values that were used.

Constant		Value
elementary charge	e	$1.602\,176\,487 \times 10^{-19}\,\mathrm{C}$
Planck constant	h	$6.626\,068\,96 \times 10^{-34}\,\mathrm{Js}$
(reduced) Planck constant	$\hbar \coloneqq \frac{h}{2\pi}$	$1.054\,571\,628 \times 10^{-34}\,\mathrm{Js}$
speed of light	c	$299\,792\,458\,\mathrm{m/s}$
vacuum permeability	μ_0	$4\pi \times 10^{-7}\,\mathrm{Vs/Am}$
vacuum permittivity	ϵ_0	$8.854\,187\,817 \times 10^{-12}\,\mathrm{As/Vm}$

Table 12.: A list of constants which were used in this thesis. Values were taken from Demtröder [5, p. 496].

Bibliography

[1] S. C. Baker-Finch and K. R. McIntosh. "One-dimensional photogeneration profiles in silicon solar cells with pyramidal texture." In: *Progress in Photovoltaics: Research and Applications* 20.1 (2012), pp. 51–61.

[2] D. Caughey and R. Thomas. "Carrier mobilities in silicon empirically related to doping and field." In: *Proceedings of the IEEE* 55.12 (1967), pp. 2192–2193.

[3] *COMSOL - Multiphysics.* URL: `https://www.comsol.com/comsol-multiphysics` (visited on 2017-08-28).

[4] M. G. Deceglie. "Advanced silicon solar cell device physics and design." PhD thesis. California Institute of Technology, 2013.

[5] W. Demtröder. *Elektrizität und Optik. German.* Springer, Berlin, 2008. DOI: `10.1007/978-3-540-68219-6`.

[6] J. Eisenlohr et al. "Matrix formalism for light propagation and absorption in thick textured optical sheets." In: *Optics express* 23.11 (2015), A502–A518.

[7] A. Fell, K. R. McIntosh, and K. C. Fong. "Simplified device simulation of silicon solar cells using a lumped parameter optical model." In: *IEEE Journal of Photovoltaics* 6.3 (2016), pp. 611–616.

[8] *File:Solarzelle Funktionsprinzip2.svg — Wikimedia Commons, the free media repository.* Wikimedia Commons. 2015. URL: `https://commons.wikimedia.org/wiki/File:Solarzelle_Funktionsprinzip2.svg` (visited on 2017-10-01).

[9] Filmmetrics. *Refractive index of GaAs.* URL: `http://www.filmetrics.com/refractive-index-database/GaAs/Gallium-Arsenide` (visited on 2017-07-14).

[10] J. G. Fossum. "Computer-aided numerical analysis of silicon solar cells." In: *Solid-State Electronics* 19 (4 1976). DOI: `10.1016/0038-1101(76)90022-8`.

[11] J. Gray. "Two-dimensional modeling of silicon solar cells. [SCAP2D]." PhD thesis. Purdue Univ.,Lafayette, IN, 1982-01-01.

[12] C. Gwyn, D. Scharfetter, and J. Wirth. "The analysis of radiation effects in semiconductor junction devices." In: *IEEE Transactions on nuclear science* 14.6 (1967), pp. 153–169. DOI: `10.1109/TNS.1967.4324787`.

[13] L. Huang et al. "Electron transport layer-free planar perovskite solar cells: Further performance enhancement perspective from device simulation." In: *Solar Energy Materials and Solar Cells* 157 (2016), pp. 1038–1047.

[14] H. Ibach and H. Lüth. *Festkörperphysik: Einführung in die Grundlagen*. Springer-Verlag, 2009. DOI: `10.1007/978-3-540-85795-2`.

[15] J. D. Jackson and R. F. Fox. “Classical electrodynamics.” In: *American Journal of Physics* 67.9 (1999), pp. 841–842.

[16] C. Jacoboni and L. Reggiani. “The Monte Carlo method for the solution of charge transport in semiconductors with applications to covalent materials.” In: *Rev. Mod. Phys.* 55 (3 1983-07), pp. 645–705. DOI: `10.1103/RevModPhys.55.645`.

[17] A. Jüngel. *Transport equations for semiconductors*. Vol. 773. Springer, 2009.

[18] C. Jungemann. “Numerical Device Simulation.” Lecture Notes. 2015-07.

[19] C. Jungemann and B. Meinerzhagen. *Hierarchical device simulation: the Monte-Carlo perspective*. Springer Science & Business Media, 2012.

[20] A. Kojima et al. “Organometal halide perovskites as visible-light sensitizers for photovoltaic cells.” In: *Journal of the American Chemical Society* 131.17 (2009), pp. 6050–6051.

[21] J. Krc et al. *Optical modeling and simulation of thin-film photovoltaic devices*. CRC Press, 2013.

[22] P. Markowich, C. Ringhofer, and C. Schmeiser. *Semiconductor Equations*. Springer, 1990.

[23] K. Misiakos and D. Tsamakis. “Accurate measurements of the silicon intrinsic carrier density from 78 to 340 K.” In: *Journal of Applied Physics* 74 (1993-01-01), p. 3293. DOI: `10.1063/1.354551`.

[24] M. Mitchell et al. *markummitchell/engauge-digitizer: Version 10 Map Support*. DOI: `10.5281/zenodo.439621`.

[25] J. N. Munday and H. A. Atwater. “Large Integrated Absorption Enhancement in Plasmonic Solar Cells by Combining Metallic Gratings and Antireflection Coatings.” In: *Nano Letters* 11.6 (2011), pp. 2195–2201. DOI: `10.1021/nl101875t`.

[26] A. Musset and A. Thelen. “IV Multilayer Antireflection Coatings.” In: *Progress in Optics* 8 (1970), pp. 201–237.

[27] *NASA: Sun Fact Sheet*. URL: `https://nssdc.gsfc.nasa.gov/planetary/factsheet/sunfact.html` (visited on 2017-07-13).

[28] D. Neher et al. “A new figure of merit for organic solar cells with transport-limited photocurrents.” In: *Scientific reports* 6 (2016), p. 24861.

[29] A. Peraiah. *An Introduction to Radiative Transfer: Methods and applications in astrophysics*. Cambridge University Press, 2002.

[30] M. N. Polyanskiy. *Refractive index database*. URL: `https://refractiveindex.info` (visited on 2017-06-17).

[31] M. N. Polyanskiy. *Refractive index database - Ag by Aspnes*. URL: `https://refractiveindex.info/?shelf=main&book=Ag&page=Aspnes` (visited on 2017-07-14).

[32] M. N. Polyanskiy. *Refractive index database - Al by Aspnes.* URL: `https://refractiveindex.info/?shelf=main&book=Al&page=Aspnes` (visited on 2017-07-14).

[33] M. N. Polyanskiy. *Refractive index database - GaAs by Aspnes.* URL: `https://refractiveindex.info/?shelf=main&book=GaAs&page=Aspnes` (visited on 2017-07-14).

[34] M. N. Polyanskiy. *Refractive index database - GaAs by Jellison.* URL: `http://refractiveindex.info/tmp/main/GaAs/Jellison.csv` (visited on 2017-07-14).

[35] M. N. Polyanskiy. *Refractive index database - Si by Aspnes.* URL: `https://refractiveindex.info/?shelf=main&book=Si&page=Aspnes` (visited on 2017-07-14).

[36] M. N. Polyanskiy. *Refractive index database - Si3N4 by Philipp.* URL: `https://refractiveindex.info/?shelf=main&book=Si3N4&page=Philipp` (visited on 2017-07-20).

[37] *Reference Solar Spectral Irradiance: Air Mass 1.5.* URL: `http://rredc.nrel.gov/solar/spectra/am1.5/` (visited on 2017-07-13).

[38] J. Renshaw. "Numerical modeling and fabrication of high efficiency crystalline silicon solar cells." PhD thesis. Georgia Institute of Technology, 2013.

[39] D. Rover, P. Basore, and G. Thorson. "Solar cell modeling on personal computers." In: *IEEE photovoltaic specialists conference. 18.* 1985, pp. 703–709.

[40] S. Selberherr. *Analysis and simulation of semiconductor devices.* Springer Verlag/Wien, 1984.

[41] *SILVACO - Atlas.* URL: `https://www.silvaco.com/products/vwf/atlas/device3d/device3d_br.html` (visited on 2017-08-28).

[42] S. H. Simon. *The Oxford solid state basics.* OUP Oxford, 2013.

[43] *Solar cell structure.* URL: `http://pveducation.org/pvcdrom/solar-cell-structure` (visited on 2017-09-12).

[44] *SYNOPSYS - Sentaurus.* URL: `https://www.synopsys.com/silicon/tcad/device-simulation/sentaurus-device.html` (visited on 2017-08-28).

[45] W. Tress. "Device Physics of Organic Solar Cells: Drift-Diffusion Simulation in Comparison with Experimental Data of Solar Cells Based on Small Molecules." PhD thesis. Technische Universität Dresden, 2012.

[46] N. Tucher et al. "3D optical simulation formalism OPTOS for textured silicon solar cells." In: *Optics express* 23.24 (2015), A1720–A1734.

[47] R. Varache et al. "Investigation of selective junctions using a newly developed tunnel current model for solar cell applications." In: *Solar Energy Materials and Solar Cells* 141 (2015), pp. 14–23. DOI: `10.1016/j.solmat.2015.05.014`.

[48] C. Wieners. “Numerical Methods for Maxwell’s Equations.” In: (2008-10-17). URL: `http://www.math.kit.edu/user/~wieners/MaxwellCourse.pdf` (visited on 2017-09-17).

[49] Wikipedia. *Band gap — Wikipedia, The Free Encyclopedia.* 2017. URL: `https://en.wikipedia.org/w/index.php?title=Band_gap&oldid=781976094` (visited on 2017-06-18).

[50] Wikipedia. *Hadamard product — Wikipedia, The Free Encyclopedia.* 2017. URL: `https://en.wikipedia.org/wiki/Hadamard_product_(matrices)` (visited on 2017-09-21).

[51] N. Wöhrle et al. “Understanding the Rear-Side Layout of p-Doped Bifacial PERC Solar Cells with Simulation Driven Experiments.” In: *Energy Procedia* (2017). PREPRINT.

[52] N. Wöhrle et al. “All-Diffused Back-Contact Back-Junction Solar Cell With Aluminum-Alloyed Emitter—Experiment and Simulation.” In: *IEEE Journal of Photovoltaics* 6.3 (2016), pp. 641–648.

[53] T. Yagi, Y. Uraoka, and T. Fuyuki. “Ray-trace simulation of light trapping in silicon solar cell with texture structures.” In: *Solar energy materials and solar cells* 90.16 (2006), pp. 2647–2656.

[54] W. S. Yang et al. “Iodide management in formamidinium-lead-halide–based perovskite layers for efficient solar cells.” In: *Science* 356.6345 (2017), pp. 1376–1379. DOI: `10.1126/science.aan2301`.

[55] K. Yee. “Numerical solution of initial boundary value problems involving Maxwell’s equations in isotropic media.” In: *IEEE Transactions on antennas and propagation* 14.3 (1966-05), pp. 302–307.

[56] J. Zhao et al. “Efficient organic solar cells processed from hydrocarbon solvents.” In: *Nature Energy* 1 (2016), p. 15027.